Institute of Metallurgy and Materials Science
Polish Academy of Sciences

Fraunhofer
IKTS

NOVA
UNIVERSIDADE NOVA
DE LISBOA

CEITEC

BRNO
UNIVERSITY
OF TECHNOLOGY

Institute of Metallurgy and Materials Science
of the Polish Academy of Sciences, Poland
Fraunhofer Institute for Ceramic Technologies and Systems, Germany
NOVA University Lisbon, School of Science and Technology, Portugal
CEITEC -Central European Institute of Technology,
Czech Republic

Proceedings
of
European School for Young
Materials Scientists
November 4th to 7th, 2024
Dresden – Germany

European School for young material scientists

Dresden - Krakow – Lisboa – Brno 2024

Edited by: Magdalena Bieda, Institute of Metallurgy and Materials Science of the Polish Academy of Sciences, Krakow, Poland

Scientific Committee:

Rodrigo Martins Professor in Materials Science, NOVA University Lisbon (Portugal)

Eva Olsson Professor at Chalmers University of Technology (Sweden)

Paweł Zięba Professor, Polish Academy of Science (Poland)

Tomas Sikola Research Group Leader, CEITEC, Brno (Czech Republic)

Luis Pereira Associate Professor at NOVA University Lisbon (Portugal)

Diana Gaspar Associate Professor at NOVA University Lisbon (Portugal)

Joanna Wojewoda-Budka Professor of Polish Academy of Science (Poland)

Magdalena Bieda-Niemiec Professor of Polish Academy of Science (Poland)

Organizing Committee:

André Clausner - Fraunhofer Institute for Ceramic Technologies and Systems, Dresden, Germany
Diana Gaspar - NOVA School of Science and Technology, Lisboa, Portugal
Magdalena Bieda-Niemiec - Institute of Metallurgy and Materials Science of the Polish Academy of Sciences, Krakow, Poland

ISBN 978-83-60768-99-0

Table of contents

Preface

The **ESYMS 2024** - **European School for Young Materials Scientists** will take place on **November 4-5** and aims to bring together young scientists, mainly PhD students, working in the exciting fields of Materials Science, Nanotechnology, Nanoscale Materials, Nanoanalysis, Multi-scale materials characterization, as well as Microscopy.

In 2024 the special focus will be put on all relevant techniques used for correlative materials characterization including Light Microscopy, Electron Microscopy, X-ray Microscopy, and Scanning Probe Microscopy. The contributions shall cover all topics from fundamental research up to technology and product development for the market.

The School will be a two days event and will count with a inspiring keynote lecture from a prominent scientist in the above-mentioned fields, as well as and most importantly, the very active participation of the PhD students. The event will create a live forum that brings together presentations of the PhD works (oral and posters), intensive discussions, and many opportunities for interaction and networking.

The School will be organized in close cooperation with the **4th Correlative Materials Characterization workshop** at Novembrer 6-7 as a second part of the school.

Organizers

How does copper affect biodegradable zinc?

M.Gieleciak[1,*], A.Jarzębska[1], Ł. Maj[1], M. Kulczyk[2], M. Bieda[1]

[1]*Institute of Metallurgy and Materials Science, Polish Academy of Sciences, 25 Reymonta Street, 30-059, Kraków, Poland,*
[2]*Institute of High Pressure Physics, Polish Academy of Sciences, 29/37 Sokołowska Street, 01-142, Warszawa, Poland,*

[*]*m.gieleciak@imim.pl*

Abstract

Biodegradable zinc materials are a widely discussed topic in the literature. Its corrosion rate allows the use of zinc for example to produce cardiovascular stents. However, the problems of low mechanical properties and low recrystallization temperature limit their usefulness. Utilizing severe plastic deformation methods and alloying additives may solve those problems. In this work pure zinc as a reference material and zinc-copper alloy were used to define the effect of alloying additive on the microstructure and mechanical properties. Additionally, thermal stability was performed in order to determine changes between initial materials and subjected to elevated temperatures. Research revealed a positive effect of Cu addition on grain refinement and mechanical properties. Moreover, zinc-copper alloy presents better thermal stability up to 150℃.

Keywords: biodegradable zinc, zinc alloys, thermal stability, recrystallization

Introduction

Biodegradable zinc-based materials are nowadays relatively often described in the literature as potential candidates to produce e.g. cardiovascular stents. Their advantages compared to non-degradable solutions include no long-term side effects like re-occlusion of blood vessels (called in-stent restenosis) or no need for repeated surgical intervention [1]. Other degradable metals, such as magnesium and iron, have corrosion rates that do not meet the requirements for such products, while zinc fits almost perfectly into these guidelines. This is due to its standard potential (-0.76V), which is located between the two aforementioned elements (-2.37V for Mg and -0.77V for Fe) [2]. However, pure zinc can be characterized by low mechanical properties limits its usefulness as a biomaterial. Nevertheless, it was proven that alloying additives and plastic deformation can significantly strengthen zinc by grain refinement and second-phase particles [3]. One of the additives that create with zinc second phase, according to equilibrium systems, is copper. Literature reports indicate, that copper is an essential element, that helps growth and development as an important catalytic cofactor for proteins [4]. Therefore, in small amounts is non-toxic for humans. One of the best techniques for plastic deformation of low alloyed zinc is hydrostatic extrusion. It is an unconventional method of severe plastic deformation in which material is deformed at high speed at room temperature and can change its diameter [5]. However, despite the positive effects of both alloying and deformation, researchers have mostly focused on characterizing these materials at room temperature. Considering the fact, that the human body temperature is about 37℃, the properties of materials may change. Therefore, it seems important to test materials also in the post-heating state. Especially taking into account the problem of low

recrystallization temperature of zinc. There is still a limited understanding of the specific impact of heating and as a consequence static recrystallization (SRX) on zinc and zinc-based materials. The main aim of this work is to firstly characterize zinc and zinc-copper alloy after plastic deformation and secondly define the effect of heating on the microstructural changes.

Results and Discussion

The research was performed on pure zinc and zinc-copper alloy with 3 weight percent of additive. The materials were gravity casted into the metal forms and subjected to two-step plastic deformation – hot extrusion at 250℃ and hydrostatic extrusion at 4 consecutive passes. As a result rods with 5 mm of diameter were obtained. According to the Zn-Cu phase diagram, the microstructure of the alloy consists of α-Zn grains and CuZn4 second phase and α-Zn grains for pure metal . Copper addition influenced grain refinement significantly (fig. 1). The calculated average grain size was 16.2 μm and 2.2 μm for Zn and ZnCu3, respectively. Simultaneously, the density of high-angle (HAGB) and low-angle grain boundaries (LAGB) increased. A higher amount of LAGBs suggests, that during plastic deformation DRX occurred partially and left structural defects. It can be confirmed also by grain orientation spread calculations, where for Zn this parameter was close to 0, while for alloy some grains took higher values.
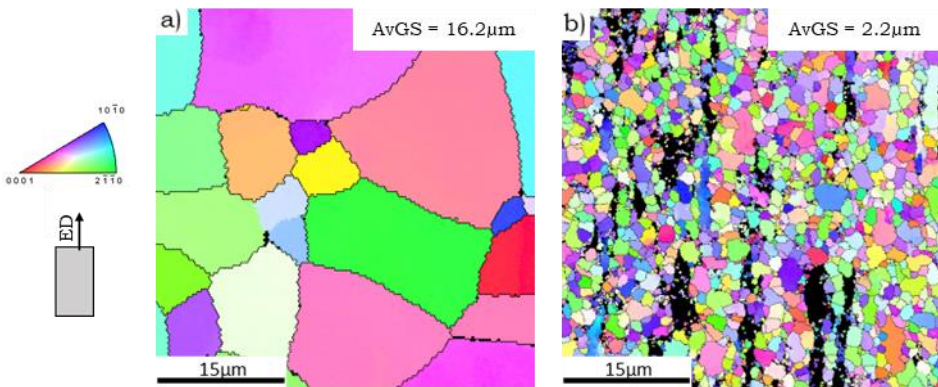
Fig.1. *SEM/EBSD microstructures of a) Zn and b) ZnCu3 after hydrostatic extrusion with calculated average grain sizes. Maps were collected according to the extrusion direction.*

Mechanical properties were investigated by static tensile test. Copper addition influenced ultimate tensile strength, yield strength, and elongation compared to pure zinc. Obtained results for UTS were 135/222 MPa, YS 70/117 MPa and E 61/86% for the material without and with alloying additive, respectively. According to the Hall-Petch relation, those values are consistent with the obtained SEM/EBSD microstructures (Fig.1).

In order to evaluate the effect of copper addition on the thermal stability of the microstructure, quasi-in-situ heating was performed. Pure zinc after plastic deformation showed unchanged microstructure up to 50℃. Average grain size and the density of HAGB and LAGB stayed at the same level. Above this temperature grain growth was observed, finally at 150℃ reaching almost fully recrystallized microstructure with an average grain size 45 μm. Copper addition led to inhibition of SRX, and even after heating at 150℃, average grain size increased slightly from 2.3 μm to 2.7 μm. At a temperature of 100℃, the density of grain boundaries increased as a result of the recovery process. Dislocation initially existed in the microstructure formed low-angle boundaries, and LAGBs formed HAGBs. Due to the lack of significant changes up to 150℃, heating at 250 degrees was also performed. This temperature revealed a static recrystallization and grain size increased to 5.7 μm. Fig. 2 presents SEM/EBSD microstructures of ZnCu alloy before and after heating.
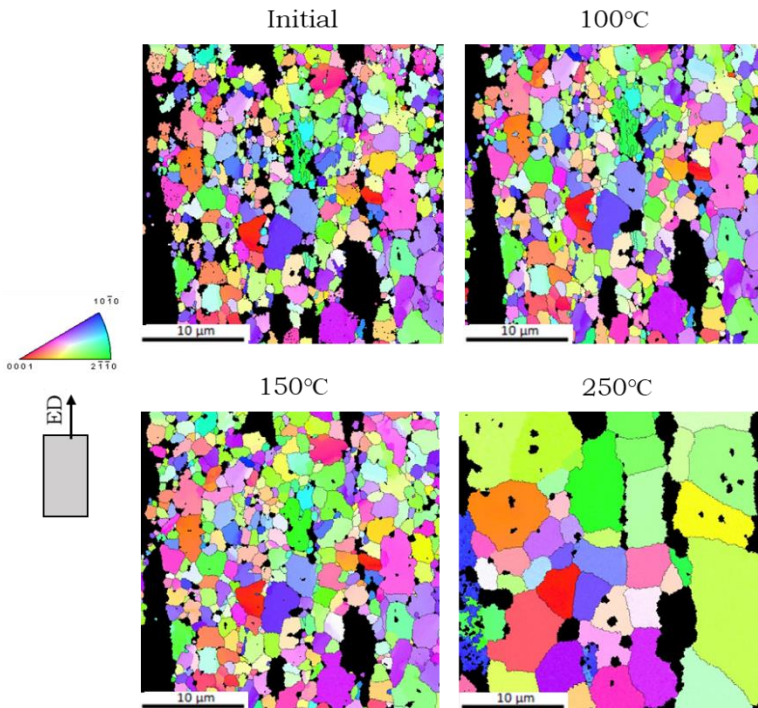
Fig.2. *Orientation maps of ZnCu3 alloy initially and after quasi-in-situ heating at different temperatures.*

Conclusions

This research leads to the following conclusions:

- The addition of copper leads to grain refinement and the generation of more structural defects reflected in the low-angle grain boundaries, compared to

pure zinc. Mechanical properties measured by static tensile test also increased as a result of alloying.

- The initial microstructure, i.e. after the hydrostatic extrusion affects the behavior of the material during heating. In the case of pure metal significant SRX was observed at 100℃ while for the alloy at 250℃.

Acknowledgements

References

[1] G. Levy, J. Goldman, E. Aghion, The Prospects of Zinc as a Structural Material for Biodegradable Implants—A Review Paper, Metals, *7*(10), 402, 2017
[2] D. Vojtěch, J. Kubásek, J. Čapek, I. Pospíšilová, Comparative Mechanical and Corrosion Studies on Magnesium, Zinc and Iron Alloys as Biodegradable Metals, Mater. Technol. 49, 6, 877–882, 2015
[3] S. Chen, T. Du, H. Zhang et al., Methods for improving the properties of zinc for the application of biodegradable vascular stents, Biomater. Adv., 156, 213693, 2024
[4] H. Tapiero, D.M. Townsend, K.D. Tew, Trace elements in human physiology and pathology. Copper, Biomedicine & Pharmacotherapy, 57(9), 386-398, 2003
[5] W. Pachla, S. Przybysz, A. Jarzębska et al., Structural and mechanical aspects of hypoeutectic Zn–Mg binary alloys for biodegradable vascular stent applications, Bioact. Mat., 6(1), 26-44, 2021

Process parameters of the anodic oxidation of cast biodegradable magnesium alloys on the properties of the protective coatings

M. Karaś[1], S. Boczkal[1], Ł. Maj[2], J. Skiba[3], D. Kapinos[1], K. Limanówka[1], A. Jarzębska[2], M. Bieda[2]

[1] Lukasiewicz Research Network – Institute of Non-Ferrous Metals, Light Metals Division, Poland
[2] Institute of Metallurgy and Materials science Polish Academy of Science, Cracow, Poland
[3] Institute of High Pressure Physics, Polish Academy of Sciences, Warsaw, Poland

*michal.karas@imn.lukasiewicz.gov.pl

Abstract

The influence of process parameters during anodic oxidation in environmentally friendly solutions is presented in this paper. The thickness, porosity and corrosion resistance of the protective layer are affected by varying the current density and the process time. Increasing the current density increases the thickness and corrosion resistance of the biodegradable magnesium alloy. The phases presented in the coatings identified, such as Mg, $KMgF_3$, MgF_2 and MgO improve the corrosion resistance of the MgZn1Ca0.2Li1 alloy.

Keywords: biodegradable implants, magnesium alloys, orthopaedic biomaterial, protective coating on biodegradable magnesium alloys.

Introduction

Magnesium and its alloys, with their good ratio of mechanical properties to material density, play an important role in biomedical engineering but there are limited by the corrosion rate, which can lead to deterioration of their performance characteristics. The application of a protective coating is one way of reducing the rate of corrosion. The findings of this research are pivotal for the advancement of orthopedic biomaterials, particularly in the development of more durable and biocompatible materials suitable for extensive applications in biomedical engineering. Among the methods evaluated, the anodic oxidation process utilizing a KOH + KF solution exhibited the most favorable properties. This selection is justified by several key advantages that affirm its optimality. The KOH + KF solution facilitates the obtainment of coatings with optimal thicknesses, which are challenging to achieve using other electrolytes. Precise control over coating thickness can be achieved through the adjustment of process parameters, which is essential for ensuring the optimal protective properties of the coatings [1].

Results and Discussion

The KOH + KF solution is non-toxic and alkaline, enhancing process safety relative to more aggressive chemical alternatives. Coatings produced using this solution exhibit not only increased thickness and roughness but also a favorable chemical composition, incorporating elements that are biocompatible. This characteristic renders the coatings particularly suitable for biomedical. From previous studies on chemical composition, as well as chemical and corrosion properties the

MgZn1Ca0.2Li1 alloy was chosen as a substrate material. The as cast material was subjected to anodic oxidation in a biocompatible electrolyte solution. Detailed process parameters are showed in Table 1.

Table 1. Summary of sample name with protective coating fabrication parameters on MgZn1Ca0.2Li1 alloy.

Sample No.	Current density [A/dm²]	Process time [min]	Solution temperaturę [°C]
MgZn1Ca0.2Li1_5_5	5	5	25.9
MgZn1Ca0.2Li1_5_10	5	10	24.2
MgZn1Ca0.2Li1_10_5	10	5	24.1
MgZn1Ca0.2Li1_10_10	10	10	24.2

Optimization of the anodizing process toward increasing both current density and time leads to improved microstructural quality of protective coatings, which is crucial for applications in biological environments. Protective coatings produced in KOH + KF solution at different current densities and process times were compared. The effects of varying fabrication parameters on the microstructure and characteristics of protective fluoride coatings are illustrated in the figures 2. Analysis of the microstructure of fluoride protective coatings, provides important information on the effect of process parameters on the quality and integrity of coatings on magnesium alloy.

a)   b)   c)   d)
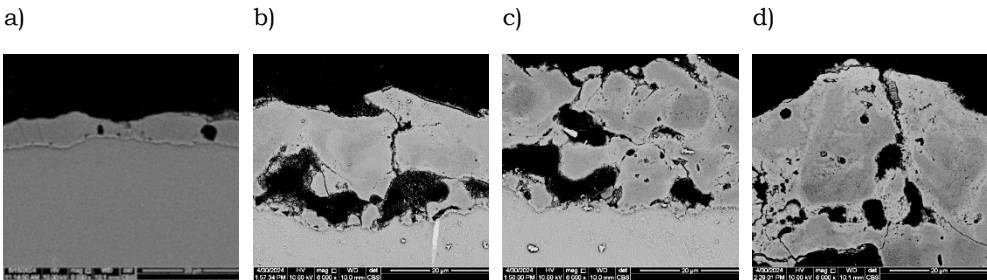
Fig. 2. Microstructure of the protective coating or two magnifications 6000x: a) sample produced at a current density of 5 A/dm2 and for 5 minutes (MgZn1Ca0.2Li1_5_5), b) sample produced at a current density of 5 A/dm2 and for 10 minutes (MgZn1Ca0.2Li1_5_10), c) sample produced at a current density of 10 A/dm2 and for 5 minutes (MgZn1Ca0.2Li1_10_5) d) sample produced at a current density of 10 A/dm2 and for 10 minutes (MgZn1Ca0.2Li1_10_10).

Each image (a-d) shows coatings obtained at different current densities and anodic oxidation times. The microstructures are crucial to the corrosion properties of the coatings, as the quality, continuity and number of defects directly affect their protective effectiveness. Analysis of the microstructure of fluoride coatings clearly shows the effect of anodizing process parameters on their quality. Too short anodizing time (sample a) results in a thin, porous coating with low protective effectiveness. Increasing the anodizing time at the same current density (sample b) improves the integrity of the coating, but some defects are still visible. Increasing the current density (sample c) leads to faster coating growth, but at the same time causes numerous defects. The best coating properties were obtained for sample (d), where both higher current density and longer anodizing time were used. This type of coating has the highest homogeneity and the lowest number of defects, which is likely to translate into better corrosion properties. High current density can lead to the formation of a more porous coating structure, as intense electrochemical reactions can generate bubbles and micro-cracks in the coating. Current density directly affects the growth rate of a protective coating. Higher current density leads to faster growth of the coating layer, which can increase its thickness. With such selected parameters, coating thicknesses ranging from 4.5 to as much as 50 micrometers were obtained (fig. 3).
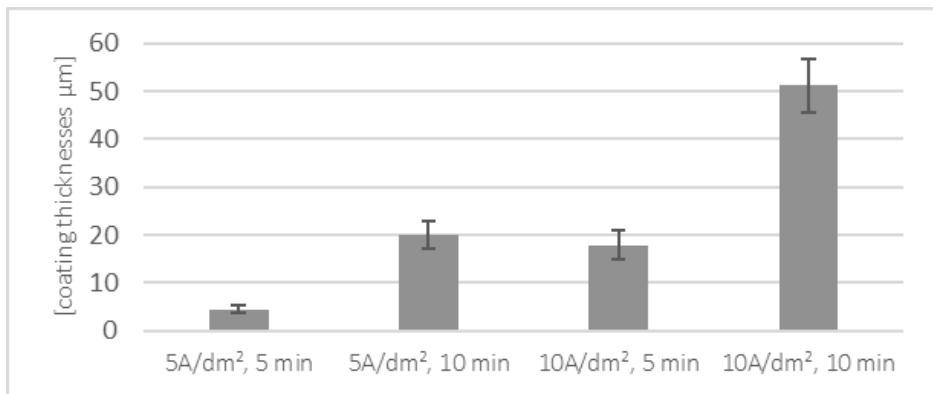
Fig. 3 Average thicknesses of the protective coating produced at different current parameters and at different times.

The thickness of the coating produced by anodic oxidation on magnesium alloys is significantly influenced by current density and processing time. The most efficient way to increase coating thickness is to increase the current density, although increasing the time also contributes. However, the thickest coatings are produced by a combination of higher current density and longer duration. The next step of investigations was EDS analysis. The EDS maps analysis of protective coatings made using current densities of 5 A/dm^2 with processing times of 10 minutes are shown in fig. 4.
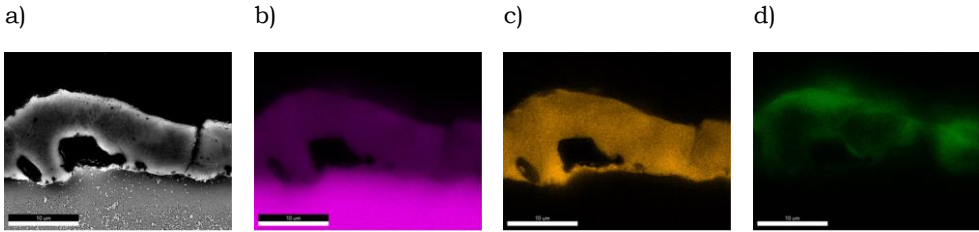
Fig.4. EDS analysis of the protective coating produced at a current density of 5 A/dm2 and for 10 minutes. Sample MgZn1Ca0.2Li1_5_10: a) photo of the analysis site, b) magnesium, c) fluorine, d) potassium.

The chemical compounds in the coating are considered to be biocompatible and safe for use by the human body. The basic elements found in the coating include fluorine, potassium and magnesium. The anodic oxidation process on magnesium alloys typically involves the reaction of the alloy surface with oxygen and fluoride ions from the electrolyte, leading to the formation of protective oxide and fluoride phases. The X-ray diffraction analysis confirmed the following phases: $KMgF_3$, MgF_2, MgO, and Mg. Each phase contributes to the overall protective function of the coating, with varying levels of effectiveness in enhancing corrosion resistance and controlling the degradation rate of the underlying alloy. Electrochemical testing were performed for obtained coatings. OCP measurements were carried out for 60 minutes in Ringer's solution at an elevated temperature of 37 °C. Table 2 shows numerical values electrochemical corrosion test of MgZn1Ca0.2Li1 uncoated and with coatings alloys.

Table 2. Numerical values electrochemical corrosion test of magnesium alloy with coatings produced at different process parameters.

Sample name	E_{corr} [mV]	I_{corr} [A/cm^2]	R_p [Ω]
MgZn1Ca0.2Li1_ uncoated	-1547	5,1E-05	340
MgZn1Ca0.2Li1_5_5	-1434	2,4E-05	1443
MgZn1Ca0.2Li1_5_10	-1412	6,2 E-06	4007
MgZn1Ca0.2Li1_10_5	-1439	9,32E-06	3428
MgZn1Ca0.2Li1_10_10	-1339	1,74E-06	4927

At more negative values of corrosion potential, the material corrodes more easily. The table 2 shows, that the unprotected sample has the lowest corrosion potential of -1547mV, indicating that it is most susceptible to corrosion compared to samples with protective coatings. E_{corr} values for coated samples are less negative, indicating improved corrosion resistance. The highest corrosion potential, and thus the best corrosion resistance, is shown by the MgZn1Ca0.2Li1_10_10 sample with a value of -1339 mV. The unprotected (coated) sample has the highest I_{corr} value of 5.1E-05 A/cm², indicating the highest corrosion rate. In contrast, the coated samples have a significant reduction in I_{corr} values, especially for the MgZn1Ca0.2Li1_5_10 (6.2E-06

A/cm²) and MgZn1Ca0.2Li1_10_10 (1.74E-06 A/cm²) samples. Sample MgZn1Ca0.2Li1_10_10 shows the lowest corrosion current density, indicating the highest corrosion protection efficiency. Polarization resistance, measured in ohms (Ω), is a parameter inversely proportional to the corrosion rate - the higher the value of R_p, the higher the corrosion resistance. The uncoated sample has the lowest polarization resistance of 340 Ω, indicating very low corrosion resistance. In contrast, coated samples show much higher R_p values. The MgZn1Ca0.2Li1_10_10 sample reaches 4927 Ω, indicating the most effective corrosion protection.

Conclusions

To increase the corrosion resistance of biodegradable magnesium alloys, it is best to use protective conversion coatings that have fluorides and metal oxides in their composition. The process parameters are the most important during the manufacturing of coatings on MgZn1Ca0.2Li1 alloy. Relationship between current density, time, and coating thickness is crucial for optimizing the protective performance of magnesium alloy coatings, particularly for applications where controlled degradation is important. The analysis of anodically oxidized magnesium alloys reveals the formation of key protective phases—MgF_2, $KMgF_3$, and MgO—along with residual metallic magnesium. The fluoride phases, particularly MgF_2, are highly effective in enhancing the corrosion resistance of magnesium alloys, making them suitable for biodegradable applications in biomedical devices. The combination of these phases ensures a controlled degradation of the alloy, allowing for temporary medical implants that gradually dissolve in the body.

Acknowledgements

References

[1] Runjia Liu, Enhanced corrosion protection for MAO coating on magnesium alloy by the synergism of LDH doping with deposition of 8HQ inhibitor film, Ceramics International, Volume 49, Issue 18, 15 September 2023, Pages 30039-30048, doi.org/10.1016/j.ceramint.2023.06.261

Evaluation of Antibacterial Ti6-Al4-V/Chitosan/TiN Layer Systems obtained via the EPD Technique: Structural, Mechanical, and Biological Properties

M.Biegun-Żurowska[1,*], T.Goryczka[2], E.Menaszek[4], K.Klesiewicz[5], M.Ziąbka[1]

[1] AGH University of Krakow, Faculty of Materials Science and Ceramics, Department of Ceramics and Refractories, Reymonta 30, 30-059 Krakow, Poland
[2] University of Silesia in Katowice, Institute of Materials Science, 75 Pułku Piechoty 1A, 41-500 Chorzow, Poland.
[3] Pomeranian Medical University in Szczecin, Department of Orthodontics, Al. Powst. Wlkp. 72, 70-111 Szczecin,
[4] Jagiellonian University Collegium Medicum, Department of Cytobiology, Faculty of Pharmacy Medyczna 9 Street, 30-068 Cracow, Poland
[5] Jagiellonian University Collegium Medicum, Department of Pharmaceutical Microbiology, Faculty of Pharmacy, Medyczna 9 Street, 30-688 Kraków, Poland

*biegun@agh.edu.pl

Abstract

Poster presents the results of structural, surface and biological studies of antibacterial layers containing different concentrations of titanium nitride (TiN) particles. Coatings were obtained using the Electrophoretic Deposition Process (EPD) and are being investigateg for potential applications in various biomedical fields. Comprehensive characterization of the coatings was performed, including Scanning Electron Microscopy (SEM) analysis with layer thickness measurement, X-ray Diffraction (XRD) analysis as well as tests for coatings adhesion, antibacterial activity, and cytotoxicity.

Keywords: Antibacterial coatings, Electrophoretic Deposition Process, Orthodontic implants

Introduction

Titanium orthodontic implants are increasingly utilized in contemporary dental treatments due to their numerous advantages, including enhanced stability, long-term functionality, and minimally invasive application. However, despite these benefits, such implants are associated with a substantial risk of bacterial infections, which may result in implant failure and complications for patients [1,2]. To address these risks, there is a growing interest in developing surface coatings that provide sustained antibacterial protection, potentially reducing reliance on antibiotic therapies and minimizing the emergence of antibiotic resistance. A promising approach to fabricating such coatings is the Electrophoretic Deposition Process. This method is gaining recognition for its versatility and efficacy in producing thin, uniform coatings on complex geometries, such as implant materials. EPD offers precise control over the composition and thickness of coatings [3], making it highly suitable for biomedical applications where both mechanical and biological properties are critical. In our study, we employed a combination of chitosan and titanium nitride (TiN) particles for the coating system. Chitosan, a natural biopolymer, is well-known for its excellent biocompatibility and inherent antibacterial properties, making it a viable candidate for biomedical coatings. Titanium nitride, conversely, has been widely

researched for its mechanical robustness, corrosion resistance, and antibacterial effects.

Results and Discussion

Scanning electron microscopy (SEM) analysis (Fig. 1) verified the successful formation of EPD coatings with increasing concentrations of TiN particles on etched Ti-6Al-4V substrates. The surface morphology of the uncoated titanium alloy exhibited significant roughness due to the HF acid etching process, which is expected to enhance implant integration and improve osseointegration. The pure chitosan coating displayed a smooth and homogeneous morphology, with minor agglomerates and micropores. SEM micrographs of the chitosan/TiN composite coatings confirmed the incorporation of ceramic particles, revealing a continuous, crack-free surface. With higher TiN particle concentrations, the coatings demonstrated increased density and thickness, ranging from 12.25 to 20.56 μm.
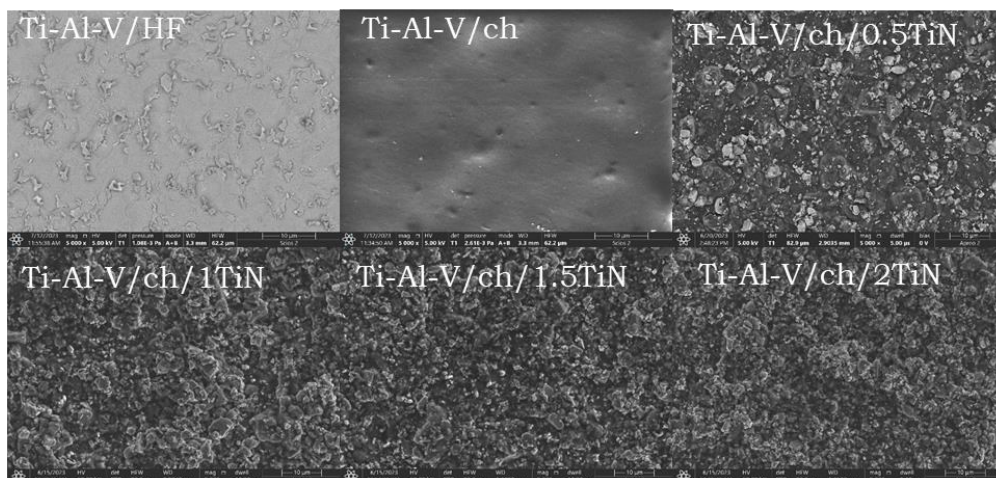
Fig.1*. SEM images and EDS analysis of HF etched titanium alloy (Ti-Al-V) coated with EPD chitosan/TiN layers.*

The XRD Analysis revealed that the Ti6-Al4-V substrate is a two-phase alloy, consisting of a dominant α-phase with a hexagonal crystal lattice and a β-phase with a cubic crystal lattice. The diffractograms showed that titanium nitride (TiN) was crystalline, while chitosan existed in an amorphous form, evidenced by a broadened 2θ maximum around 20°. Notably, increasing the TiN content in the deposited mixture led to a decrease in the intensity of diffraction lines from the α-phase, confirming that the volume fraction of the Ti6-Al4-V alloy's α-phase decreases as the TiN concentration increases, which correlates with an increase in layer thickness.

The adhesion strength of the chitosan/TiN coatings was evaluated using the direct pull-off method, showing a decreasing trend as the titanium nitride content increased. Although this aligns with the theory that adhesion strength decreases with coating thickness, statistical analysis revealed no significant differences based on TiN concentration. Further optimization of deposition methods and post-treatment processes remains crucial to achieving better outcomes for EPD coatings in medical applications.
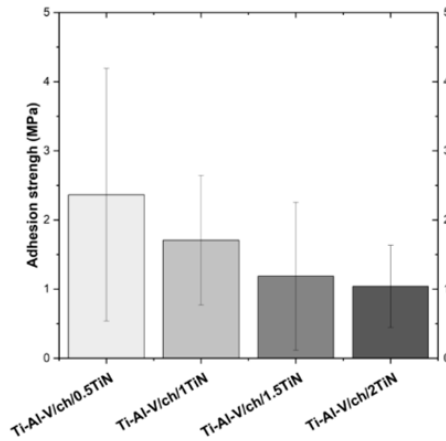
Fig.2. *Adhesion strength of titanium alloy (Ti-Al-V) covered with chitosan/TiN EPD coatings.*

The antibacterial activity tests (Tab.1.) against Staphylococcus aureus and Escherichia coli revealed that the pure titanium alloy exhibited no antibacterial properties. In contrast, the chitosan coating demonstrated a one-log reduction in Gram-positive bacteria. For the coating containing both chitosan and titanium nitride, a three-log reduction was observed for Gram-positive bacteria and a two-log reduction for Gram-negative bacteria. These results indicate a significantly enhanced antibacterial effect when titanium nitride is incorporated into the chitosan-based coating.

Tab.1. *The antimicrobial efficacy of the investigated material*

Sample	*S. aureus*	*E. coli*
Ti-Al-V/HF	$7{,}65 \cdot 10^7$	$7{,}82 \cdot 10^6$
Ti-Al-V/ch	$3{,}75 \cdot 10^4$	$4{,}90 \cdot 10^5$
Ti-Al-V/ch/0,5TiN	$2{,}60 \cdot 10^2$	$5{,}00 \cdot 10^3$
Initial amount of CFU:	$1{,}5 \cdot 10^5$	$1{,}5 \cdot 10^5$

Despite demonstrating antibacterial potential, the coatings were found to be cytotoxic, as evidenced by both quantitative analysis (Fig. 4) and fluorescence microscopy images. In comparison to the pure titanium alloy, the osteoblast cells did not proliferate or develop properly on the coated surfaces. Such result suggests that, although the coatings are effective against bacterial growth, they adversely affect cellular behavior, indicating a need for further optimization to improve their biocompatibility.

Conclusions

The findings of the studies suggest that depositing homogeneous EPD coatings of TiN particles and chitosan alters the properties of implant surfaces to various degrees. In terms of implant applications, such changes may prove desirable. Despite the antibacterial effectiveness of these coatings, initial biological tests have revealed

concerns regarding their cytotoxicity. This limits their direct application in biomedical devices such as orthodontic implants without further optimization. The observed toxicity suggests that additional modifications to the layer composition or processing parameters are necessary to enhance biocompatibility. Future studies will focus on both reducing the cytotoxic effects and enhancing adhesion while maintaining antibacterial properties, with the aim of developing a safer, functional coating suitable for long-term implant use.
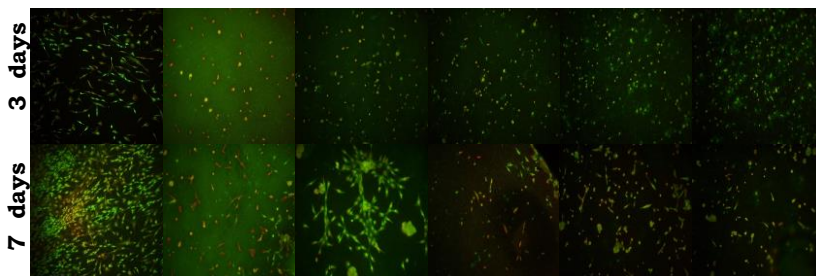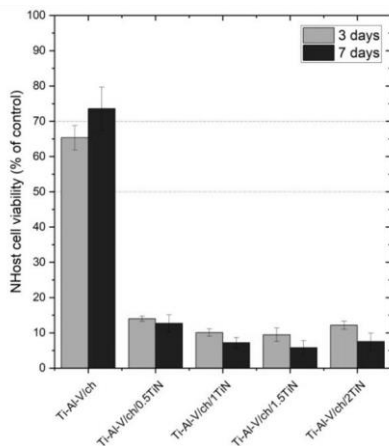
Fig.4 *The proliferation of NHost cells on the modified Ti-Al-V surfaces evaluated by Presto Blue assay conducted at time points of 3 and 7 days.*

Acknowledgements

References

[1] L. Zhang, C. Ning, T. Zhou, X. Liu, K.W.K. Yeung, T. Zhang, Z. Xu, X. Wang, S. Wu, and P.K. Chu: ACS Appl. Mater. Interfaces, 2014, vol. 6, pp. 17323–45.
[2] L. Zhao, P.K. Chu, Y. Zhang, and Z. Wu: 2009, pp. 470–80.
[3] D. Zhitomirsky, J.A. Roether, A.R. Boccaccini, and I. Zhitomirsky: J. Mater. Process. Technol., 2009, vol. 209, pp. 1853–60.

Development of Hybrid Sol-Gel Coatings containing Hexagonal Boron Nitride and Titanium Nitride Nanoparticles: Synthesis, Composition, and Biological Properties`

K. Matysiak[1,*], K. Klesiewicz[2], K. Cholewa-Kowalska[1], M. Ziąbka[1]

[1] *AGH University of Krakow, Faculty of Materials Science and Ceramics, Kraków, 30 Reymonta Street, Poland, 30-059*
[2]*I Department of Pharmaceutical Microbiology, Faculty of Pharmacy, Jagiellonian University Medical College, Medyczna 9 St., 30-688 Kraków, Poland*

[*]*kmatysiak@agh.edu.pl*

Abstract

The aim of this study was to develop hybrid coatings consisting of titanium nitride (TiN) and boron nitride nanoparticles (hBN) on the TiAlV medical alloy using the sol-gel process. These coatings were engineered to enhance bactericidal properties and offer protection against surgical wear during the implantation of medical devices, improving both the performance and longevity of implants. The study focused on thoroughly analyzing the microstructure (using SEM), structure (through FTIR), and surface characteristics, such as wettability and surface free energy of the coatings.

Keywords: sol – gel layers, ceramic nanoparticles

Introduction

Titanium (Ti) and its alloys are favored in biomedical applications due to their excellent mechanical properties and high biocompatibility, making them ideal candidates for osseointegrative implants [1]. However, despite their many advantages, Ti alloys also face certain limitations, particularly their poor wear resistance, which remains a significant concern [2]. Wear debris and corrosion products can accumulate, causing adverse reactions with surrounding bone tissue and potentially leading to implant failure. To address these issues, improving the bioactivity, wear resistance, and corrosion protection of titanium alloys through surface modification is crucial [1,2]. One of the most promising approaches for enhancing these properties involves the application of protective coatings [1]. Among the different coating techniques, the sol-gel method stands out for its potential to offer superior corrosion resistance while also enabling the incorporation of antimicrobial agents within a pure silica matrix [2]. In this study, two hybrid bilayer sol-gel systems, $SiO_2/hBNNP$ and $SiO_2/TiNNP$, were developed. The aim of the presented work is to investigate how deposition process parameters and the appropriate selection of sol components affect the microstructure and surface properties. Additionally, the antibacterial potential of the proposed coatings was also examined.

Results and Discussion

SEM observations of the layers (Fig.1) confirmed the presence of ceramic particles on the modified titanium alloy, indicating successful deposition of the coating. However, the analysis also revealed that the layers were not entirely homogeneous, with

titanium nitride particles displaying uneven distribution across the surface. Despite this, no porosity or visible cracks were detected in the composite material, suggesting good overall structural integrity.
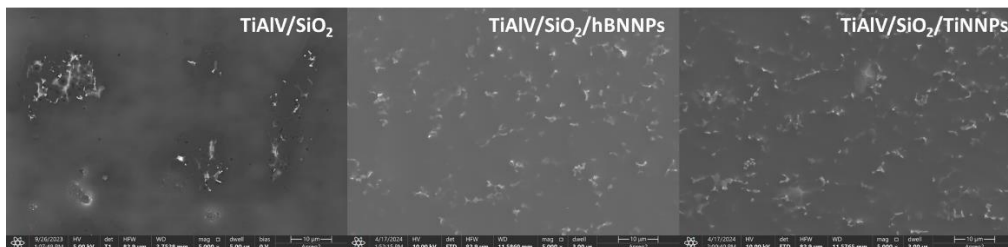
Fig. 1. *SEM microphotographs of SiO₂ coatings deposited on Ti6Al4V samples and obtained in sol–gel reaction*

Figure 2 illustrates the FTIR spectra of the layers measured immediately after deposition, covering the 400–4000 cm⁻¹ spectral range. In all the spectra, a weak band observed between 3100–3600 cm⁻¹ was associated with the presence of physically and/or chemically bound water, specifically representing the OH symmetric stretching of asymmetrically hydrogen-bonded water molecules. This indicates residual moisture in the layers, which is common in freshly applied sol-gel coatings. Furthermore, the CH alkyl stretching bands were clearly detected within the 2890–2960 cm⁻¹ range, suggesting the presence of organic components, such as alkyl groups, derived from the sol-gel precursors. Notably, the peaks observed at 770, 1020, and 1160 cm⁻¹ corresponded to the stretching vibrations of Si–O–Si bonds. The appearance of these distinct Si–O–Si stretching bands is a clear marker of the polycondensation reaction between tetraethyl orthosilicate (TEOS) and GPTMS, signifying the formation of a robust silica network within the hybrid layer. The FTIR spectrum of the coatings containing h-BN particles revealed characteristic peaks at 825 cm⁻¹ and 1370 cm⁻¹, which can be attributed to the vibrations of the B-N bond. The band observed at 1045 cm⁻¹ can be attributed to Ti-N stretching vibrations, while the vibrations at 547 cm⁻¹ are associated with Ti-N stretching modes.

The modification of TiAlV alloys with organic-inorganic hybrid layers significantly altered their surface characteristics, as evidenced by the changes in contact angle and surface free energy (Fig.3). The increased contact angle and lowered surface energy suggest that the introduction of ceramic particles, such as h-BN and TiN, into the hybrid layers enhances the water-repellent properties of the alloy. This shift towards hydrophobicity could improve the alloy's performance in biomedical applications by reducing the likelihood of fluid accumulation on the surface, potentially decreasing biofilm formation and enhancing the long-term durability of implants. The strong correlation between ceramic particle content and surface property changes underscores the importance of controlling the composition of the hybrid coatings to tailor the surface characteristics for specific applications.
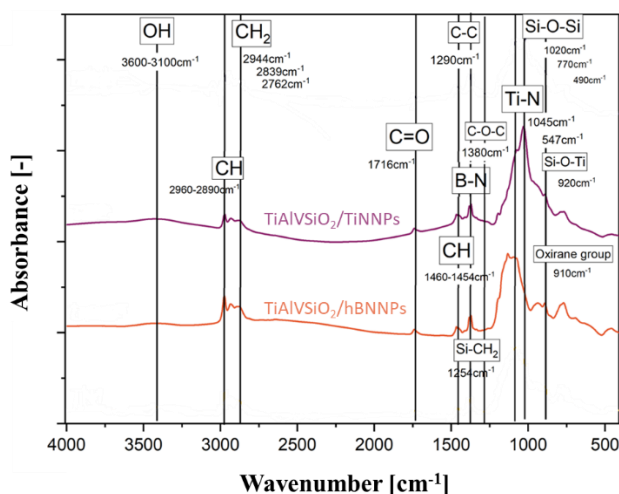
Fig.2. *FTIR spectra of titanium alloy (TiAlV)-covered sol–gel hybrid layer containing A)hBNNPs and B)TiNNPs.*
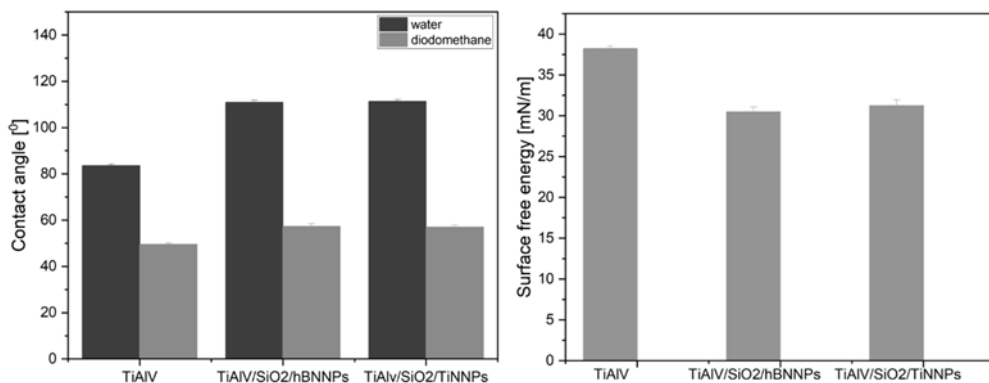
Fig.2. *FTIR spectra of titanium alloy (TiAlV)-covered sol–gel hybrid layer containing A)hBNNPs and B)TiNNPs.*

Antibacterial studies (Fig.3) showed that the addition of ceramic nanoparticles resulted in the inhibition of the growth of both gram-positive and gram-negative bacterial strains. For the SiO2/TiNNP ssample, the number of bacterial colonies decreased by one logarithm, while for the SiO2/hBNNP ssample, it decreased by two logarithms. This suggests that the proposed layers are bacteriostatic.

Sample name	*S.Aureus*	*E.coli*
TiAlVHF	$7{,}65 \cdot 10^7$	$7{,}82 \cdot 10^6$
TiAlV/SiO$_2$	$2{,}12 \cdot 10^6$	$2{,}2 \cdot 10^6$
SiO$_2$/hBNNPs	$4 \cdot 10^4$	$1{,}5 \cdot 10^5$
SiO$_2$/TiNNPs	10^5	10^5

Initial amount: $1{,}5 \cdot 10^6$

Fig.3. *The antimicrobial efficacy of the investigated materials (colony-forming unit).*

Conclusions

The modification of the Ti alloy layer altered surface properties such as wettability, surface energy, and roughness. SEM observations of the layers indicated that ceramic particles were not uniformly distributed. .Additionally, the incorporation of TiN or hBN nanoparticles into the layers resulted in an increased contact angle, which in turn lowered the surface energy. Biological studies further validated the bacteriostatic properties of the coatings, demonstrating their effectiveness in inhibiting bacterial growth. Further research should focus on improving the homogeneity of the obtained layers.

Acknowledgements

References

[1] H. J. Haydar, J. Al-Deen, A. K. Abidali, and A. A. Mahmoud, "Improved performance of Ti6Al4V alloy in Biomedical applications - Review.," in Journal of Physics: Conference Series, IOP Publishing Ltd, Aug. 2021. doi: 10.1088/1742-6596/1973/1/012146.

[2] A. Zanurin, N. A. Johari, J. Alias, H. M. Ayu, N. Redzuan, and S. Izman, "Research progress of sol-gel ceramic coating: A review," in Materials Today: Proceedings, Elsevier Ltd, 2021, pp. 1849–1854. doi: 10.1016/j.matpr.2021.09.203..

Application of magnetite nanoparticles modified by γ-cyclodextrin in magnetic hyperthermia and dyes adsorption

A. Ciuraszkiewicz[,1,2*], A. Radoń[1], Ł. Hawełek[1], T. Warski[1], J. Wojewoda-Budka[2], and A. Kolano-Burian[1]

[1] *Łukasiewicz Research Network — Institute of Non-Ferrous Metals, Gliwice, Poland*
[2] *Institute of Metallurgy and Materials Science, Polish Academy of Sciences, Cracov, Poland*

[*]*agnieszka.ciuraszkiewicz@imn.lukasiewicz.gov.pl*

Abstract

Magnetite nanoparticles (MNPs) are extensively researched for various biomedical applications, including magnetically induced hyperthermia. This study investigated the impact of cyclodextrin decomposition on the crystallization of MNPs, as well as their effectiveness in magnetic hyperthermia and dye adsorption processes. The findings confirmed that modifying the synthesis process, particularly the medium and the method of cyclodextrin introduction, results in the production of magnetite nanoparticles with distinct magnetic properties. The highest magnetic hyperthermia effect was observed in the sample synthesized by method M3 in benzyl ether with cyclodextrin. At a concentration of 0.25 mg/ml, the specific absorption rate (SAR) exceeded 200 W/g. However, SAR alone is insufficient to fully assess the nanoparticles' potential; the temperature increase must also be evaluated. At 0.25 mg/ml, the temperature increased by 7.60 ± 0.72°C, while at 2 mg/ml, it increased by 21.2 ± 0.83°C. Lastly, the dye adsorption efficiency of the MNPs was assessed. The results showed that the MNPs synthesized using also method M3, similar to the magnetic hyperthermia results, exhibited the highest adsorption capacity, adsorbing over 70% of both rhodamine B and crystal violet dyes.

Keywords: Fe_3O_4 nanoparticles, magnetic hyperthermia, polysaccharide coating, dye adsorption, cyclodextrin

Introduction

Magnetite's spinel structure, with Fe^{2+} and Fe^{3+} cations in octahedral and tetrahedral sites, respectively, gives it unique properties such as ferrimagnetism, biocompatibility, and chemical stability. These features make magnetite valuable in various fields, from catalysis to medicine. Magnetite nanoparticles (MNPs) are particularly useful due to their ability to be functionalized, enhancing their applications as biosensors, MRI contrast agents, hyperthermia therapy agents, and magnetic drug carriers [1]. Despite their advantages, MNPs face challenges such as aggregation in hydrophilic media due to strong electrostatic interactions [2]. To address this, they are often coated with polymers like cyclodextrin, which improves their stability and biocompatibility. Cyclodextrin is favored for its non-toxicity, water solubility, and anticoagulant properties, making it an ideal coating material for magnetite [3]. Research has demonstrated the effectiveness of polysaccharide-coated MNPs in various applications, including cancer treatment through magnetic hyperthermia, where heat is used to destroy tumor cells or enhance their sensitivity to other treatments [4]. Hyperthermia is particularly effective against tumors, which are less able to manage

heat compared to normal cells [5]. Magnetite nanoparticles are also highly effective at adsorbing dyes from aqueous solutions due to their large surface area, magnetic properties, and surface functionalization. These nanoparticles can be easily modified with polymer coatings, enhancing their adsorption efficiency for various dyes. The magnetic properties of MNPs allow for easy recovery and reuse, making them ideal for environmental applications, such as wastewater treatment [6].

Materials and method

Magnetite nanoparticles were synthesized using a high-temperature degradation method with γ-cyclodextrin as a modifier. Four different synthesis approaches (M1-M4) were employed to explore the influence of the medium and the cyclodextrin decomposition process on the structure and properties of Fe_3O_4 nanoparticles. In the M1 synthesis, triethylene glycol (TREG) was used as the boiling medium, with the modifier introduced alongside the precursor before the boiling stage. In the M2 process also used triethylene glycol, but the precursor was added after the crystallization of the MNPs. For the M3 synthesis, benzyl ether (BE) was used as the boiling medium, and, similar to M1, the modifier was introduced at the start of the synthesis. In contrast, the M4 synthesis used benzyl ether as the boiling medium, but the modifier was added only after the MNPs crystallization process. Wide-angle X-ray diffraction (XRD) measurements were performed using a Rigaku MiniFlex 600 diffractometer. The tests were carried out at room temperature, in a scattering angle range of 2θ = 10-90°, with a scanning speed of 1.5°/min and a measurement step of 0.02°. Thermogravimetric analysis (TGA) was conducted under an argon atmosphere. Heating was applied at a rate of 10°C/min, spanning from room temperature (25°C) to 800°C. The magnetic hyperthermia effect was measured using D5 Series Automatic Driver G2 with D5 Calorimetry CoilSet (nanoScale Biomagnetics SL) under optimal conditions, which, based on preliminary tests, were determined to be a frequency of 347 kHz, a magnetic field intensity of 17 kA/m, and a concentration of 25 mg/ml. Adsorption measurements were conducted within the wavelength range of 190-750 nm using a UV-Vis spectrophotometer (ThermoFisher Scientific Evolution™ 220).

Results and Discussion

XRD analysis confirmed that all materials are single-phase, exhibiting characteristic diffraction peaks for magnetite (JCPDS card no. 01-075-1372). The results are presented in Fig. 1A. The Halder-Wagner method was applied to determine the average crystallite size. The samples synthesized in TREG (ckldex M1 and ckldex M2) have smaller crystallites (5.5 ± 0.1 nm and 8.1 ± 0.1 nm, respectively) than the samples synthesized in BE (ckldex M3 and ckldex M4) for which average crystallite sizes was equal to. 22.2 ± 0.7 nm and 37.7 ± 0.4 nm, respectively.

In addition to the impact of the synthesis method on nanoparticle size, its influence on the formation of polymeric shells was also examined using TGA (Fig. 1B). The TGA curves reveal two primary mass loss steps for all synthesized nanomaterials. The first significant mass loss in the prepared materials occurred within the temperature range of 200 to 420°C. The decomposition temperature of the organic phase varied depending on the synthesis method. These changes are attributed to the decomposition of γ-cyclodextrin and/or the carbonous shells formed in this high-boiling medium (~298°C). A second significant mass loss, observed between 600 and 700°C, corresponds to the degradation of the carbon-based structures [7].
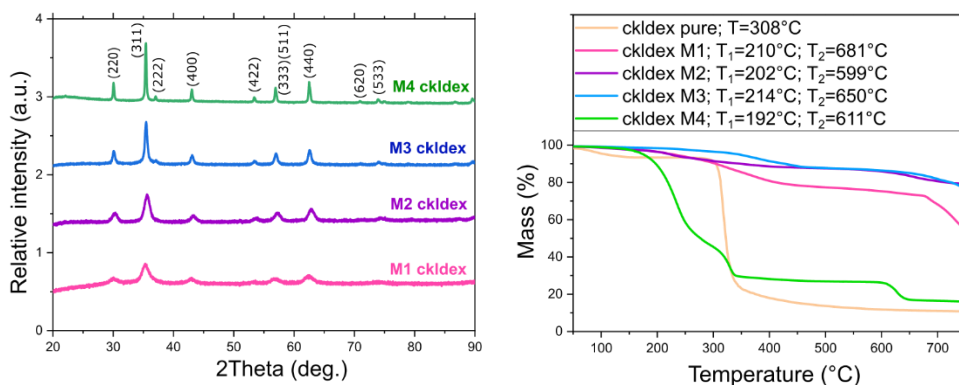
Fig. 1 *A- XRD patterns of Fe₃O₄ synthesized using cyclodextrin with marked Miller indices characterized for magnetite; B- TGA curves with onset temperatures of pure cyclodextrin and MNPs synthesized in the presence of γ-cyclodextrin using methods M1-M4*

It was postulated that crystallite size and differences in shell composition influence the magnetic hyperthermia effect generated by the MNPs and the dye adsorption process. All synthesized materials were measured under established conditions, and the results are shown in Table 1. Following the SAR measurements at a dispersion concentration of 25 mg/ml, ckldex M3, was selected for testing at lower concentrations (0.25, 0.5, and 2 mg/ml). Reducing the concentration of magnetite is crucial for biomedical applications [8]. As shown in Table 3, the highest SAR values were observed at the lowest concentration of 0.25 mg/ml, which was equal to 227.05 ± 11.42 W/g. Interestingly, despite the low concentration equal to 0.25mg/ml, the temperature change was still significant, measuring 7.60 ± 0.72℃. However, an even higher temperature increase was observed at higher concentrations, even though the SAR value was lower. For the dispersion with a concentration of 25 mg/ml, the ΔT reached 24.37 ± 0.88℃.

Material	Fe₃O₄ concentration [mg/ml]	SAR av. [W/g]	SAR error [+/-]	Temperature change [°C]
ckldex M1	25	1.56	0.11	5.23±0.08
ckldex M2	25	2.43	0.26	6.67±0.55
ckldex M3	0.25	227.05	11.42	7.60±0.72
	0.5	160.80	15.87	10.97±0.64
	2	129.62	3.42	24.93±0.51
	25	99.10	6.23	24.37±0.88
ckldex M4	25	8.53	0.37	24.43±0.67

Tab. 1 *Results of magnetic hyperthermia effect measurements for Fe₃O₄ NPs (f=347kHz; H=17kA/m).*

Secondly, the dye adsorption efficiency was evaluated for rhodamine B, crystal violet, and lissamine green as the test dyes. These dyes are zwitterionic, cationic, and

anionic, respectively. Notably, for the materials synthesized using method M3 observed the highest adsorption efficiency for all tested dyes. Additionally, samples for which the modifier was introduced before MNP crystallization showed better adsorption capacity compared to those where the modifier was added after crystallization which can be related to the formation of carbonous shell [9].
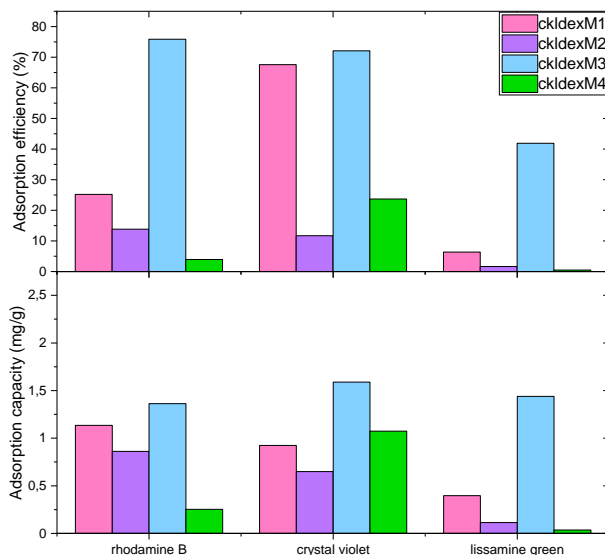
Fig. 2 *Dye adsorption efficiency and capacity of Fe$_3$O$_4$ mod: γ-cyclodextrin.*

Conclusions

Magnetite nanoparticles of varying sizes, coated with cyclodextrin, were successfully synthesized using the high-temperature decomposition method. XRD analysis confirmed that all samples were free of impurities, with average crystallite sizes ranging from 5.5 ± 0.1 nm for nanoparticles synthesized in triethylene glycol to 37.7 ± 0.4 nm for those produced in benzyl ether. The method of γ-cyclodextrin introduction also influenced the concentration of the organic phase. An exceptionally high SAR value of 227.051 ± 11.423 W/g was achieved for ckldex M3 at a low concentration of 0.25 mg/ml. Notably, this concentration also resulted in a significant temperature change of 7.60 ± 0.72°C. Interestingly, although higher concentrations showed lower SAR values, they produced greater temperature increases. For a 25 mg/ml dispersion, a ΔT of 24.93 ± 0.51°C was observed, with heating times differing substantially. Similar to the magnetic hyperthermia effect, ckldex M3 exhibited the highest adsorption efficiency, adsorbing 75.87% of rhodamine B, 72.11% of crystal violet, and 41.90% of lissamine green.

Acknowledgements

References

[1] A. Radoń, A. Włodarczyk, Ł. Sieroń, M. Rost-Roszkowska, A. Ciuraszkiewicz, et al. Influence of the modifiers in polyol method on magnetically induced hyperthermia and biocompatibility of ultrafine magnetite nanoparticles, (123AD).

[2] W.W. Wolak, A. Drzewi, MODELLING OF THE INTERACTIONS BETWEEN MAGNETIC, 21 (2022) 98–106.

[3] C. Caizer, I.S. Caizer, Study on Maximum Specific Loss Power in Fe3O4 Nanoparticles Decorated with Biocompatible Gamma-Cyclodextrins for Cancer Therapy with Superparamagnetic Hyperthermia, Int. J. Mol. Sci. 2021, Vol. 22, Page 10071. 22 (2021) 10071.

[4] I.S. Caizer-Gaitan, C.G. Watz, C. Caizer, C.A. Dehelean, T. Bratu et. al, In Vitro Superparamagnetic Hyperthermia Employing Magnetite Gamma-Cyclodextrin Nanobioconjugates for Human Squamous Skin Carcinoma Therapy, Int. J. Mol. Sci. 25 (2024) 25.

[5] A. Włodarczyk, S. Gorgoń, A. Radoń, K. Bajdak-Rusinek, Magnetite Nanoparticles in Magnetic Hyperthermia and Cancer Therapies: Challenges and Perspectives, Nanomaterials. 12 (2022).

[6] B. Stephen Inbaraj, B.H. Chen, Dye adsorption characteristics of magnetite nanoparticles coated with a biopolymer poly(γ-glutamic acid), Bioresour. Technol. 102 (2011) 8868–8876.

[7] T. Krahnstöver, J. Plattner, T. Wintgens, Quantitative detection of powdered activated carbon in wastewater treatment plant effluent by thermogravimetric analysis (TGA), Water Res. 101 (2016) 510–518.

[8] M. Peiravi, H. Eslami, M. Ansari, H. Zare-Zardini, Magnetic hyperthermia: Potentials and limitations, J. Indian Chem. Soc. 99 (2022) 100269.

[9] A. Lewińska, A. Radoń, K. Gil, D. Błoniarz, A. Ciuraszkiewicz, et al. Carbon-Coated Iron Oxide Nanoparticles Promote Reductive Stress-Mediated Cytotoxic Autophagy in Drug-Induced Senescent Breast Cancer Cells, ACS Appl. Mater. Interfaces. 16 (2024) 15457–15478.

Microscopy Techniques in the Optimization of Nitinol Implants: Surface Modification for Improved Biocompatibility and Durability in the Treatment of Atrial Septal Defect

K.Szawiraacz[1,*], P. Kurtyka[1,2], M.Basiaga[3], Ł. Major[1], R. Major[1,*]

[1] Institute of Metallurgy and Materials Science, Polish Academy of Sciences, 25 Reymonta Street, 30-059, Kraków, Poland;
[2] Institute of Heart Prostheses, Foundation for the Development of Cardiac Surgery, Zabrze, Poland;
[3] Silesian University of Technology, Faculty of Biomedical Engineering, Department of Biomaterials and Medical Devices Engineering, Roosevelta 40 St., 41-800 Zabrze, Poland.

*k.szawiraacz@imim.pl ; r.major@imim.pl

Abstract

The work concerns on the development of surface engineering dedicated to the cardiovascular system through the surface modification of implants designed for closing atrial septal defects (ASD), utilizing the ALD (Atomic Layer Deposition) method. The base elements of these implants are made from shape memory materials such as NiTi (Nitinol). Surface modification is critical as it allows for the retention of the beneficial mechanical properties of nitinol while minimizing its potential negative biological effects. Improving the biocompatibility of implants not only reduces the risk of allergic reactions but also extends their lifespan, directly impacting patient health. The samples were analyzed using a combination of various research techniques, including digital microscopy, scanning electron microscopy (SEM), X-ray diffraction (XRD), and scanning acoustic microscopy (SAM). The integration of these methods allows for a comprehensive analysis of both surface topography and internal residual stresses, enabling a deeper understanding of coating behavior and its influence on the mechanical properties of the samples. XRD provides insights into the distribution of residual stresses in the material, which is essential for assessing the mechanical stability of nitinol-based samples, known for their shape-memory properties. The distribution of residual stresses, which can influence delamination, was measured using X-ray diffraction techniques and correlated with acoustic microscopy images. These images illustrate stress maps that indicate areas at risk of delamination, providing critical insights into the structural stability of the coatings.

Keywords: NiTi alloy, biocompatibility, cardiovascular implant, scanning electron microscopy, X-ray Diffraction

Introduction

Cardiovascular diseases are the leading causes of death worldwide. ASD is a condition where the valve between the left atrium and the left ventricle of the heart does not close properly, causing blood to flow back into the atrium. In advanced cases, implants, such as specialized occluder systems, are necessary to improve valve function [1]. Nitinol is often used in the construction of these implants due to its exceptional mechanical properties. Nitinol is known for its unique characteristics, such as shape memory and superelasticity. The superelasticity of nitinol, or its ability to flexibly adapt to changing environments, is particularly important in the heart. The

heart is a dynamic organ, subjected to continuous fluctuations in pressure and mechanical load. Nitinol-based implants can easily adjust to these conditions, making them ideal for use in the circulatory system, such as in stents or valve repair rings [1,2].

However, despite its generally good biocompatibility, nitinol contains nickel, which can migrate from the surface of the material and cause allergic reactions in some patients. Nickel is a potent allergen, and its presence can lead to localized inflammation and irritation. For this reason, there is ongoing research to improve the biocompatibility of nitinol to reduce the risk of such reactions [2-4].

One of the most promising approaches in this area is surface modification of nitinol. Processes such as the deposition of thin protective layers, for example, metal oxides (such as silicon dioxide), using the ALD (Atomic Layer Deposition) method, aim to create a barrier that prevents nickel from migrating from the nitinol substrate to surrounding tissues. These coatings can also improve adhesion properties and corrosion resistance, further enhancing the durability of implants in the harsh intravascular environment [3-5].

Results and Discussion

Digital microscopy provides a macroscopic image of the topography, allowing for the quick identification of surface irregularities, defects, and the overall shape of the sample. Scanning electron microscopy (SEM) (Fig. 1), with its high resolution, offers more detailed information about the surface morphology.

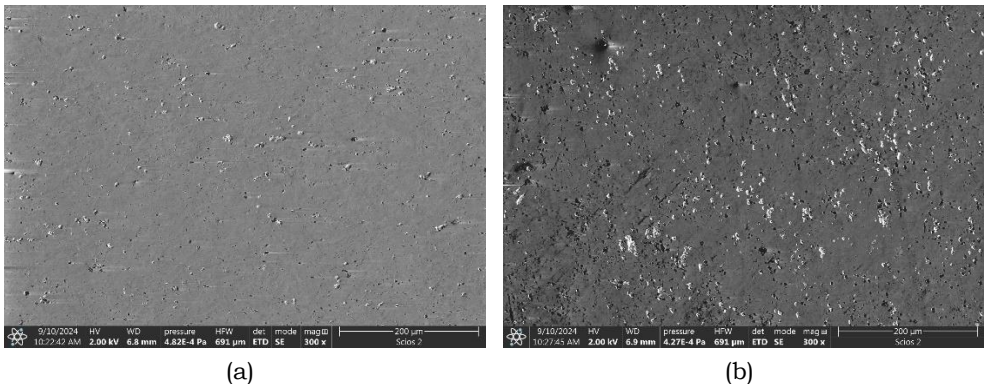(a)   (b)

Fig. 1. Surface topography comparison: (a) NiTi surface; (b) NiTi + ALD coating

The correlation of XRD results with images obtained from acoustic microscopy (Fig. 2) enables the assessment of stress distribution and potential structural defects that could lead to coating delamination.
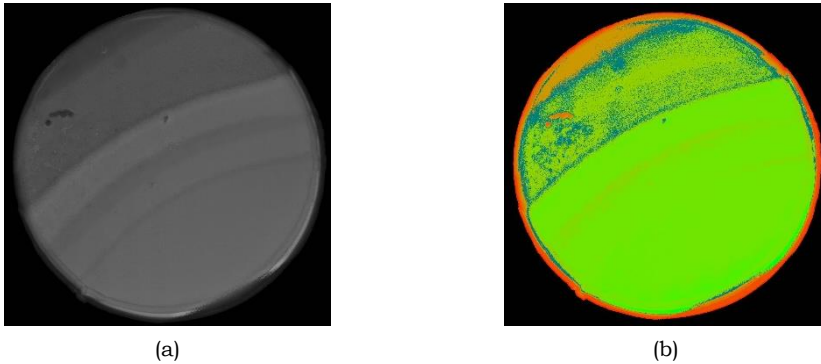
<div align="center">(a)   (b)</div>

Fig. 2. NiTi + ALD coating, SAM – delamination mode: (a) grey view; (b) color view

Conclusions

SEM, due to its high resolution, provides more detailed information about the surface morphology, revealing fine structures and potential cracks in the silicon oxide layer deposited on nitinol.

Changes in residual stress distribution, visible in XRD results, can directly affect the stability of the silicon oxide layer. In regions of high stress, the ALD coating may weaken, potentially leading to delamination, while acoustic microscopy allows for early detection of these defects. High internal stresses can negatively impact the material's durability, and correlating these findings with acoustic microscopy provides crucial insights into areas prone to damage. The correlation between imaging techniques and structural analysis enables a comprehensive understanding of the interaction between topography, residual stresses, and coating adhesion.

Acknowledgements

References

[1] M.J. Van Ligten, D.E. Rappaport, L.B. Querin, W.A. Martini, Atrial Septal Defect (ASD) Repair Unveiling an Unusual Conduction Conundrum: A Wenckebach Case Report., Cureus 16 (2024) e62073. https://doi.org/10.7759/cureus.62073.

[2] C. Constant, S. Nichols, É. Wagnac, Y. Petit, A. Desrochers, V. Braïlovski, Biocompatibility and mechanical stability of Nitinol as biomaterial for intra-articular prosthetic devices, Materialia (Oxf) 9 (2020) 100567. https://doi.org/10.1016/j.mtla.2019.100567.

[3] R. Patel, W. Moore, J.C. Jimenez, Severe symptomatic nickel allergy following stent graft implantation requiring excision and external iliac artery reconstruction., J Vasc Surg Cases Innov Tech 8 (2022) 562–564. https://doi.org/10.1016/j.jvscit.2022.08.013.

[4] A. Bandyopadhyay, I. Mitra, S.B. Goodman, M. Kumar, S. Bose, Improving biocompatibility for next generation of metallic implants, Prog Mater Sci 133 (2023) 101053. https://doi.org/10.1016/j.pmatsci.2022.101053.

[5] M. Jenko, M. Godec, A. Kocijan, R. Rudolf, D. Dolinar, M. Ovsenik, M. Gorenšek, R. Zaplotnik, M. Mozetic, A new route to biocompatible Nitinol based on a rapid treatment with H2/O2 gaseous plasma, Appl Surf Sci 473 (2019) 976–984. https://doi.org/10.1016/j.apsusc.2018.12.140.

Polyelectrolyte Micelles and Erythrocytes as Growth Factor Delivery Systems

J. Więcek-Chmielarz[1]*, W. Kajzer[2] , Ł. Major[1], R. Major[1]*

[1]*Institute of Metallurgy and Materials Science, Polish Academy of Sciences, 25 Reymonta Street, 30-059, Kraków, Poland,*
[2]*Department Of Biomaterials And Medical Devices Engineering, Silesian University Of Technology, Poland*

[*]j.wiecek@imim.pl, major.r@imim.pl

Abstract

Polyelectrolyte micelles and erythrocytes are gaining increasing attention as innovative growth factor delivery systems in regenerative therapy. Polyelectrolyte micelles, due to their ability to self-assemble and encapsulate bioactive compounds, provide precise mechanisms for drug delivery, protecting fragile growth factors from degradation in physiological environments. Erythrocytes, as natural biological carriers, offer biocompatibility, prolonged circulation time, and minimal immunogenicity, making them attractive vehicles for therapeutic molecules. These systems were analyzed using advanced microscopy techniques, providing detailed insights into their structure, stability and interactions, which are crucial for optimizing their performance in medical applications.

Keywords: polyelectrolyte micelles, erythrocytes, drug delivery systems, graft copolymers, scanning electron microscopy (SEM)

Introduction

The development of effective delivery systems is a crucial aspect of modern medicine, particularly in the field of regenerative therapy. Delivery systems are designed to ensure the controlled, targeted and sustained release of therapeutic agents, such as drugs, proteins or growth factors, directly to the site of injury or disease. By improving the stability, bioavailability and protection of these agents, delivery systems enhance therapeutic outcomes and minimize side effects.

Polyelectrolytes are polymers that carry multiple charged groups along their backbone, allowing them to interact with oppositely charged molecules or surfaces [1]. These interactions enable polyelectrolytes to form complexes and structures ideal for encapsulating bioactive substances, which can then be used in various therapeutic applications. Some of the commonly used polyelectrolytes in delivery systems include chitosan, which is a positively charged biopolymer derived from chitin; sodium alginate, a negatively charged polysaccharide extracted from brown seaweed; and chondroitin sulfate, another negatively charged biopolymer found in a cartilage tissue. These polyelectrolytes offer biocompatibility, biodegradability, and the ability to form gels or films, making them highly suitable for use in drug delivery and tissue engineering.

To further enhance the functionality of these materials, grafting techniques are often employed. Grafting refers to the process of chemically attaching specific side chains or functional groups to the main polymer chain to improve properties such as solubility, thermal stability and responsiveness to environmental triggers [2]. One

such grafted polymer is poly(N-isopropylacrylamide) (PNIPAM) [3], which exhibits thermoresponsive behavior, meaning it can change its solubility or conformation in response to temperature changes. This property is highly advantageous in controlled drug release applications, where precise environmental triggers are required.

In addition to synthetic systems, erythrocytes (red blood cells) offer unique potential as natural delivery vehicles [4]. The surface of erythrocytes carries a negative charge, primarily due to the presence of sialic acid residues. This negative charge makes them highly suitable for interaction with positively charged polyelectrolytes, allowing for the formation of stable complexes that can encapsulate growth factors or drugs. Erythrocytes also have a long circulation time in the bloodstream and are biocompatible, which enhances their utility in drug delivery applications.

Results and Discussion

The prepared growth factor delivery systems were visualized using advanced microscopy techniques. In Figure 1, the results obtained from confocal microscopy and SEM for the polyelectrolyte micelles are presented. Three variants of samples were prepared consisting of chitosan-g-PNIPAM and alginate-g-PNIPAM. All samples were cross-linked using NHS/EDC after application. In Figures 1a and 1d, the surfaces of the chitosan-g-PNIPAM/alginic acid-g-PNIPAM samples are presented. In Figures 1b and 1e, the surfaces of the chitosan-g-PNIPAM/alginic-g-PNIPAM samples, to which the growth factor VEGF was applied along with the cross-linking agent, are shown. In Figures 1c and 1f, the surfaces of the chitosan-g-PNIPAM/alginic acid-g-PNIPAM samples on which VEGF was grafted with the final layer of grafted chitosan are presented. A change in the structure of the sample to which VEGF was added along with the cross-linking reagent was observed (Fig. 1b), however, the arrangement of micelles remained uniform across the entire surface of the sample. Figure 2 shows the results for polyelectrolytes $(Chi/CSu)_{12}$ modified with Red Blood Cells (RBCs). Fig. 2 presents a chitosan/chondroitin sulphate coating, where the final layer consisted of: chitosan bound to erythrocytes (Fig. 2a, 2d), chitosan-g-pNIPAM bound to erythrocytes (Fig. 2b, 2e), and chitosan-g-PNIPAM bound to VEGF and erythrocytes (Fig. 2c, 2f). The arrangement of micelles and erythrocytes on samples 2a and 2b are significantly greater than on sample 2c.

a)   b)   c)   200 µm
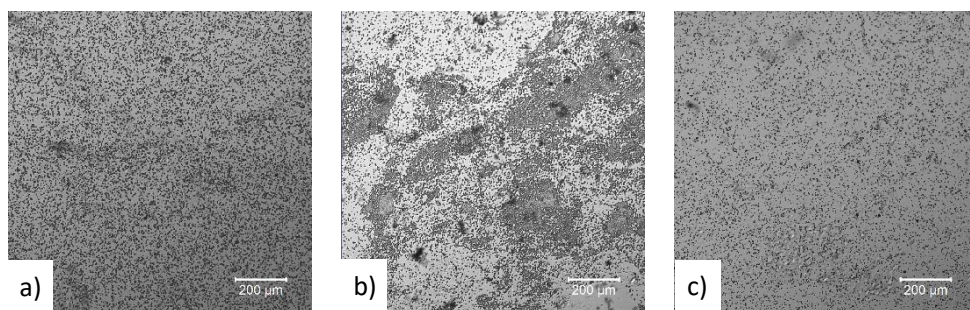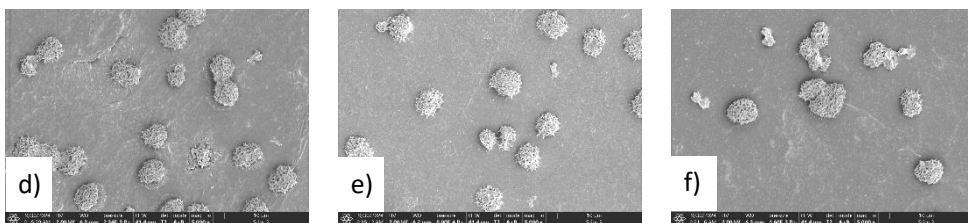
Fig.1*. Polyelectrolytes complex micelles; CLSM magnification 5x: a) (Chi-g/Alg-g)$_{12}$, b) (Chi-g/Alg-g)$_{12}$ VEGF, c) (Chi-g-VEGF/Alg-g)$_{12}$, SEM magnification 5000x: d) (Chi-g/Alg-g)$_{12}$, e) (Chi-g/Alg-g)$_{12}$ VEGF, f) (Chi-g-VEGF/Alg-g)$_{12}$,*
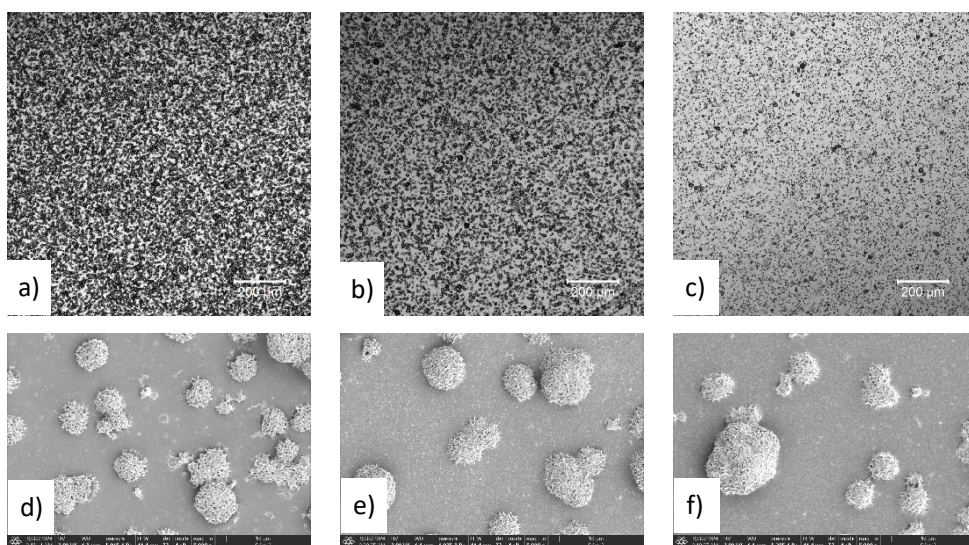
Fig.2*. Polyelectrolytes (Chi/CSu)$_{12}$ modified with Red Blood Cells (RBCs), CLSM magnification 5x, finishing layer: a) RBC Chi, b) RBC Chi-g, c) RBC Chi-g-VEGF, SEM magnification 5000x, finishing layer: d) RBC Chi, e) RBC Chi-g, f) RBC Chi-g-VEGF*

Conclusions

The formed micelles and erythrocytes created a uniform layer on the surface of the sample. No changes were observed in the structure of the micelles to which VEGF was added. The stability and uniformity of the micelles with VEGF suggest a potential application for controlled release systems, where VEGF could be steadily delivered without affecting the carrier's structural properties.

Acknowledgements

References

[1] Picart, C. (2008). Polyelectrolyte multilayer films: From physico-chemical properties to the control of cellular processes. Current Medicinal Chemistry, 15, 685-697

[2] Li, G., Song, S., Zhang, T., Qi, M., & Liu, J. (2013). pH-sensitive polyelectrolyte complex micelles assembled from CS-g-PNIPAM and ALG-g-(P(NIPAM-co-NVP) for drug delivery. International Journal of Biological Macromolecules, 62, 203-210. G

[3] Zhang, T., Li, G., Guo, L., & Chen, H. (2012). Synthesis of thermo-sensitive CS-g-PNIPAM/CMC complex nanoparticles for controlled release of 5-FU. International Journal of Biological Macromolecules, 51(5), 1109-1115.

[4] Zhang, X., Lin, Y., Xin, J., Zhang, Y., Yang, K., Luo, Y., & Wang, B. (2024). Red blood cells in biology and translational medicine: Natural vehicle inspires new biomedical applications. Theranostics, 14(1), 220–248.

Microstructure characterization of rhenium-modified refractory powder materials

A.Czech[1*], A.Wrona[1], Ł. Major[2]

[1]*Łukasiewicz Research Network- Institute of Non-Ferrous Metals, 5 Sowińskiego Street, 44-100, Gliwice, Poland,*
[2]*Institute of Metallurgy and Materials Science, Polish Academy of Sciences, 25 Reymonta Street, 30-059, Kraków, Poland,*

[*]*anna.czech@imn.lukasiewicz.gov.pl*

Abstract

The aim of this study was to characterize the microstructure of refractory powder materials, specifically tungsten-rhenium (W-Re) and molybdenum-rhenium (Mo-Re) in their non-spherical form. The characterization was performed using scanning electron microscopy (SEM), transmission electron microscopy (TEM), energy dispersive spectroscopy (EDS), and nanohardness testing.

Keywords: refractory metals, microstructure, SEM/TEM analysis, EDS analysis

Introduction

In recent years, there has been a growing interest in refractory metals due to their unique properties. Among them, tungsten and molybdenum are becoming promising precursors for Laser Powder Bed Fusion (LPBF) techniques. However, their properties, such as high melting points, high thermal conductivity, and susceptibility to cracking, make them challenging materials for additive manufacturing processes. Refractory elements from groups 5 and 6 of the periodic table possess a body-centered cubic (BCC) structure, which indicates strong atomic bonds—an unfortunate characteristic when it comes to printability. One potential solution to this issue is modifying the microstructure by altering the chemical composition of the powders. Among the various elements that can form solid solutions with tungsten and molybdenum, rhenium (Re) is a significant alloying addition. The so-called "rhenium effect" has been shown to improve low-temperature ductility in Group VIA metals, which possess BCC crystal structures. Unlike other refractory metals, rhenium has a hexagonal close-packed (HCP) structure, offering a distinct set of properties. The objective of this study was to characterize the microstructure of irregular tungsten and molybdenum powders modified with rhenium. These powders were produced through a thermoreduction process of ammonium perrhenate, developed at the Łukasiewicz Research Network - Institute of Non-Ferrous Metals. Microstructural analysis of the powder surface morphology was performed using scanning electron microscopy (SEM) with a secondary electron (SE) detector. Additionally, thin foils were prepared from individual powder particles for analysis on the cross-section by transmission electron microscopy (TEM). This allowed for detailed microstructural characterization in bright field (BF) mode, phase analysis using the selected area electron diffraction pattern (SAEDP) technique, and qualitative elemental distribution mapping via energy dispersive spectroscopy (EDS). Nano-indentation tests were conducted to determine the mechanical properties of the powders, including nanohardness. For this purpose, metallographic samples were prepared by embedding the powders in resin. Eight different types of powders were analyzed: irregular W, Mo, W-Re, and Mo-Re, as well

as spherical W, Mo, W-Re, and Mo-Re, all manufactured by the Łukasiewicz-IMN through a plasma spheroidization process.

Results and Discussion

W+Re- irregular powder

The non-spherical W-Re powder consisted of irregular particles with visible small particles on the surface—tungsten grains covered with metallic rhenium (Fig. 1). Rhenium was distributed on the tungsten in the form of a thin (approximately 0.1 µm) layer, as shown in the cross-section using the TEM BF technique. Its structure was nanocrystalline, as evidenced by the ring-shaped SAEDP pattern (Fig. 2). Additionally, a layer of oxygen was identified between the rhenium layer and the tungsten particle, which may indicate the presence of surface tungsten oxide (Fig. 3).

Fig. 1. *Surface topography image of W-Re non-spherical powder obtained by SEM SE technique*
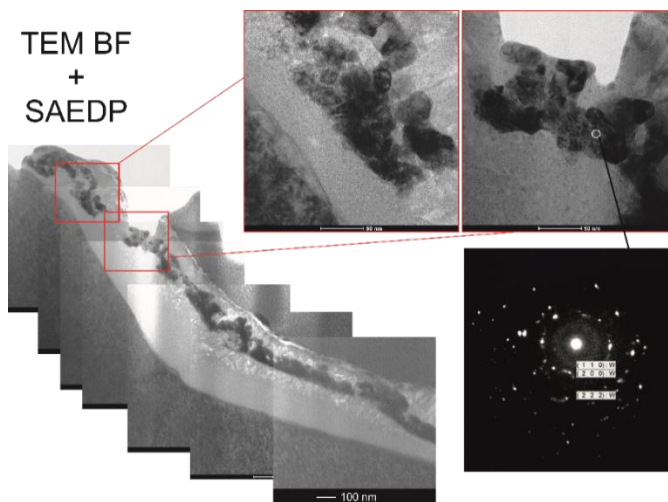
Fig. 2. Microstructure characterization of the W-Re non-spherical powder done by TEM BF & SAEDP pattern on the cross-section
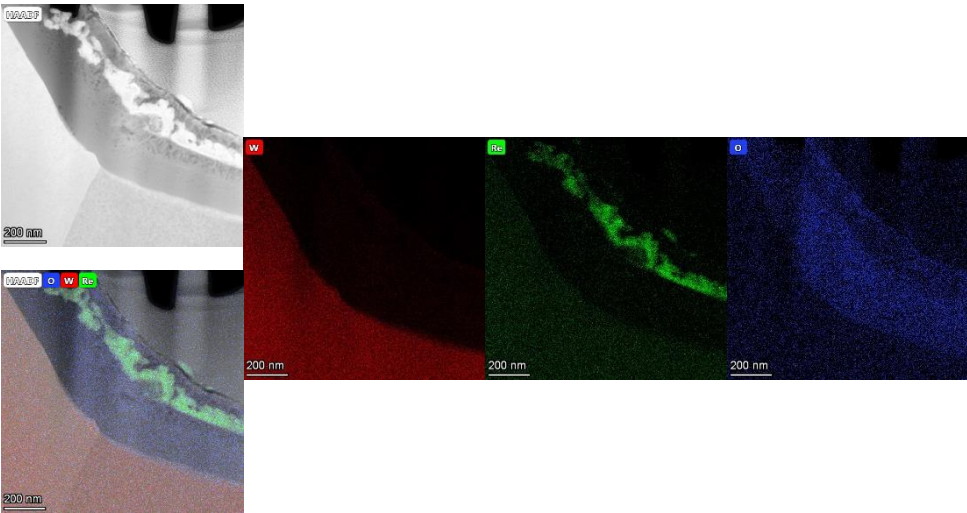
Fig. 3. *Qualitative chemical analysis of W-Re non-spherical powder done by EDS technique*

Mo+Re- irregular powder

The non-spherical Mo-Re powder consisted of irregular, flake-like particles, with visible small particles on the surface—molybdenum grains covered with metallic rhenium (Fig. 4). Rhenium was distributed on the molybdenum in the form of a thin (approximately 0.1 µm) layer, as shown in the cross-section using the TEM BF technique. Its structure, similar to that of the W-Re powder, was nanocrystalline, as evidenced by the ring-shaped SAEDP pattern (Fig. 5). Additionally, a layer of oxygen was identified between the rhenium layer and the molybdenum particle, which may indicate the presence of surface molybdenum oxide (Fig. 6). It was also shown that rhenium was distributed throughout the pores present in the molybdenum powder.
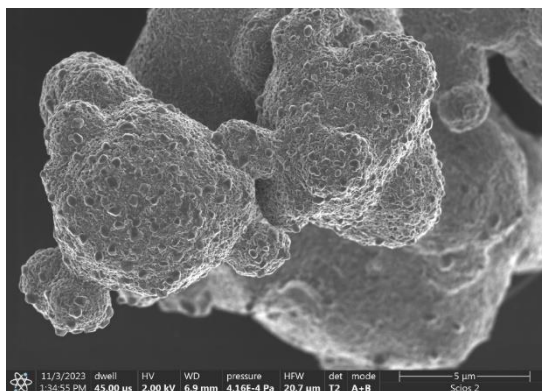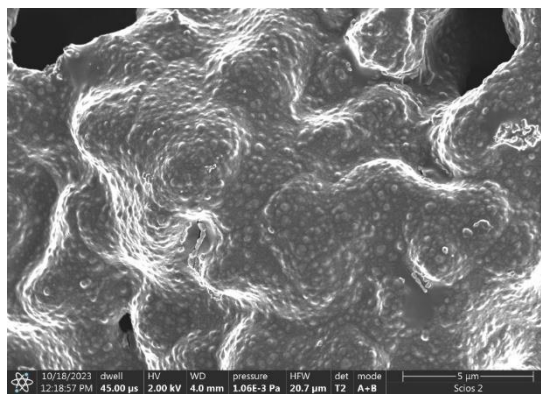

Fig. 4. *Surface topography image of Mo-Re non-spherical powder obtained by SEM SE technique [5]*
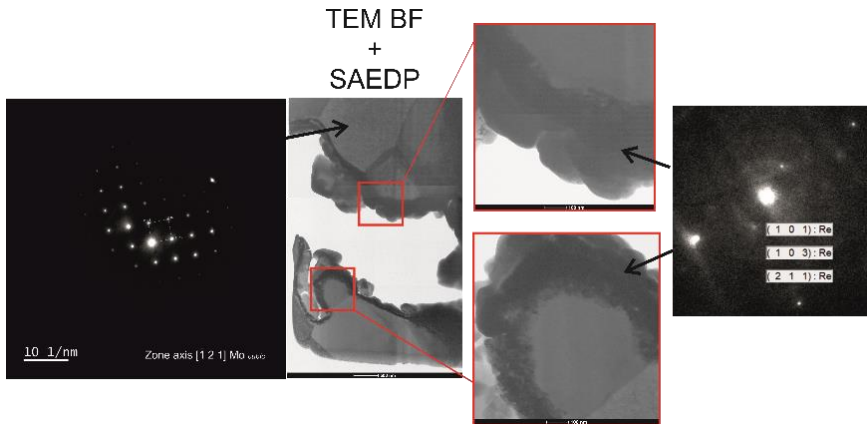
Fig. 5. *Microstructure characterization of the Mo-Re non-spherical powder done on the cross- section by TEM BF & SAEDP [5]*
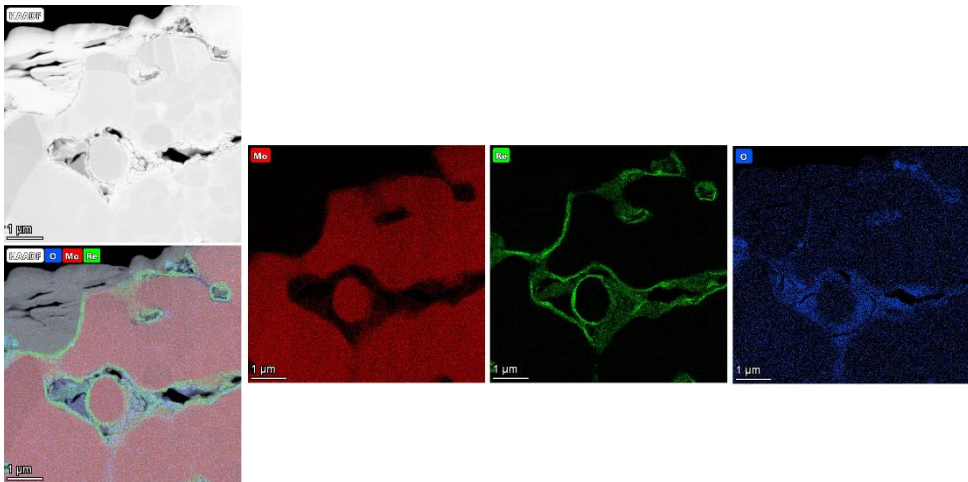
Fig. 6. *Qualitative chemical analysis of Mo-Re non-spherical powder done by EDS technique [5]*

Grain nanohardness and Young's modulus

The detailed results of the nanohardness are presented in Fig. 7, providing insights into the mechanical properties of the tested materials. Additionally, based on the nanohardness measurements, the Young's modulus was calculated for each material, as shown in Fig. 8. Among the tested materials, spherical powders exhibited higher nanohardness compared to their irregular counterparts of the same composition. However, spherical powders with the addition of rhenium demonstrated lower nanohardness than pure spherical W and Mo powders, confirming that the addition of rhenium enhances the material's plasticity.
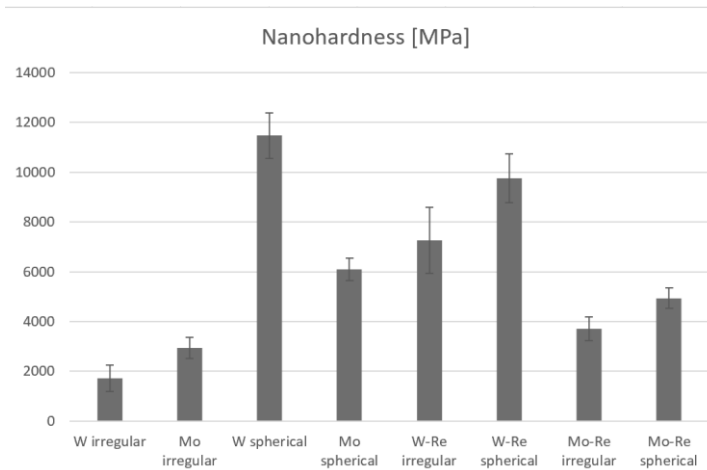
Fig. 7. *Nanohardness test results with standard deviation*
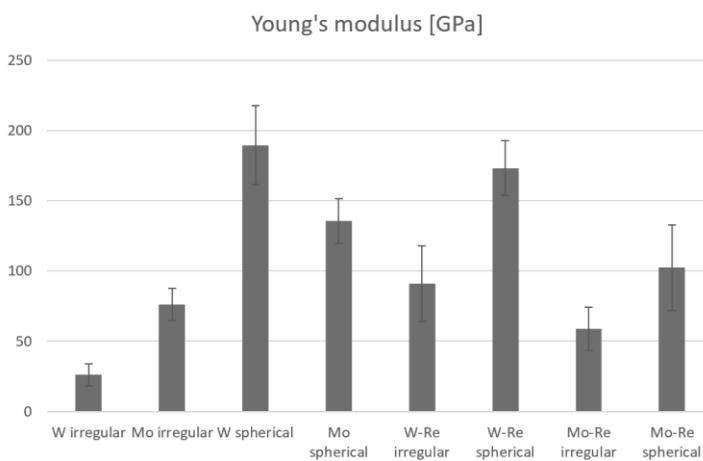
Fig. 8. *Young's modulus with standard deviation*

Conclusions

On the surface of irregular molybdenum powder, after the thermal reduction of ammonium perrhenate in a hydrogen atmosphere, a deposited layer of rhenium and a thin layer of oxygen are visible. In the case of irregular tungsten powder, rhenium is separated from the surface by a thicker oxygen layer. This could be attributed to slight surface oxidation occurring during powder storage. Micromechanical tests indicate that the plasma spheroidization process, along with the associated phenomenon of rhenium volume diffusion, reduces both the average hardness and Young's modulus values. For Mo and Mo-Re spherical powders, the Young's modulus decreased by over 30 GPa, while for W and W-Re spherical powders, the decrease was

approximately 16 GPa. This reduction may be beneficial in mitigating the brittle fracture phenomena typically associated with Mo and W.

Acknowledgements

References

[1] P. Jéhanno, M. Böning, H. Kestler, M. Heilmaier, H. Saagem, M. Krüger, Molybdenum alloys for high temperature applications in air, Powder Metallurgy 51.2, 99-102 (2008), https://doi.org/10.1179/174329008X313379

[2] J. Braun, L. Kaserer, J. Stajkovic, K.-H. Leitz, B. Tabernig, P. Singer, P. Leibenguth, C. Gspan, H. Kestler, G. Leichtfried, Molybdenum and tungsten manufactured by selective laser melting: Analysis of defect structure and solidification mechanisms, International Journal of Refractory Metals and Hard Materials, Volume 84, November (2019), 104999, https://doi.org/10.1016/j.ijrmhm.2019.104999

[3] E. Lassner, W-D. Schubert, Tungsten. Properties, Chemistry, Technology of the Element, Alloys, and Chemical Compounds, Springer New York, NY, book (2012), https://doi.org/10.1007/978-1-4615-4907-9

[4] P. Rebesan, M. Ballan, M. Bonesso, A. Campagnolo, S. Corradetti, R. Dima, C. Gennari, G.A. Longo, S. Mancin, M. Manzolaro, G. Meneghetti, A. Pepato, E. Visconti, M. Vedani, Pure molybdenum manufactured by Laser Powder Bed Fusion: Thermal and mechanical characterization at room and high temperature, Additive Manufacturing, Volume 47 (2021), 102277, https://doi.org/10.1016/j.addma.2021.102277.

[5] A.Czech. A.Wrona, M.Lis. M.Kot, Ł.Major, Microstructure characterization of refractory powder materials for LPBF method, Archives of metallurgy and materials, special issue paper EM 2024 (submitted)

Hard anodic oxide coatings modified with Si_3N_4 and Al_2O_3 nanoparticles produced by duplex method

A. Kozik[1,2*], M. Nowak[1], K. Limanówka[1], A. Trelka-Druzic[2], Ł. Maj[2],A. Góral[2]

[1] *Institute of Non-Ferrous Metals, 19 Piłsudskiego Street, 32-050 Skawina, Poland*
[2]*Institute of Metallurgy and Materials Science, Polish Academy of Sciences, 25 Reymonta Street, 30-059 Kraków, Polska*
*Anna.Kozik@imn.lukasiewicz.gov.pl

Abstract

The growing consumption of aluminium and its alloys in various industries in recent years has resulted in a growing interest and demand for hard anodic oxide coatings with with even better tribological and mechanical properties. Due to the characteristic structure of the oxide film, the surface of the hard anodic oxide coating has absorptive capacity. Therefore, it can be modified by incorporating hard particles (Al_2O_3, Si_3N_4) [1-2]. Silicon nitride (Si_3N_4) is characterized by high hardness, wear resistance and chemical inertness, it increases microhardness, reduces the friction coefficient and improves the corrosive properties of anodic oxide coatings produced on aluminum [1]. The greatest advantage of aluminum oxide nanoparticles (Al_2O_3) is their high hardness and beneficial effect on improving the corrosive properties of coatings [3]. There are two main methods for introducing modifying particles into anodic oxide coatings: one involves forming a separate particle layer on the coating's surface through techniques like spraying or ultrasonic impregnation [4], while the other incorporates particles directly into the porous structure during the anodizing process by adding them to the anodizing solution [5]. Due to the very small diameter of the pores, nanometric particles are used as modifying particles. In the case of particles of this size, a very big problem is the phenomenon of particle agglomeration. In order to eliminate this phenomenon, appropriate surfactants are selected.

The analysis of the obtained zeta potential values showed that the surfactant DSS had a beneficial effect on the increase of the absolute value of zeta potential, and thus on the improvement of stability and limitation of agglomeration of nanoparticles in the solution containing Al_2O_3 and Si_3N_4 nanoparticles.

Hard anodic oxide coatings modified with hard nanoparticles such as Si_3N4 and Al_2O_3 were produced on aluminum alloy 5754. In the first stage, a hard anodic oxide coating was produced from a 0.3M oxalic acid solution, which was then subjected to an ultrasonic impregnation process in a nanoparticles suspension. The modification of the coating with Si_3N_4 nanoparticles has led to an improvement in wear resistance and microhardness compared to the commercially produced coating.

Keywords: anodizing, wear resistance, nanocomposite coatings, tribolayer

Acknowledgements

References

[1] Mohammadi, A. Afshar, and S. Ahmadi, "Al2O3/Si3N4 nanocomposite coating on aluminum alloy by the anodizing route: Fabrication, characterization, mechanical properties and electrochemical behavior," Ceram Int, vol. 42, no. 10, pp. 12105–12114, Aug. 2016, doi: 10.1016/j.ceramint.2016.04.142.

[2] X. Lu, C. Blawert, N. Scharnagl, and K. U. Kainer, "Influence of incorporating Si3N4 particles into the oxide layer produced by plasma electrolytic oxidation on AM50 Mg alloy on coating morphology and corrosion properties," Journal of Magnesium and Alloys, vol. 1, no. 4, pp. 267–274, Dec. 2013, doi: 10.1016/j.jma.2013.11.001.

[3] Dingfei Zhang, Yinning Gou, Yuping Liu, Xingxing Guo, A composite anodizing containing superfine Al2O3 particles on AZ31 magnesium alloy, Surface & Coatings Technology 236 (2013) 52-57.

[4] J. Sun, L. Weng, and Q. Xue, "Duplex treatment for surface improvement of 2024 Al."

[5] S. Chen, C. Kang, J. Wang, C. Liu, and K. Sun, "Synthesis of anodizing composite films containing superfine Al 2 O 3 and PTFE particles on Al alloys," Appl Surf Sci, vol. 256, no. 22, pp. 6518–6525, Sep. 2010, doi: 10.1016/j.apsusc.2010.04.040.

An attempt of AgTi and CuTi intermetallic phases manufacturing by mechanical alloying from different substrates.

W. Gozdur[1*], M. Pęska[2], A. Baran[2], M. Polański[2], A. Wierzbicka-Miernik[1], A. Dębski[1]

[1]Institute of Metallurgy and Materials Science, Polish Academy of Sciences, 25 Reymonta Street, 30-059, Kraków, Poland,
[2]Department of Functional Materials and Hydrogen Technology, Military University of Technology, 2 Kaliskiego St., 00-908 Warsaw, Poland.

[*]w.gozdur@imim.pl

Abstract

This study presents an attempt to use mechanical alloying in a planetary ball mill to prepare two intermetallic phases, namely AgTi and CuTi. Two approaches were chosen. The first one involved the preparation of samples from pure elements. For the second one, titanium hydride was used instead of titanium. The morphology of the prepared samples and the phase composition were evaluated using scanning electron microscopy (SEM) and X-ray diffraction (XRD) techniques. It was found that using titanium hydride powder instead of pure titanium improves milling efficiency and allows for greater material recovery from the vial (lower losses due to the permanent sticking of cold-welded material to the vial). The prepared samples were also characterized using differential scanning calorimetry (DSC) to verify the phase transition temperatures. The obtained DSC curves show transition temperatures that are in good agreement with those that can be read from the available phase diagrams. The obtained results suggest that the mechanical alloying method can be successfully used to prepare alloys with dominating amounts of desired intermetallic phases however, single-phase materials were not obtained.

Keywords: mechanical alloying, binary alloys, SEM, XRD, DSC.

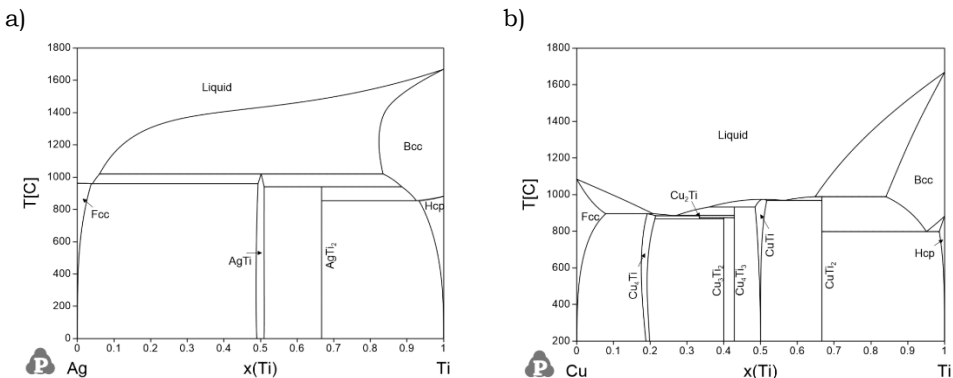*Fig.1*. Binary phase diagrams [1]: a) Ag-Ti system, b) Cu-Ti system.

Acknowledgments

References

[1] Binary phase diagrams calculated by Pandat software; content available online: https://computherm.com/phase_diagrams (Access 01/09/2024).

Effect of densification methods on the microstructure and mechanical properties of bulk TiN

J. Kasprzycki[1,*], K. Stan-Glowinska[1], A. Sypien[1], G. Garzel[1], P. Klimczyk[2], A. Jarzebska[1], L. Rogal[1]

[1]*Institute of Metallurgy and Materials Science, Polish Academy of Sciences, 25 Reymonta Street, 30-059, Kraków, Poland*
[2]*Institute of Metal Cutting, 37A Wroclawska Street, 30-011, Kraków, Poland*

[*]*j.kasprzycki@imim.pl*

Abstract

Spark plasma sintering (SPS) and high pressure high temperature (HPHT) were used to investigate different consolidation conditions on the titanium nitrides microstructure. TiN input powder was previously obtained in a mechanical alloying (MA) experiment. Microstructure investigation of sample consolidated in spark plasma sintering method resulted in grain grown up to 4,8 ± 1,6 µm while, high pressure used in both HPHT processes preserved nanograins of TiN. However, phase and microstructure examinations proved existence of another phase. The Vickers hardness and compression test were used to investigate the mechanical properties of bulk materials. Mechanical properties of bulk materials were investigated in Vickers hardness test and compression test. Highest values of mechanical properties were achieved for TiN sintered in SPS method. Vickers hardness reached 1796 [Hv5] while, compressive stress 2416 [MPa].

Keywords: sintering, powder metallurgy, Titanium nitride, HPHT, SPS

Introduction

Titanium nitride still arouses great interest mainly due to its high hardness, and friction coefficient values, which makes it a suitable candidate for cutting tools and as a reinforcement phase in composite materials [1,2]. Nitride powders can be synthesized in various powder metallurgy methods, such as chemical reactions, reaction with ammonia gas flow and mechanical alloying (MA). Mechanical alloying attracts attention due to combination of high temperature, pressure and deformation rate. Moreover, MA allows reaction between powders and gas within the reactor.

Expansion of nanomaterials and nanocomposites has emerged important step in modern material science. These nanocomposites stand out in higher yield strength, hardness [3], and creep resistance [4]. The development of bulk nanocomposites by consolidation of nanosized powders is an important processing technique. However, main problem is grain coarsening which causes loss of unique microstructure. Commonly to perform densification the SPS and HPHT methods are used in a range of 500-2250 °C [5,6]. However, temperatures above 1000-1100 °C results in recrystallization and grain growth of nanosized TiN [7]. Some studies focusing on HPHT densification proved that high pressure allows for a decrease in the temperature of the process. Densification under 4 GPa and 1100-1200 °C preserves the initial microstructure [8]. The aim of this reaction is to obtain bulk nanograin TiN characterized by high mechanical properties.

Methodology

TiN powder has been produced using in MA of pure Ti(α) within 3 bar of nitrogen pressure, the milling procedure lasted for 40 h. Synthesized powder consist of clusters of average size 2,1 ± 0,6 μm and submicron particles. Further investigation using electron microscopy proved existence of nanoparticles of average size ~21 nm. Characterized powder was used in this experiment as the input powder to consolidation procedure. Details of consolidation processes were shown in ***Tab. 1***. Microstructure of both input powder and sintered materials were investigated in usage on optical microscopy (OM), scanning electron microscopy (SEM) and transmission electron microscopy (TEM). Phase composition was evaluated using X-ray diffraction (XRD) CoKα (λ = 1,789) radiation source in range 20-120 (2θ°). Mechanical properties were measured in Vickers hardness (Hv5) and compression test.

Tab. 1*. Sintering conditions.*

Lp.	Sintering method	Temperature [°C]	Pressure [MPa]	Time [min]
1	SPS	1600	50	10
2	HPHT	1300	8000	1
3	HPHT	1600	8000	1

Results and Discussion

XRD patterns of starting powder and bulk samples were shown in **Fig. 1**. Input powder obtained from MA consists mainly of TiN Fm$\overline{3}$m however, residual Ti(α) P6$_3$/mmc can also be identified. In case of sample obtained after SPS sintering single TiN Fm$\overline{3}$m phase can be detected. In HPHT samples additional peaks of Ti(α) P6$_3$/mmc phase was identified. In comparison with the initial powder changes in lattice constant is observed what is connected with nitrogen diffusion and dislocation density.
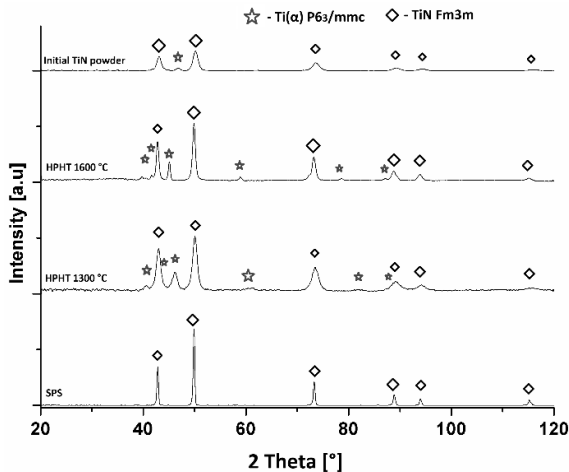
Fig. 1. *XRD diffraction patterns of initial powder, after both HPHT and SPS sintering procedures.*

SEM micrographs presented in **Fig. 2. a-c** depicts the microstructure after both densification techniques. It is clearly visible that titanium nitride grains grown up to 4,8 ± 1,6 μm. Different contrast of individual grains seem to be attributed to different orientations. Between grains other white phase can be noted, further investigation confirms that contains mainly iron previously worn of during MA and diffused into grain boundaries during sintering. Microstructure sintered in both variants of HPHT is much different (**Fig. 2 b, c**). Two different areas can be recognized, circular shape and the matrix area. Mentioned regions differs from each other nitrogen concentration. Circular areas visible in the microstructure of sample sintered at 1600 °C are slightly different in comparison to sample sintered at 1300 °C, there are visible bands at the edge of those areas suggesting early stage of diffusion occurring.
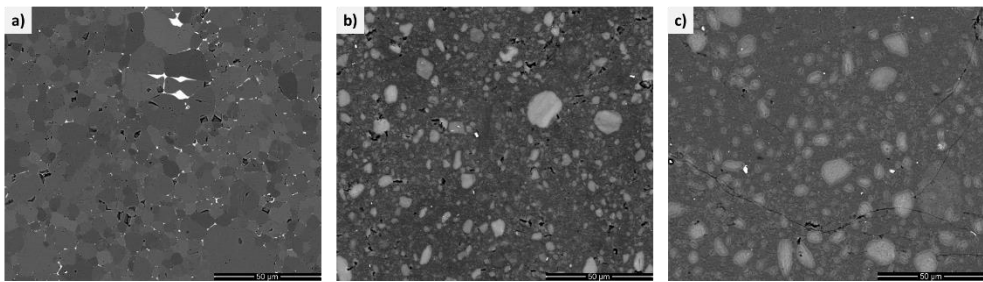
Fig. 2. *SEM micrographs of consolidated samples* **a)** *SPS,* **b)** *HPHT 1300 °C,* **c)** *HPHT 1600 °C.*

Based on TEM bright field studies **(Fig 3 a-c)** the average size of TiN crystals was 23,1 and 27,1 nm for sintering temperatures of 1300 and 1600 °C respectively. However, the region originating from circular areas visible in SEM micrographs has been identified as hexagonal structure of Ti(α) $P6_3/mmc$ enriched with nitrogen.
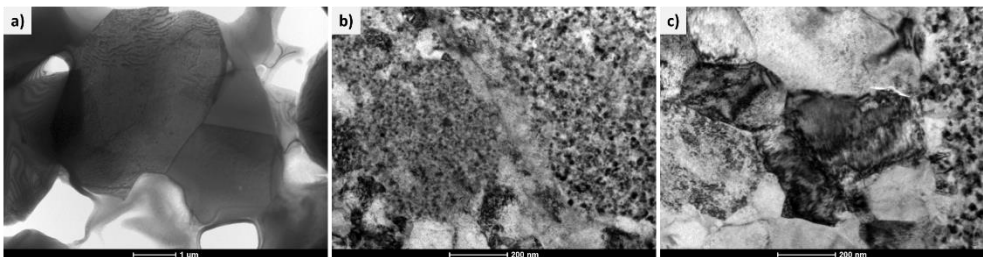
Fig. 3. *TEM-BF images of microstructures of* **a)** *SPS,* **b)** *HPHT 1300 °C,* **c)** *HPHT 1600 °C.*

The Highest mechanical properties were obtained for the sample consolidated via SPS method. At the same time, both samples reached similar values in term of hardness and compression test (**Tab. 2).**

Tab. 2. Mechanical properties of bulk samples.

Sintering method	Temperature [°C]	Pressure [MPa]	Time [min]	Hardness [Hv5]	Compression stress [MPa]
SPS	1600	50	10	1796	2416
HPHT	1300	8000	1	1441	1779
HPHT	1600	8000	1	1538	1624

Conclusions

This experiment used different consolidation methods to investigate their influence on the microstructure and mechanical properties. The SPS method resulted in grain-grown and homogeneous microstructure. HPHT resulted in initial microstructure preservation. It is caused by shorter consolidation time and high pressure which can limit diffusion rate during sintering. Highest compression stress was reached for SPS sample probably due to the more equalized microstructure.

Acknowledgements

References

[1] E. Santecchia, A.M.S. Hamouda, F. Musharavati, E. Zalnezhad, M. Cabibbo, and S. Spigarelli, Wear resistance investigation of titanium nitride-based coatings, Ceramics International, vol. 41, no. 9. Elsevier Ltd, pp. 10349–10379, 2015.
[2] A. Franczak and J. Karwan-Baczewska, COPPER MATRIX COMPOSITES REINFORCED WITH TITANIUM NITRIDE PARTICLES SYNTHESIZED BY MECHANICAL ALLOYING AND SPARK PLASMA SINTERING, *Metallurgy and Foundry Engineering*, vol. 43, p. 97, 2017.
[3] V.V. Dabhade, T.R. Rama Mohan, P. Ramakrishnan, Sintering behavior of titanium-titanium nitride nanocomposite powders, Journal of Alloys and Compounds Vol. 453, 215-221, 2008.
[4] Ch. Yang, L. Cao, Y. Gao, P. Cheng, P. Zhang, J. Kuang, J. Zhang, G. Liu, J. Sun, Nanostructural SC-based hierarchy to improve creep resistance of Al-Cu alloys, Materials and Design, Vol 186, 2020.
[5] H. Kuwahara, N. Mazaki, M. Takahashi, T. Watanabe, X. Yang, T. Azawa, Mechanical properties of bulk sintered titanium nitride ceramics, Materials Science and Engineering: A, Vol. 319-321. 687-691, 2001.
[6] U.W. Blab, T. Barsukova, M.R. Schwarz, A. Kohler, C Schimpf, I.A. Petrusha, U. Muhle, D. Rafaja, E. Kroke, Bulk titanium nitride ceramics – Significant enhancement of hardness by silicon nitride addition, nanostructuring and high pressure sintering, Journal of the European Ceramic Society, Vol 35, 2733-2744.
[7] O.N. Kaidash, Special features of structural transformations in sintering a nanodispersed monophase powder of titanium nitride produced by plasmachemical synthesis, Journal of Superhard Materials vol. 32, 236-249, 2010.
[8] V.S. Urbanovich, Properties of nanocrystalline titanium nitride-based materials prepared by high-pressure sintering, 169-176, 2001.

Effect of Co and Cu doping on mechanical bending response of Ni-Mn-Ga melt-spun ribbons

M. Kowalska[1, *], P. Czaja[2], Ł. Rogal[1], M.J. Szczerba[1]

[1]*Institute of Metallurgy and Materials Science, Polish Academy of Sciences, 25 Reymonta Street, 30-059, Kraków, Poland,*
[2] *Department of Materials Science and Engineering, Stanford University, Stanford, CA, 94305, USA*

[*]*m.kowalska@imim.pl*

Abstract

The study reports on the effect of Co and Cu doping and wheel velocity on the mechanical behavior of Heusler Ni-Mn-Ga melt-spun ribbons during cyclic bending tests. X-ray diffraction measurements revealed a presence of solely $L2_1$ austenite parent phase in the melt-spun ribbons with 1 at. % of Co and Cu, regardless of the wheel's linear velocity. However, increasing the alloying concentration to 6 at. % of Co and Cu led to changes in phase composition to a non-modulated martensite phase (NM). Such alterations of crystal structure resulted in different mechanical response of Ni-Mn-Ga-based ribbons during bending. For the ribbons containing 1 at. % of Co and Cu, deformation was purely pseudo-elastic, while those with the NM phase exhibited both plastic and elastic contribution. Additionally, the study found that the highest plastic strain occurred in the ribbons produced at 5 m/s, while the lowest was seen in the ribbons fabricated at 20 m/s. These findings are significant for the design and optimization of functional Heusler materials exhibited magnetic field-induced bending effect.

Keywords: ferromagnetic shape memory alloys, mechanical bending experiments, melt-spinning

Introduction

Heusler alloys based on Ni-Mn-Ga are a group of smart materials, which have gathered significant attention due to their potential in various applications such as sensors, actuators, magnetic refrigeration, and energy harvesting systems [1]. This multifunctionality is largely due to the unique interaction between the magnetic and mechanical properties of these materials, known as the magnetic field-induced strain effect (MFIS), first documented by Ullakko et al. [2]. This effect involves the reorientation of martensite variants through twin boundary motion [3]. In ternary Ni-Mn-Ga alloys, MFIS has been observed predominantly in 10-layered (10M) and 14-layered (14M) modulated martensite phases, yielding strain values of about 7% and 11%, respectively [4,5]. However, Sozinov et al. demonstrated that by adding Cu and Co to these alloys, the MFIS effect could also be achieved in non-modulated (NM) martensite phases, resulting in a strain of up to 12% [6]. Cobalt reduces the tetragonality of the martensite unit cell, thus lowering the twinning stress, while copper raises the martensitic transformation temperature, making these alloys suitable for high-temperature applications [7,8]. Among the various fabrication methods, melt-spinning has been used to produce Heusler alloys in the form of thin ribbons with high length-to-width ratios, which hold considerable promise for diverse uses. Recent studies have shown that Ni-Mn-Ga-Co-Cu ribbons exhibit not only MFIS,

but also a magnetic field-induced bending (MFIB) effect [9]. Mechanical properties of these alloys are highly influenced by the parameters of the melt-spinning process, particularly the linear velocity of the copper wheel [10]. In addition, various concentration of Co and Cu additives can lead to changes in phase composition and affect mechanical response of Ni-Mn-Ga melt-spun ribbons. Therefore, the main goal of this work was to investigate wheel velocity as well as chemical composition dependence of mechanical properties studied during bending experiments.

Materials and methods

A cylindrical ingot with the nominal composition $Ni_{50-x}Mn_{25}Ga_{25-x}Co_xCu_x$ (at. %, x = 1 and 6) was first produced through induction melting in an argon atmosphere, using high-purity elements: Ni (99.9%), Mn (99.9%), Ga (99.99%), Co (99.9%), and Cu (99.99%). Afterward, the ingot was homogenized at 1173 K for 72 hours under vacuum to achieve a consistent chemical composition. Utilizing the melt-spinning technique, ribbons of two nominal compositions of $Ni_{49}Mn_{25}Ga_{24}Co_1Cu_1$ (denoted as Co_1Cu_1) and $Ni_{44}Mn_{25}Ga_{19}Co_6Cu_6$ (denoted as Co_6Cu_6), were fabricated at varying copper wheel linear velocities of 5, 10, 15 and 20 m/s. Phase composition of the ribbons produced at these different velocities and with various Co and Cu concentrations were analyzed at room temperature using a Bruker D8 X-ray diffractometer (XRD) with CoKα radiation. To verify the chemical composition, energy dispersive spectroscopy (SEM/EDS) was used. Mechanical bending tests were then conducted on the melt-spun ribbons, with each sample subjected to up to 10 bending cycles at a strain rate of 0.1 mm/s. These tests were performed using an Instron machine equipped with precise instrumentation. The ribbons were securely fixed between two aluminum blocks using carbon tape, ensuring that the ribbon surface remained perpendicular to the blocks. Ribbon samples were prepared to have a length of 10±2 mm from the clamping point for each bending test. The bending procedure involved displacing the cantilever by 5 mm, with a constant distance of 7 mm between the fixed side of the ribbon and the cantilever.

Results and Discussion

The chemical composition of the ribbons with 1 and 6 at. % of Co and Cu was measured as $Ni_{49.0}Mn_{26.7}Ga_{22.8}Co_{0.8}Cu_{0.7}$ and $Ni_{44.6}Mn_{25.7}Ga_{17.9}Co_{5.9}Cu_{5.9}$, with corresponding valence electron concentration per atom (e/a) of 7.602 and 7.976, respectively. The as-spun ribbons had a mean thickness of approximately 140 µm, 76 µm, 55 µm and 38 µm for wheel velocity of 5 m/s, 10 m/s, 15 m/s and 20 m/s, respectively. X-ray diffraction measurements revealed that the crystal structure of the Co_1Cu_1 ribbons was found to be solely L2$_1$ cubic structure (parent austenite phase), Fig.1a. X-ray diffraction pattern obtained for the ribbons produced at highest wheel velocity of 20 m/s displayed a peak intensity resembling randomly oriented grains as in powder material. This phenomenon is likely due to the rapid crystallization, which did not allow enough time for a distinct crystallographic texture to form. Further alloying up to 6 at. % of Co and Cu led to significant changes in phase composition of melt-spun ribbons (Fig.1b). X-ray diffraction data revealed that ribbons produced at 5 and 10 m/s were consisted solely of tetragonal, non-modulated (NM) martensite phase. At higher linear velocities of 15 and 20 m/s, coexistence of NM and L2$_1$ phase was observed. This can be attributed to the fact that producing ribbons at lower linear velocities led to the stabilization of the NM martensite phase, due to the presence of larger grain size resulting from the slower cooling rate during melt-spinning process.
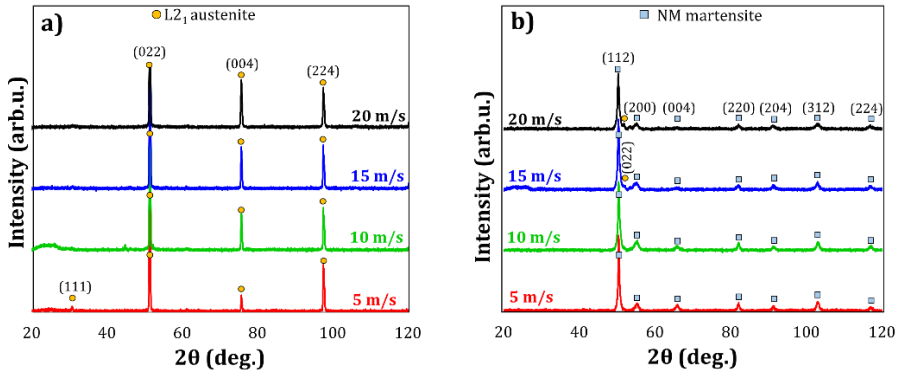
Fig.1. X-ray diffraction data of Co₁Cu₁ (a) and Co₆Cu₆ (b) melt-spun ribbons, produced at different linear velocities of the copper wheel.

Mechanical experiments revealed that there was a strong dependence between chemical composition of melt-spun ribbons and their deformation behavior upon cycling bending. Fig.2a depicted load vs. displacement curves recorded for the first and tenth cycle for the ribbons with 1 at. % of Co and Cu. In each cycle of mechanical test, the cantilever shifted along the ribbon's surface as the load was applied, leading to an increase in the load. When the displacement reached 5 mm, the ribbon achieved its maximum bend position. It is important to note that, regardless of the linear velocity or bending cycle, the melt-spun ribbons returned to their original position during unloading. This behavior is attributed to the presence of only the $L2_1$ austenitic phase in the ribbon's microstructure, which appears to deform exclusively through pseudo-elastic deformation. During mechanical bending, austenite grains either undergo compression or tension based on the side of the ribbon, leading to the accumulation of elastic energy in the material. This energy causes the ribbon to return to its original position upon unloading, allowing for reversible bending. In contrary, the deformation of the melt-spun ribbons in the martensitic state was found to involve both plastic and elastic components (Fig.2b). The majority of plastic deformation occurred during the first bending cycle. This suggests that in the initial loading cycle, the microstructure experiences martensite variant reorientation via twinning mechanism. In subsequent cycles, the load was applied to a ribbon that has already been deformed, so the bending is mainly governed by elastic strain. The possible explanation of the elastic contribution may be presence of elastic twins, which were analyzed and discussed by Straka et al. [11]. Elastic strain may occur when partial dislocations are able to move freely back and forth as the applied load increases and decreases, respectively.
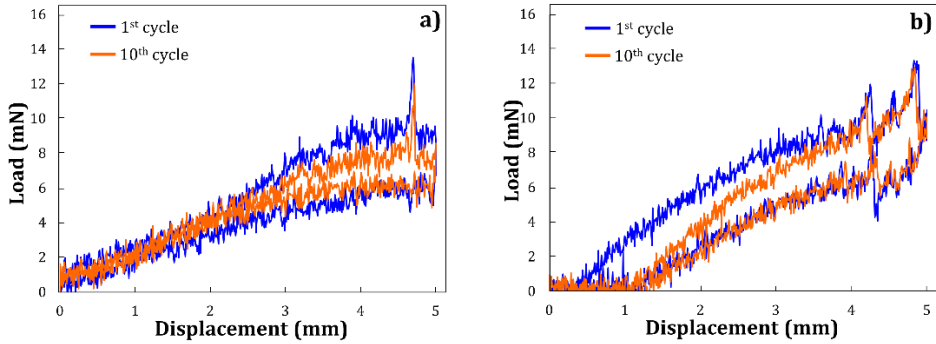
Fig.2. *Load vs. displacement curves recorded during mechanical bending experiments of Co_1Cu_1 (a) and Co_6Cu_6 (b) melt-spun ribbons produced at 20 m/s.*

It was noted that the load required to initiate deflection decreased with each subsequent cycle. The difference in bending load between the first and tenth cycles was around 1.5 mN for Co_1Cu_1 and approximately 1.9 mN for Co_6Cu_6 ribbons. Additionally, the hysteresis loop became progressively narrower as the number of cycles increased. Taking advantage of load-displacement curves, the changes in the plastic ($D_{plastic}$) and elastic ($D_{elastic}$) contributions to the total deflection (D_{total}) were calculated. Plastic strain for each cycle was determined by subtracting the $D_{plastic}$ of the previous cycle from that of the current cycle, while $D_{elastic}$ was obtained by subtracting $D_{plastic}$ from the total measured deflection.

Figure 3 illustrates the variations in the ratio of $D_{plastic}$ and $D_{elastic}$ strain to the total deformation (D_{total}) during cyclic bending, as a function of wheel velocity. It was found that the plastic contribution is inversely proportional to the linear velocity. The highest plastic strain occurred in the ribbons produced at 5 m/s, while the lowest was observed in the ribbons fabricated at 20 m/s. It was due to the fact, that microstructure of the ribbons produced at lower velocities exhibited larger grains and fewer grain boundaries, which act as obstacles during the reorientation of martensite variants under deformation.
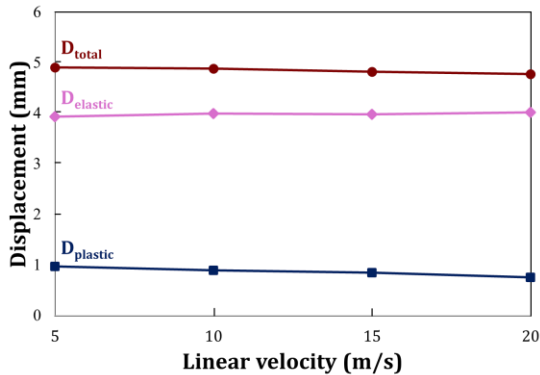
Fig.3. *Plastic ($D_{plastic}$) and elastic ($D_{elastic}$) contributions to the total value of deflection (D_{total}) as a function of linear velocity for the ribbons with 6 at. % of Co and Cu.*

Conclusions

Based on the research, the following conclusions can be drawn:

(i) Mechanical bending response of melt-spun ribbons with 1 at. % of Co and Cu exhibited pseudo-elastic character, due to the presence of solely $L2_1$ austenite parent phase;

(ii) Upon further alloying up to 6 at. % of Co and Cu, the changes in phase composition to NM martensite phase occurred and the overall deformation was composed of plastic and elastic contributions;

(iii) The plastic contribution was dominant during the initial bending cycle, but significantly decreased with continued cycles, where the bending was mainly governed by elastic strain;

(iv) The relationship between plastic contribution and linear velocity of the copper wheel was found to be inversely proportional.

References

[1] M. Acet, Ll. Manosa, A. Planes, Magnetic-field induced effects in martensitic Heusler-based magnetic shape memory alloys, Handbook of Magnetic Materials (2011), 19, 231-289.

[2] K. Ullakko, J.K Huang, C. Kantner, et al. Large magnetic-field-induced strains in Ni2MnGa single crystals, Appl Phys Lett, 69, 1966-1968, 1996.

[3] P. Müllner, A.H. King, Deformation of hierarchically twinned martensite, Acta Materialia 58 (2010) 5242 – 526.

[4] E. Pagounis, R. Chulist, M.J. Szczerba, M. Laufenberg, Over 7% magnetic field-induced strain in a Ni-Mn-Ga five-layered martensite, Applied Physics Letters 105 (2014) 052405.

[5] E. Pagounis, R. Chulist, M.J. Szczerba, M. Laufenberg, Large magnetic field-induced work output in a NiMnGa seven-layered modulated martensite, Applied Physics Letters 107 (2015) 152407.

[6] A. Sozinov, N. Lanska, A. Soroka, W. Zou, 12% magnetic field-induced strain in Ni-Mn-Ga-based non-modulated martensite, Applied Physics Letters 102, 0211902 (2013).

[7] A. Soroka, A. Sozinov, N. Lanska, M. Rameš, L. Straka, K. Ullakko, Composition and temperature dependence of twinning stress in non-modulated martensite of Ni-Mn-Ga-Co-Cu magnetic shape memory alloys, Scripta Materialia 144 (2018) 52-55.

[8] Y. Ma, S. Yang, W. Jin, X. Liu, $Ni_{56}Mn_{25-x}Cu_xGa19$ (x=0,1,2,4,8) high temperature shape memory alloys, Journal of Compounds and Alloys 471 (2009) 570-574.

[9] M.J. Szczerba, Giant magnetic-field-induced bending effect in Ni-Mn-Ga-Co-Cu melt-spun ribbons, Scripta Materialia 205 (2021) 114203.

[10] M. Kowalska, P. Czaja, Ł. Rogal, M.J. Szczerba, Effect of Linear Velocity on Magneto-mechanical Properties of Ni-Mn-Ga-Based Melt-Spun Ribbons, Metallurgical and Materials Transactions A (2024), 1-10.

[11] L. Straka, H. Hanninen, N. Lanska, A. Sozinov, Twin interaction and large magnetoelasticity in Ni-Mn-Ga single crystals, Journal of Applied Physics 109 (2011), 063504.

Effect of annealing Ni-Mn-Ga based ribbons obtained by rapid crystallization on martensitic transformation behavior and microstructure

M. Dudziński[1*], M. Kowalska[1], Ł. Rogal[1], P. Czaja[2], M.J. Szczerba[1]

[1]Institute of Metallurgy and Materials Science, Polish Academy of Sciences, 25 Reymonta Street, 30-059, Kraków, Poland,
[2]Department of Materials Science and Engineering, Stanford University, Stanford, CA 94305, USA

[*]m.dudzinski@imim.pl

Abstract

In recent years, Ni-Mn-Ga and Ni-Mn-Ga-based alloys have gained attention due to their exceptional combination of magnetic and mechanical properties. Particularly in their single-crystal form, these materials exhibit significant magnetic field-induced strain (MFIS), a phenomenon driven by the reorientation of martensitic variants through deformation twinning and detwinning mechanisms. However, challenges related to the scalability of single crystals have spurred the exploration of alternative material architectures such as ribbons, microwires, and porous foams. This study focuses on polycrystalline Ni-Mn-Ga ribbons synthesized through melt spinning and subjected to various annealing conditions (100°C to 900°C) to investigate their microstructure and phase transformation behavior. Detailed X-ray diffraction (XRD) and differential scanning calorimetry (DSC) analyses reveal that annealing up to 500°C does not significantly affect the phase composition or grain size, while higher annealing temperatures (700°C and 900°C) result in marked grain growth and changes in phase stability. Moreover, the martensitic transformation temperatures shift to higher values as grain size increases, influencing the material's transformation kinetics. These findings offer critical insights into the processing-structure-property relationships of Ni-Mn-Ga ribbons, paving the way for their application in magnetically activated devices such as actuators and sensors.

Keywords: ferromagnetic shape memory effect, magnetic properties, magnetic field induced bending, fatigue properties

Introduction

In recent years, Ni-Mn-Ga and Ni-Mn-Ga-based alloys have garnered significant attention due to their unique integration of magnetic and mechanical properties [1-4]. These materials, particularly in their single-crystal form, can undergo considerable macroscopic shape transformations when exposed to an external magnetic field of less than 1T [5, 6]. This phenomenon, termed magnetic field-induced strain (MFIS), operates on a microscopic level through the reorientation of martensitic variants via the deformation twinning/detwinning mechanism [7-11]. Substantial efforts have been invested in understanding the fundamental aspects of this effect, leading to targeted modifications in various material characteristics that directly impact and potentially optimize MFIS.

Single crystals, unencumbered by the limitations imposed by grain boundaries, represent the optimal alloy state for realizing substantial magnetically induced strain (MFIS) effects. However, the fabrication and scalability of single crystals remain

challenging. As a result, significant efforts have been directed toward exploring alternative synthesis methods and material architectures, including porous foams, 3D-printed alloys, polymer-powder composites, micropillars, microfibers, oligocrystalline microwires, and melt-spun ribbons [12-19]. Microwires and ribbons, or more generally geometries with a large length-to-width ratio, are becoming extremely interesting; such geometries, in addition to exhibiting MFIS, also show the phenomenon of the magnetic bending effect (MFIB). In general, MFIB resembles in behavior a ferromagnetic wire fixed on one side and placed in an external magnetic field. The ferromagnetic wire will experience a certain amount of bending depending on the value of the magnetic field, but this will only occur in the elastic range. Ni Mn Ga-based ribbons under the above conditions were shown to be able to accommodate a relevant fraction of the plastic deformation. A detailed experiment described by Kucza et al. conducted on monocrystalline Ni-Mn-Ga beams showed 2 components of plastic strain: axial and bending strain, which are attributed to MFIS and magnetic torque induced bending (MTIB) phenomena respectively [20].

Material and methods

Materials of high purity: Ni - 99.9%, Mn - 99.95% and Ga - 99.99% were used to prepare master ingots of nominal composition - $Ni_{50}Mn_{30}Ga_{20}$ for melt spinning process. The resulting ingots were homogenized at 1173K for 72 hours, in order to protect the material from oxidation during the annealing process, the material was embedded in a sealed quartz ampoule under vacuum conditions. Then, using a circular saw, the ingot was divided into equal parts with a volume of approximately 1.2 cm3, which were then used as input for melt spinning process.

The specified volume of the material was placed in a quartz crucible and melted using induction heating under a protective helium atmosphere. Subsequently, the molten alloy was injected onto a copper wheel, which was additionally cooled and rotating at a speed of 15 m/s.

The ribbons were annealed at temperatures of: 100°C, 300°C, 500°C, 700°C, 900°C to study the effect of phase composition on fatigue and mechanical properties. The choice of specific temperature values is motivated by a recent detailed study [21] on the effect of annealing on the microstructure of Ni-Mn-Ga - based ribbons, where two distinct temperature ranges were identified, each having significantly different effects on microstructure. The first range, from 0°C to 500°C, is where the recovery process takes place. The second range, from 500°C to 900°C, is where recrystallization occurs. The crystal structure and phase composition of the produced ribbons at various temperatures were analyzed using a Bruker D8 X-ray diffractometer (XRD) at room temperature.

Results and Discussion

Analysis of the diffractograms measured on the wheel side reveals that the phase composition remains stable up to and including 500°C (Fig. 2.). In contrast, the diffractogram of the sample annealed at 700°C shows a marked weakening of the signal from the parent phase (L_{21}) between 49° and 54° 2θ, accompanied by a slight enhancement of the 5M phase signal. Notably, reflections from these planes significantly weaken or nearly disappear in the sample annealed at 900°C, which may suggest a reorientation of the crystallographic texture or a sequential martensitic transformation. Annealing at 900°C results in a substantial reorganization of the material's phase composition.
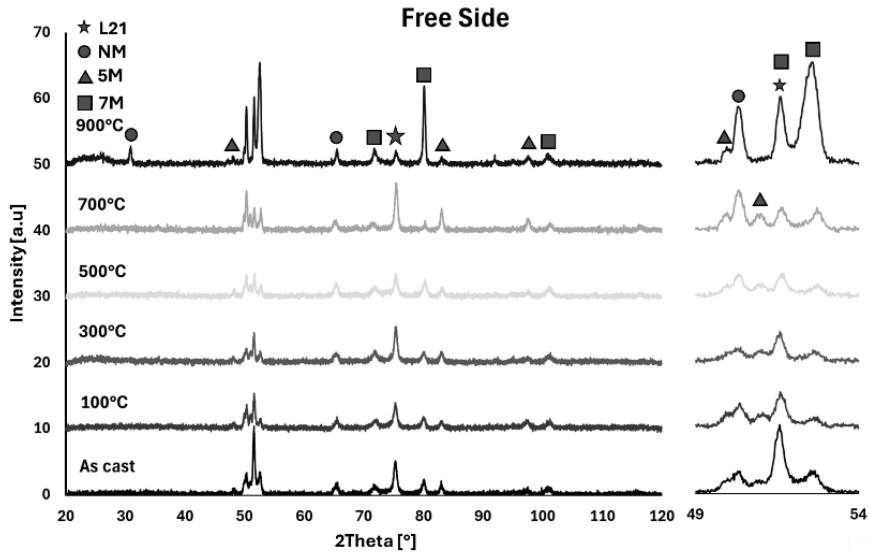
Fig. 1. *X-ray diffractogram of the ribbons obtained on free side.*

Detailed diffractograms of the ribbons, measured on the free side, are presented in Fig. 1. In the as-cast state, as well as after all heat treatment variants, multiple peaks corresponding to four distinct phases can be identified: the parent phase (L_{21}), non-modulated martensite (NM), and 5M and 7M modulated martensitic phases. A detailed analysis of the phase composition, depending on the annealing temperature, reveals that annealing up to 500°C does not induce significant changes in the phase structure. For samples annealed at 700°C, an increase in the intensity of peaks associated with the non-modulated and 5M martensitic phases is observed. Annealing at 900°C results in a sharp increase in the intensity of reflections corresponding to the non-modulated and modulated 7M phases. Figure 2. a) illustrates the martensitic transformation and reverse martensitic transformation for sample in AC state during the first and second heating and cooling cycles. It can be observed that, for all samples, the initial transformation and baseline exhibit an irregular behavior, differing slightly from the reverse transformation during the second cycle, following heating to 150°C and subsequent cooling to the martensitic phase.

Fig. 2. *Martensitic transformation (exothermic) and reverse transformation (endothermic) observed over two heating-cooling cycles for samples: (a) As-Cast (AC), (b) Annealed at 300°C, (c) Annealed at 500°C, and (d) Annealed at 900°C.*

The martensitic transformation is highly stable for each sample, as indicated by the overlapping curves in both cycles. Therefore, only cycle 2, representing the austenite → martensite → austenite transformation, provides a reliable characterization of the transformation behavior. The characteris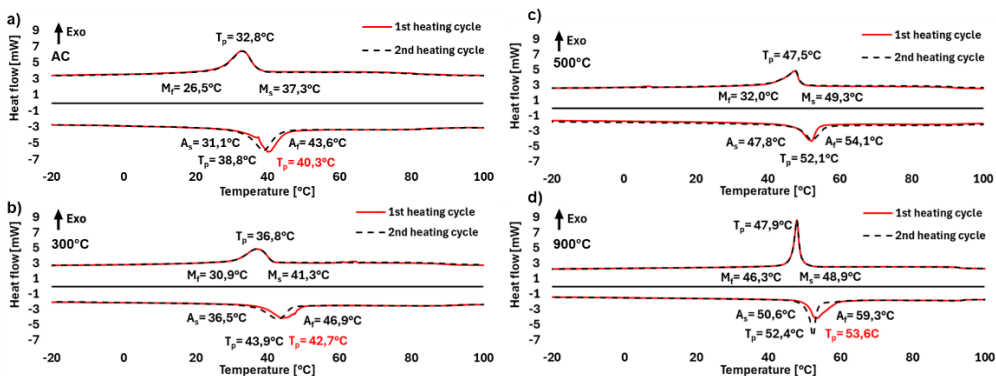tic temperatures for this cycle are listed in Table 1. As shown, the transformation temperatures are consistent for the martensitic phase transition, falling within a range of ±3°C. A similar trend was observed for the reverse transformation. Figure 2. b), c), d) summarizes the curves for two heating/cooling cycles of ribbons annealed at 300°C, 500°C, and 900°C. A noticeable shift in the temperatures of both martensitic and reverse transformations towards higher values is observed. To facilitate a detailed analysis of the transformation kinetics and hysteresis loops, the results are presented as dot plots in Figure 3. Samples annealed at 500°C and 900°C exhibit completely different transformation kinetics compared to the ribbons in the as-cast (AC) state. In contrast, annealing at 300°C, apart from a slight shift in the transformation temperature, does not significantly alter the transformation kinetics. An additional observation is that annealing at 300°C causes a slight increase in the transformation hysteresis loop, which then decreases significantly upon further annealing at 500°C and 900°C. The heat treatment significantly influences the martensitic transformation temperature (Fig. 2). It was observed that annealing shifts the characteristic temperatures of the martensitic transformation towards higher values. For sample AC, the presence of a "pinning effect" was detected, likely caused by stress fields generated by foreign atoms or excess vacancies. The method of ribbon production strongly suggests the presence of excess vacancies, which are retained in the structure due to rapid cooling from the liquid phase. By subjecting annealed samples to analysis (Fig 2. b), c), d), Fig. 3 a), b)), it is possible to observe a change in transformation kinetics depending on temperature. The martensitic transformation for these samples is stable, the reverse transformation to it shows temperature instability and a change in kinetics depending on the cycle.

Table 1. Summary of characteristic temperatures of transformations.

Sample	Martensitic transformation			Reverse transformation		
	M_s	T_p	M_f	A_s	T_p	A_f
AC	38,9	33,4	26,9	33,1	39,7	44,9
300°C	41,3	36,8	30,9	36,5	43,9	46,9
500°C	49,3	47,5	32,0	47,8	52,1	54,1
900°C	48,9	47,9	46,3	50,6	52,4	59,3
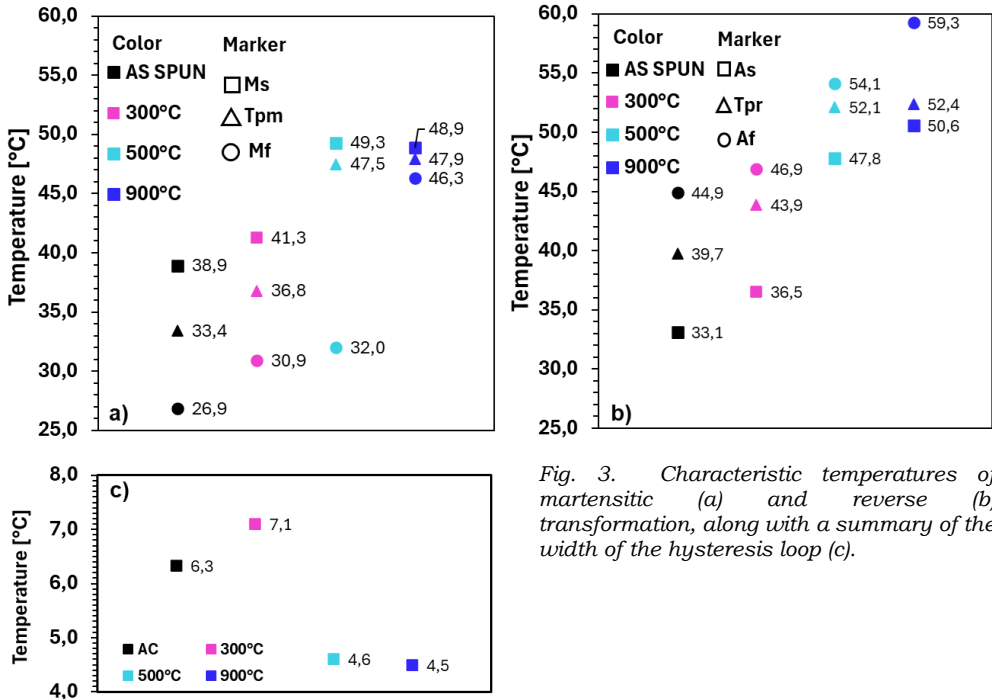
Fig. 3. Characteristic temperatures of martensitic (a) and reverse (b) transformation, along with a summary of the width of the hysteresis loop (c).

Figure 4. presents microstructure images of ribbons obtained via melt spinning for each heat treatment variant. In all cases, equiaxed grains with distinct boundaries are observed. The average grain size for the as-cast (AC) samples was approximately 6 µm. It was determined that annealing up to and including 500°C does not cause significant changes in grain size. However, heat treatment at 700°C and 900°C leads to considerable grain growth, with detailed values provided in Fig. 5.
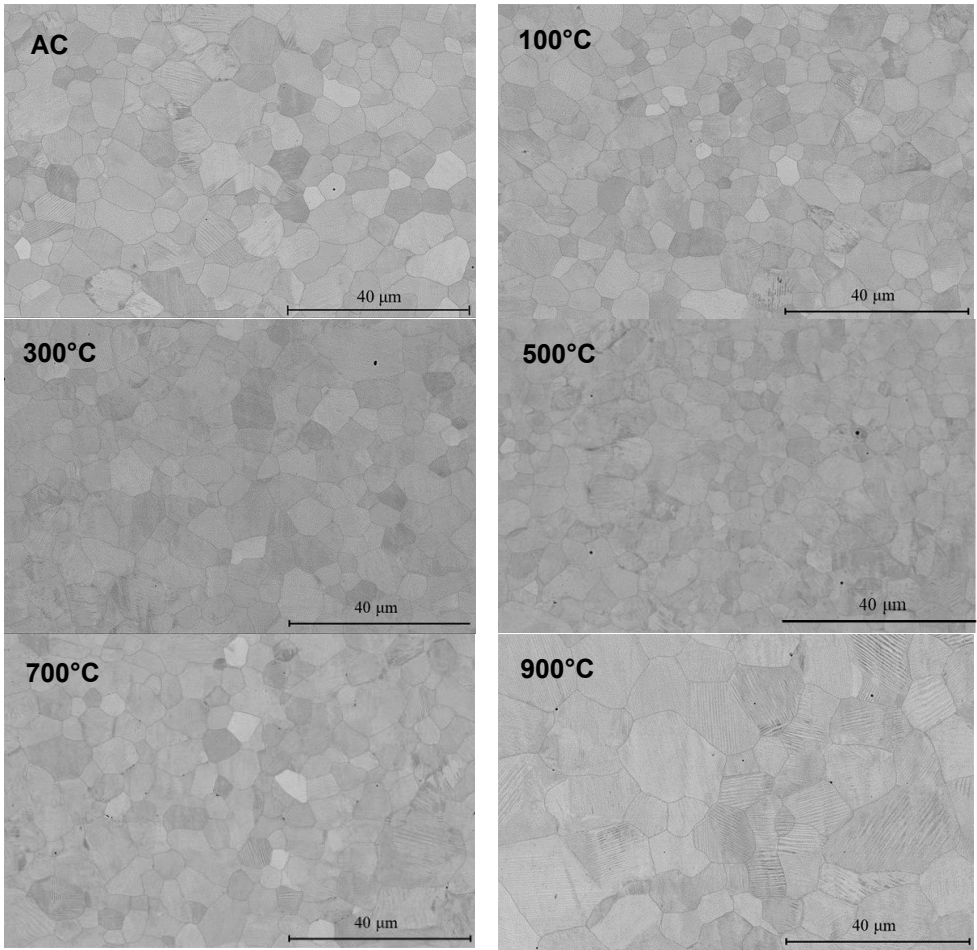
Fig.4. Microstructure of ribbon longitudinal section.
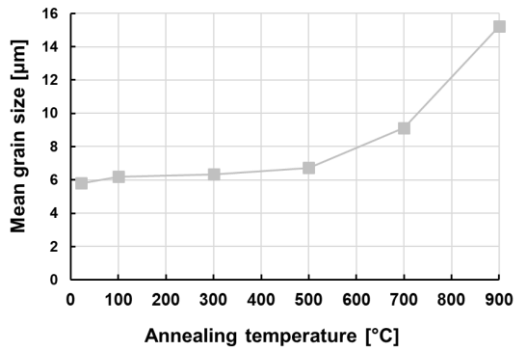
Fig. 5. Mean grain size as a function of annealing temperature

Conclusions

Ribbons cast and annealed in the temperature range of 100°C to 500°C were characterized by a small grain size (5.8 μm – 6.3 μm), with no observable grain growth. In contrast, annealing at 700°C and 900°C for 30 minutes resulted in a recrystallization process accompanied by abnormal grain growth. Therefore, it is reasonable to conclude that the martensitic start temperature (Ms) is influenced by grain size. DSC data further indicate that the temperature range of the martensitic transformation is broader for the as-cast ribbons compared to the ribbons annealed at 900°C The presence of larger grains in the microstructure significantly facilitates the martensitic transformation and shifts Ms to higher temperatures.

Acknowledgements

References

[1] K. Ullakko , J.K. Huang , C. Kantner , R.C. O'Handley , V.V. Kokorin , Appl. Phys. Lett. 69 (1996) 1966.

[2] F. Masdeu, J. Pons, J. Torrens-Serra, Y. Chumlyakov, and E. Cesari: Mater. Sci. Eng. A, (2022), vol. 833, 142362.

[3] J.F. Gomez-Cortes, P. Czaja, M.L. No´, M.J. Szczerba, and J.M. San Juan: Mater. Sci. Eng. A, 2023, vol. 881, p. 145339.

[4] P. Müllner , V.A. Chernenko , G. Kostorz , Scr. Mater. 49 (2003) 129.

[5] A .A . Likhachev , K. Ullakko , Phys. Lett. Sect. A Gen. At. Solid State Phys., 275 (2000) 142.

[6] M. J. Szczerba: Scr. Mater. Vol 205 (2011) 114203.

[7] L. Straka, O. Heczko, H. Seiner, N. Lanska, J. Drahokoupil, A. Soroka, S. Fa¨hler, H. Ha¨nninen, and A. Sozinov: Acta Mater., 2011, vol. 59, pp. 7450–63

[8] B. Karki, P. Mullner, and R. Pond: Acta Mater., 2020, vol. 201, pp. 604–16.

[9] L. Straka, N. Lanska, K. Ullakko, and A. Sozinov: Appl. Phys. Lett., 2010, vol. 96, 131903.

[10] S. Kustov, A. Saren, A. Sozinov, V. Kaminskii, and K. Ullakko: Scr. Mater., 2020, vol. 178, p. 483.

[11] M.J. Szczerba and M.S. Szczerba: Scr. Mater., 2012, vol. 66, p. 29.

[12] A. Mostafaei, K.A. Kimes, E.L. Stevens, J. Toman, Y.L. Krimer, K. Ullakko, M. Chmielus , Acta Mater. 131 (2017) 482.

[13] A. Mostafaei, P. Rodriguez De Vecchis, E.L. Stevens, M. Chmielus, Acta Mater. 154 (2018) 355.

[14] M. Chmielus, X.X. Zhang, C. Witherspoon, D.C. Dunand, P. Mullner, Nat. Mater. 8 (2009) 863.

[15] A.Saren, D.Musiienko, L. Straka, M. Vronka, J. Kopecek, O. Heczko, A. Sozinov, Kari Ullakko, Scr. Mater. 162 (2019) 482.

[16] T.-F.M. Chang, V. Chernenko, H.-C. Tang, C.-Y. Chen, A. Umise, M. Tahara, H. Hosoda, M. Sone, AIP Adv. 11 (2021) 025213.

[17] F. Lambrecht, N. Sagardiluz, M. Gueltig, I.R. Aseguinolaza, V.A. Chernenko, M. Kohl , Appl. Phys. Lett. 110 (2017) 213104.

[18] A. Mostafaei, K.A. Kimes, E.L. Stevens, J. Toman, Y.L. Krimer, K. Ullakko, and M. Chmielus: Acta Mater., 2017, vol. 131, pp. 482–90

[19] Y. Zhao, M. Kang, J. Xue, J. Ju, M. Wang, S. Wang, Y. Zhang, M. Vazquez, H. Gao, J. Wang, Scr. Mater. 162 (2019) 397.

[20] N.J. Kucza , C.L. Patrick , D.C. Dunand , P. Müllner , Acta Mater. 95 (2015) 284.

[21] M. Kowalska, M. J. Szczerba, T. Czeppe, P. Czaja, Conference paper of 11th European School for Young Materials Scientists.

Influence of Matrix Surroundings on ICP-RIE Mesa Etching Uniformity in 2-Inch Wafer Applications

M. Różycka[1,2,*], A. Jasik[1], K. Czuba[1], P. Kozłowski[1], A. Wierzbicka- Miernik[2]

[1] *Łukasiewicz Research Network - Institute of Microelectronics and Photonics, 32/46 Lotników avenue, 02-668, Warsaw, Poland*
[2] *Institute of Metallurgy and Materials Science, Polish Academy of Sciences, 25 Reymonta Street, 30-059, Kraków, Poland,*

[*] *marta.rozycka@imif.lukasiewicz.gov.pl*

Abstract

In the field of electronics, achieving uniformity in plasma etching processes on 2-inch wafers is of critical importance, both economically and in terms of process repeatability. Uniform etching ensures consistent device performance, particularly for complex semiconductor structures where precise control over layer thickness is required. This study investigates the influence of matrix surroundings on the uniformity of Inductively Coupled Plasma Reactive Ion Etching (ICP-RIE) of mesas on 2-inch wafers. The precise stopping of etching within specific layers of the superlattice, often referred to as the "sandwich" structure, is crucial for the optimal performance of the resulting electronic devices.

Two mask designs were employed in this study to assess the impact of matrix surroundings on etching uniformity. The first mask includes 32 matrices, 12 full matrices, each measuring 1 cm by 1.5 cm, uniformly distributed across the wafer, ensuring that each matrix is equidistant from its neighbors and 20 incomplete matrices that are just an add-on. This design promotes more homogeneous etching across the wafer. In contrast, the second mask features only 6 full matrices of the same size, with discrete detectors positioned along one edge of matrix. This asymmetric design leads to significant non-uniformities in etching, particularly at the four corners of each matrix, as well as across the entire 2-inch wafer.

The results highlight the importance of mask design and matrix arrangement in achieving uniform ICP-RIE mesa etching. The findings demonstrate that when matrices are uniformly surrounded, etching uniformity is significantly improved, whereas non-uniform surroundings lead to substantial variations in etching depth and quality. This study underscores the necessity of careful mask and layout design to enhance the reliability and performance of semiconductor devices produced on 2-inch wafers.

Keywords: ICP-RIE, dry etching, matrix, 2-Inch Wafer Uniformity,

Introduction

In the semiconductor industry, the uniformity of etching processes on 2-inch wafers is critical for the successful fabrication of electronic devices. Uniform etching ensures consistent parameters of devices, what is of particular importance for device performed on advanced semiconductor structures. The accuracy of this process has a direct impact on the economic efficiency and repeatability of device production, making it a vital aspect of modern electronics manufacturing. [1,2]

In the field of microelectronics technology, the uniformity of etching in lithographic processes, such as ICP-RIE (Inductively Coupled Plasma Reactive Ion Etching), plays a critical role in achieving high-quality semiconductor structures. In particular, mesa etching on 2-inch wafers requires precise control over process parameters, and one of the main challenges is the influence of matrix surroundings on etching uniformity. As highlighted in literature reviews, numerous studies focus on optimizing this process, with attention given to the impact of neighboring structures and plasma parameters on etching efficiency. Recent research emphasizes that non-uniformities in the surrounding areas can lead to varied results, directly affecting the final parameters of microelectronic devices. [2] Researchers are increasingly addressing this issue, seeking to understand and control this aspect of the process to achieve more consistent and repeatable outcomes. [3]

Experiment

Inductively Coupled Plasma Reactive Ion Etching (ICP-RIE) was utilized to etch mesas on 2-inch GaAs wafers. The etching process was carried out using a BCl_3 plasma, chosen for its effectiveness in etching III-V semiconductor materials. The ICP generator was set to a power of 300 W, while the RF power was maintained at 270 W. To enhance the etching precision and minimize thermal effects, the temperature of the chiller was lowered to -20°C. This low temperature was crucial in reducing potential etching non-uniformities caused by excessive heat, ensuring a more controlled and consistent process across the wafer [2,3].

The wafers were prepared using standard negative photolithography techniques, which allowed for the precise definition of patterns. Negative photolithography is a widely used method in semiconductor fabrication due to its ability to produce highly accurate and detailed patterns, which are essential for achieving the desired device characteristics [4].

At the start of the photolithography process, samples were heated at 120°C for a few minutes to eliminate residual water. Then, a hexamethyldisilazane (HMDS) primer was used to create a hydrophobic surface. A 1.5 μm thick AZ nLof 2070 photoresist film was applied via static spin-coating, followed by a 60-second soft bake at 110°C to remove remaining solvent. The vacuum contact method aligned the lithographic mask, and the sample was exposed to UV radiation (70 mJ/cm²) from a 500 W mercury vapor lamp. A post-exposure bake at 110°C for 60 seconds completed the photoreaction. Finally, unexposed photoresist was removed by immersing the sample in developer solution (Az 726 MIF) for 60 seconds.

After the etching process, the samples were measured using a 3D profilometer. This measurement technique provided detailed topographical data on the etched surfaces, allowing for an in-depth analysis of the etching uniformity across the entire wafer [5].

Results and discussion

The first photolithographic mask (Figure 1) analyzed in this article, designed for etching structures on 2-inch wafers, contains six full matrices with dimensions of 1 cm by 1.5 cm, a resolution of at least 320x240 pixels, and a pixel pitch of 30 μm. Each of these matrices has been precisely designed to achieve high-quality patterns during the etching process, which is crucial for ensuring the consistency of optical

and electrical parameters in the final structures. In addition to the photodetector matrices, the mask also includes a set of discrete detectors. These detectors enable rapid measurement of electrical parameters, such as current-voltage characteristics and sensitivity, allowing for quick feedback on the performance of the entire system.

Figure 3 Etched 6 full arrays and discrete detectors on an appropriately cut piece of 2-inch GaAs wafer, using a photolithographic mask prepared for etching 2-inch GaAs structures, where the surroundings of each array are not the same.

When analyzing the design of this mask, it is also important to note the specific arrangement of the matrices. Out of the six matrices, in four cases, one of their edges is not surrounded by other matrices, which may affect the uniformity of the etching. The difference between lowest and largest values of Δd_1 is ~ 0.39 μm (Table 1). The lack of adjacent structures on this edge may cause local differences in gas flow during the ICP-RIE etching process, leading to variations in etching depth on these matrices. This type of asymmetry in the mask layout presents a challenge in achieving perfect etching uniformity across the entire wafer, which is critical in the context of producing high-precision devices.

Table 2 Parameters describing the etch depths of a sample made with a photolithographic mask, where discrete detectors are additionally etched at each matrix, measured on a Filmetrics Profilm3D optical profilometer where a - left upper corner, b - right upper corner, c - left lower corner, d - right lower corner of each matrix, marked in Fig. 1.

Lp.	Etching depth, μm				The difference between max and min depths (Δd_1), μm
	a	b	c	d	
1	6.13	6.53	6.14	6.22	0.40
2	6.46	6.50	6.24	6.15	0.35
3	6.39	6.45	6.57	6.93	0.54
4	5.88	5.96	6.13	6.04	0.26
5	6.08	6.23	6.11	6.19	0.15
6	5.91	6.17	6.03	6.09	0.26

The difference in etching depth across the entire wafer was 1.05 μm, while the variations within one of the matrices ranged from 0.15 μm to 0.54 μm, that is, the average difference in mesa etch height on a 2-inch structure was 0.33 μm.

Another photolithographic mask (Figure 2) used in the project, also designed for etching structures on 2-inch wafers, contains 12 full matrices with the same dimensions as the first mask, i.e., 1 cm by 1.5 cm. A key feature of this mask is its specific layout, where each full matrix is surrounded by an incomplete matrix. This arrangement results in the placement of an additional 20 incomplete matrices across the entire wafer, which is a significant improvement over the previous design.
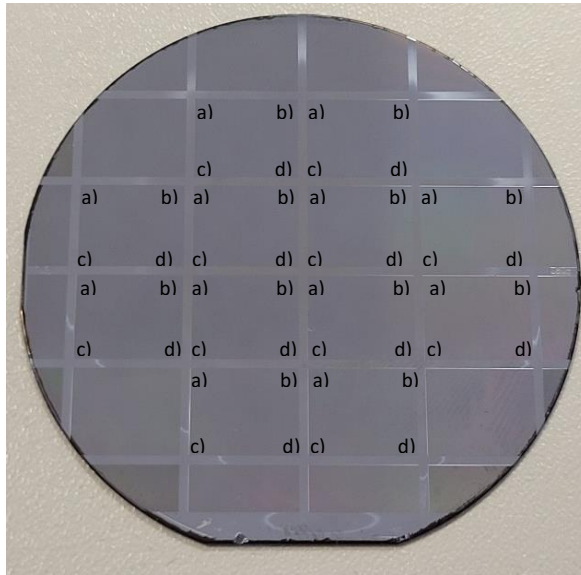
Figure 4 Etched 12 full and 20 incomplete dies on a 2 inch GaAs wafer, using a photolithographic mask, where the environment of each matrix is the same.

One of the greatest advantages of this configuration is that each edge of the full matrices is surrounded in the same way, eliminating issues related to the varying surroundings during the etching process. The homogeneous environment around each matrix ensures more stable etching conditions in the ICP-RIE technology, leading to a more uniform process across the entire wafer. As a result, differences in etching depth between individual matrices are minimized, which positively impacts the quality of the devices produced. The difference between lowest and largest values of Δd_2 is ~ 0.23 μm (Table 2). That's 50% less than in the case of the first mask. Moreover, the standardized surroundings of each matrix allow for more predictable and repeatable outcomes in the production process, which is crucial for precision structures such as photodetectors (Table 2).

Table 3 Parameters describing the depths of etching of a sample made with a photolithographic mask, where the environment of each die is the same, measured on a Filmetrics Profilm3D optical profilometer where a - left upper corner, b - right upper corner, c - left lower corner, d - right lower corner, marked in Fig. 2.

Lp.	Etching depth, µm				The difference between max and min depths (Δd_2), µm
	a	b	c	d	
1	5.07	5.11	4.97	5.01	0.14
2	5.10	5.28	5.01	5.21	0.27
3	4.95	4.94	4.97	5.04	0.1
4	4.93	4.97	5.05	5.09	0.16
5	5.01	5.21	5.08	5.07	0.2
6	5.23	5.38	5.11	5.17	0.27
7	4.92	5.06	4.96	4.97	0.14
8	5.06	5.06	4.98	5.02	0.08
9	5.04	5.04	5.03	5.06	0.03
10	5.06	5.16	5.04	5.15	0.12
11	4.97	5.01	5.18	5.24	0.27
12	5.02	5.06	5.24	5.34	0.32

The difference in etching depth across the entire wafer was 0.46 µm, indicating a more stable process. Within a single matrix, the etching depth was more stable, ranging from 0.08 µm to 0.32 µm, which positively impacts the quality of the final product, that is, the average difference in mesa etch height on a 2-inch structure was 0.175 µm.

Conclusions

The experiment analyzed the influence of two different masks on etching uniformity in the ICP-RIE process for 2-inch GaAs wafers. The first mask, enabling simultaneous etching of six dies and discrete detectors, exhibited twice the variation in etching depth, both across the entire wafer and within individual matrices. Despite the advantage of obtaining rapid electrical information, the significant non-uniformity in etching could negatively affect the quality of the matrices produced.

In contrast, the second mask, where the surroundings of each matrix were the same, provided significantly better etching uniformity. Additionally, the use of this mask allowed for a greater number of finished matrices, totaling 12, which is a crucial factor in improving production efficiency.

Comparing both approaches, the mask with uniform matrix surroundings ensures better etching uniformity at both the wafer and matrix levels, while also increasing production efficiency.

Acknowledgements

References

[1] E. Kwei-wei Huang, Multi-spectral Infrared Photodetectors and Focal Plane Arrays based on Band-engineered Type-II Indium-Arsenic / Gallium-Antimony Superlattices and its Variants, Northwestern University, (2013)

[2] M. Różycka, A. Jasik, P. Kozłowski, K. Bracha, J. Ratajczak, A. Wierzbicka-Miernik, The use of one-component plasma in the ICP-RIE etching process of periodic structures for applications in photodetector arrays. Metrol. Meas. Syst. 30; (2023). https://doi.org/10.24425/mms.2023.147955

[3] S. Li Tan, Y. L. Goh, S. Das, S. Zhang, C. H. Tan, J. P. R. David, N. Gautam, H. Kim, E. Plis, S. Krishna, "Dry etching and surface passivation techniques for type-II InAs/GaSb superlattice infrared detectors", Proc Volume 7838, Optics and Photonics for Counterterrorism and Crime Fighting VI and Optical Materials in Defence Systems Technology VII; 783814; (2010). https://doi.org/10.1117/12.864787

[4] H. Jung, K. Kang, S. Ryu, T. Lee, Jong Gi Kim, J. Eom, Young Chul Kim, A. Jang, Hyun Jin Lee, Young Ho Kim, Han Jung, S. H. Kim, J. Choi, Investigation of ICP dry etching of InAs/GaSb type-II superlattice LWIR photodetector, Proceedings Volume 11741, Infrared Technology and Applications XLVII; 117411V; (2021). https://doi.org/10.1117/12.2588043

[5] F. Rutz, R. Rehm, M. Walther, L. Kirste, M. Masur, A. Wörl, J. Schmitz, M. Wauro, J. Niemasz, R. Scheibner, J. Ziegler, Current developments for type-II superlattice imaging systems, Proc. SPIE 8012, Infrared Technology and Applications XXXVII, 80120U; (2011). https://doi.org/10.1117/12.883786

Micromechanical testing of on-chip interconnect stacks structures including FEM modelling

S. Weitz[1,2,*], A. Clausner[1], B. Jost[1], E. Zschech[2]

[1]*Fraunhofer Institute for Ceramic Technologies and Systems IKTS, Maria-Reiche-Str. 2, 01109 Dresden, Germany,*
[2]*Brandenburg University of Technology Cottbus-Senftenberg, Konrad-Zuse-Str. 1, 03044 Cottbus, Germany,*

[*]*stefan.weitz@ikts.fraunhofer.de*

Abstract

Semiconductor industry is continuing the downsizing of device dimensions and also of on-chip interconnect structures, both from performance motives but also from economic motives. This evolution has impacts for the design of guard ring structures, i.e. metallic non-functional systems in the back end of line (BEoL) stack at the periphery of these microchips. On the one hand, these protective elements have to be designed to be effective to stop microcrack propagation and, on the other hand, the footprint of these structures has to be as little as possible. To test the function of these protective structures, micromechanical experiments are required linked with appropriate characterization techniques to induce cracking and facilitate its visualization. Thus, a micromechanical in-situ test was integrated into an X-ray microscope (ZEISS Xradia 800 Ultra), ensuring high resolution imaging of the 3D-patterned sample structures and its flaws in 2D and 3D with a resolution of up to 50 nm during in-situ testing. Running tomographies allows non-destructive 3D visualization of the nanopatterned interior throughout the whole experiment and thus seamless 3D tracking of microcrack origination and propagation. A tailored sample design was developed which allows the application of tensile load to a BEoL sample by a lever mechanism. A microindenter is actuating the lever whose indentation load is quantified throughout the experiment. In this work, mechanical degradation and failure mechanisms in a BEoL stack due to fatigue loading are investigated, to foster understanding of the mechanical robustness and fatigue degradation of on-chip interconnect stack structures.

Palladium-based Membrane Reactors for Pure H_2 Generation

L. Alonso[a*], V. Suazo[a]

[a] *Hydrogen OnSite S.L (H2SITE), Gogorrenqa Bidea 2, 48180 Loiu, Spain.*

lydia.alonso@h2site.eu; vladimir.suazo@h2site.eu

Introduction

In recent years, the demand for pure hydrogen has increased owing to its important role as an energy source. The implementation of hydrogen economy could become the key to outbreaking the full potential of renewable energies to decarbonize the industrial sectors and meet the net zero emission target. Among the hydrogen separation processes, Pd-based membranes involve multiple advantages such as high hydrogen flux and exclusive hydrogen perm-selectivity. In the present work, a review on H2SITE's membrane reactor technology for the generation of pure hydrogen is presented.

Pd-based Membrane Reactors

H2SITE's membranes consist of thin-film composed of Pd-Ag, which are supported in a porous tubular support. Additionally, an external layer of a porous protecting ceramic is deposited on the membrane surface, filling in the defects of the Pd-Ag layer in order to maintain a high H_2 selectivity and reducing erosion produced by catalyst. Since the permeation is inversely proportional to the membrane thickness, thin Pd-Ag membranes give benefits of high hydrogen permeance while reducing the material cost.

These membranes are integrated in a reactor, which benefits from the capacity of high selectivity of Pd-Ag alloy membrane to be assembled within a catalyst to generate hydrogen from its precursor and separate hydrogen in a one-step process. Additionally, by employing membranes into the reactor, the hydrogen separation occurs in-situ as the hydrogen reaction takes place, shifting the equilibrium of the reaction, and consequently, due to Le Chatelier's principle, increasing the reaction rate [1].

Applications

Hydrogen Separation
In the new developing economy based on alternative fuels, hydrogen will be transported efficiently and cost-effectively. But the local production of hydrogen is not always possible as it highly depends on the local resources. However, transporting H_2 through the existing natural gas pipes for long distances is a potential solution. At the project H2SAREA is focused in developing a technological and economical method for hydrogen transport via natural gas pipelines. Furthermore, H2SITE's goal is to implement the separation of the blended hydrogen by using palladium-based membrane separators, obtaining high-purity hydrogen from any inlet stream, and unlocking the use of hydrogen in pipelines [2].

Hydrogen Generation

The ability to effectively store and transport large amounts of energy is a key element to enable reliable and flexible energy systems. Despite hydrogen potential, its low volumetric density prevents its use as an energy vector due to the cost of compression or liquefaction. In this context, ammonia outstands as a hydrogen carrier that benefits from a well-known supply chain and well-stablished standards for long distance transport. Being considered as a promising solution for the hydrogen economy and transport problem.

Currently the world's largest ammonia cracker based on the H2SITE's integrated membrane reactor concept is built within the AMMOGEN Project framework. This unit was commissioned at Tyseley Energy Park (Birmingham, UK) and is currently producing 200 kg/day of high purity hydrogen from green ammonia. Where hydrogen recovery factors over 97.5% have been demonstrated [3].

Conclusion

At H2SITE, the production of large scale Pd-based membranes has been industrialized, and membrane reactors are currently being fabricated, while efforts to continue improving the membrane reactors technology is a constant that is considered as a big step in the development and implementation of reliable renewable hydrogen technology.

References

[1] Melendez, J., Fernandez, E., Gallucci, F., van Sint Annaland, M., Arias, P. L., & Pacheco Tanaka, D. A. (2017). Preparation and characterization of ceramic supported ultra-thin (~1 µm) Pd-Ag membranes. Journal of Membrane Science, 528, 12–23. https://doi.org/10.1016/j.memsci.2017.01.011

[2] H2Sarea Project. July 28, 2023. https://www.h2sarea.com/difusion/

[3] A world-leading ammonia to hydrogen project at Tyseley Energy Park. Project Ammogen. https://ammogen.co.uk/

Nanoscale examination of degradation in copper metallization layers using lab-based nanoTXM and DFXM

L. Neumann[1,*], A. Clausner[1], M. Reisinger[2], C. Corley-Wiciak[3], Can Yildrim[3], Carsten Detlefs[3]

[1] *Microelectronic Materials and Nanoanalysis, Fraunhofer IKTS, Maria-Reiche-Str. 2, 01109 Dresden, Germany*
[2] *KAI Kompetenzzentrum für Automobil- und Industrieelektronik GmbH, Europastr. 8, 9524 Villach, Austria*
[3] *European Synchrotron Radiation Facility, Grenoble, France*

[*]*laura.neumann@ikts.fraunhofer.de*

Abstract

During application, high-power semiconductor devices undergo cyclic thermal loading caused by short circuit events. While the copper metallization provides rapid cooling to the underlying semiconductor material, it is prone to thermo-mechanical fatigue caused by high thermal stresses due to the different thermal expansion coefficients. Determining the conditions for the onset of copper metallization degradation, especially of void formation and crack growth, is therefore essential to further improve the reliability of high-power semiconductor devices.

Lab-based X-ray microscopy with a resolution of about 50nm is used to image the cracks and voids forming in the copper metallization during thermomechanical stress cycling. Synchrotron-based dark field X-ray microscopy (DFXM) is used to image single grains in the copper and determine their 3D shape and stress distribution.

The use of these complementary techniques achieves a comprehensive understanding of failure and deformation mechanism in the Cu metallization structures. Strain distributions in local grains can be correlated with small voids and cracks identified using nanoXCT, painting a comprehensive picture of intragranular microstructure refinement and condensation of structural defects near grain boundaries that perpetuate void formation and degradation in copper metallizations under fast-cycling thermal loads.

Keywords: microelectronics, X-ray, microscopy, dark-field, tomography

Introduction

Novel high power microelectronic devices are in high demand. Consisting of stacks of different materials like Si, Cu and Al, they undergo extreme cycles of thermal stress induced by high overload pulses during short circuit events, resulting in very high junction temperatures caused by extreme currents and power densities in the materials [1]. Copper used as metallization layer provides rapid cooling to the underlying semiconductor material, however due to the extreme difference in thermal expansion coefficient between silicon and copper, stress is introduced into the copper at the interface. Subsequently, voids and cracks are generated, causing degradation of the copper metallization [2]. Determining the conditions for the onset of this degradation is therefore essential to further improve the reliability of high-power semiconductor devices.

Lab-based TXM with spatial resolutions of 65 nm and a field of view of about 67µm by 67µm allows precise examinations of microelectronic or battery materials with significantly lower access barriers than synchrotron-based X-ray studies. The microscope can provide detailed nano X-ray tomographies (nanoXCT) and 2D radiographies of sufficiently thinned samples.

In DFXM, a coherent monochromatic X-ray beam is focused on a sample, projecting the shape of a single grain onto a distant diffraction detector, and magnifying the grain by placing an objective compound refractive lens in a proper position. It is used to reveal the shape and structure of single grains, enabling 3D mapping of the intragranular microstructure showing the lattice orientation and strain distribution.

Results and Discussion

To understand the fatigue behavior, polyheater test chips (Cu on Si) were thermo-mechanically pre-cycled by repetitive heating with a heating rate of 10^6 K/sec, each sample to a different amount of cycles. They were imaged with lab-based nanoXCT and reconstructed orthogonal slices of a copper metallization after 2500 heating cycles are shown in Fig. 1. The reconstruction shows, that after 2500 heating cycles cracks and voids have formed in the copper layer, visualized as white structures in the figure. Furthermore, on these samples the intragranular microstructure and strain evolution of singular Cu grains was observed, especially at high angle grain boundaries (HAGBs). To achieve this, dark field X-ray microscopy (DFXM) measurements performed at the ID03 beamline at ESRF are used to study the crystal orientation across grains and their evolution during degradation, providing experimental
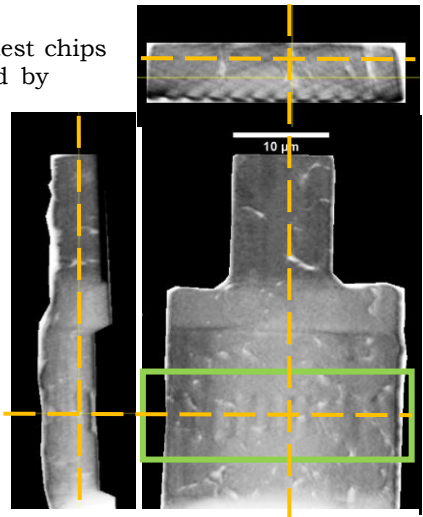

Fig.1. Reconstructed orthogonal views (orange axis) of Cu after 2500 cycles
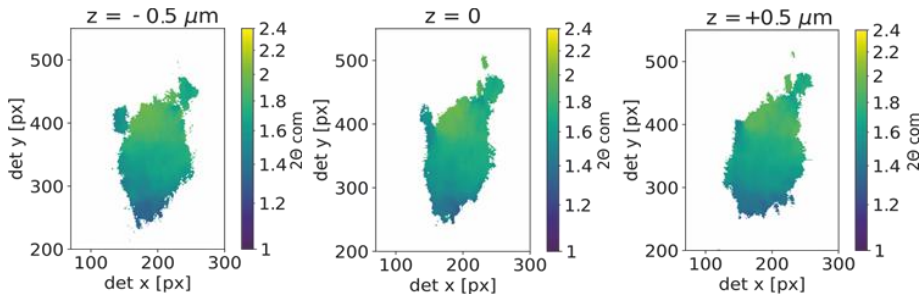

Fig.2. First order of moments (center of mass) of three middle slices of a grain after 2500 cycles, shape evolves in z over a distance of 1 µm. One pixel corresponds to approximately 40 nm.

evidence that mosaicity of Cu grains and residual elastic strain concentrations increase simultaneously in the vicinity of HAGBs [3].To determine the general shape of a single grain, far field intensity is summed up over a rocking curve, and different slices of the grain are examined by moving the beam (respectively the sample) in out of plane direction through the grain. The resulting data can then be processed using the ESRF darfix module. Several polyheater samples were cycled ex-situ and then examined with DFXM, the results of which are shown in figure 2, for the sample cycled 2500 times.

The general area, in which this respective grain can be found, is marked in green in figure 1.

The slices show inhomogeneous distribution of strain moments over the grain in multiple directions, indicating the presence of stress, for three different consecutive z-slices of the same grain. All DFXM slices are going to be stacked and stitched to cohesively provide the grains 3D shape, subsequently aligning the complete dataset with the 3D render of the reconstructed TXM tomography. The combination of both can then be adapted for comprehensive multi-dimensional damage modelling approaches.

Conclusions

While the DFXM technique provides great access to the crystallographic information of the Cu structure, it is limited to a few grains and grain boundaries, lacking the big-picture approach to correlate the onset of crack and void formation with stress-strain distributions. This is achieved by the lab-based nanoXCT, providing a 3D volume of the copper metallization and crack distribution throughout the sample. An exact association of 3D grain volume and 3D sample volume will give insight into the distribution of cracks and voids around grain boundaries after thermos-mechanical stress cycles.

Acknowledgements

References

[1] M. Nelhiebel, R. Illing, C. Schreiber et. al. A reliable technology concept for active power cycling to extreme temperatures, Microelectron. Reliab., 51, 1927-1932, 2011.

[2] T. Walter, G. Khatibi, M. Nelhiebel, W. Heinz, W. Robl, (2015). High-cycle fatigue properties of Cu films, Microelectron. Eng, 137, 64-69, 2015.

[3] K. Hlushko, T. Ziegelwanger, M. Reisinger et al. Intragranular thermal fatigue of Cu thin films: Near-grain boundary hardening, strain localization and voiding. Acta Materialia 253, 118961, 2023

1.0V FeRAM Operation Using Nanolaminate $Hf_{1-x}Zr_xO_2$ Film and Prospects for High-density Memory

A. Kashir[1], H. Jang[2], T. Schenk[1], M. Habibi[2], M. Schuster[1], S. Oh[2], X. Wang[1,*], H. Hwang[2], S. Müller[1,*]

[1] *Ferroelectric Memory GmbH, Charlotte-Bühler-Str. 12, 01099 Dresden, Germany,*
[2] *Center for Single Atom-based Semiconductor Device and the Department of Materials Science and Engineering, Pohang University of Science and Technology, Pohang 37673, Korea,*

[*] *xuetao.wang@ferroelectric-memory.com; stefan.mueller@ferroelectric-memory.com*

Abstract

Hafnia-based ferroelectric thin films demonstrate strong ferroelectricity, scalability, and compatibility with complementary metal-oxide semiconductor (CMOS) processes. However, their reliability remains a critical concern in ferroelectric random-access memory (FeRAM) devices, especially when operated at low voltages, typically below 2.0 V. This study first develops a $Hf_{1-x}Zr_xO_2$-based ferroelectric capacitor with a nanolaminate design of a precisely controlled HfO_2/ZrO_2 layering, Hf/Zr ratio and a proper annealing process, achieving low-voltage operation at ~ 1 V with excellent data retention (>10 years at 85 °C) and endurance (~10^{11} cycles at 10 MHz). The transmission electron microscope reveals that presence of thin tetragonal-like regions reduces the switching barrier in the optimized nanolaminate film. This is attributed to the stored strain inside the ferroelectric layer and the presence of tetragonal-like domain walls, making this a significant step toward the practical application of low-voltage FeRAMs. After addressing the reliability challenges for the planar device at low-operation voltages, the learning is transferred to the 3-dimensional devices. This work successfully develops a fabrication process for conformally coating the high aspect ratio trench with a HfO_2-based ferroelectric capacitor stack.

Keywords: $Hf_{1-x}Zr_xO_2$, nanolaminate, FeRAM, low-voltage operation, high aspect ratio

Introduction

Hafnia-based ferroelectric random-access memory (FeRAM) is gaining attention due to its non-volatility, high speed, scalability and compatibility with CMOS technology. However, the commercialization of HfO_2-based FeRAM faces reliability challenges during low-voltage operation.

Previous studies have primarily focused on enhancing switchable polarization and addressing reliability issues, such as the wake-up effect, imprint, and fatigue [1-3]. However, these efforts have largely concentrated on performance improvements without tackling the root cause of reliability challenges, which is the high coercive voltage (V_c) in $Hf_{1-x}Zr_xO_2$ (HZO) thin films. The persistently high V_c limits both endurance and retention, which are crucial for FeRAM applications. This study addresses these challenges directly by engineering a nanolaminate structure of HZO to reduce V_c, enabling reliable operation at 1 V while maintaining robust endurance and retention properties. Afterwards, this work further pushes the commercialization of HfO_2-based FeRAM by successfully fabricating a high aspect ratio trench device.

Results and Discussion

The large V_c of solid solution ferroelectric HZO stems from its intrinsic polar structure [4]. A fundamental solution to reduce the operation voltage is the V_c reduction. Recently, we showed that the design of an HZO-based nanolaminate structure consisting of orthorhombic/tetragonal (o/t) layers can facilitate the polarization switching [5]. **Fig. 1** illustrates how the thin t-phase layers reduce the switching barrier.
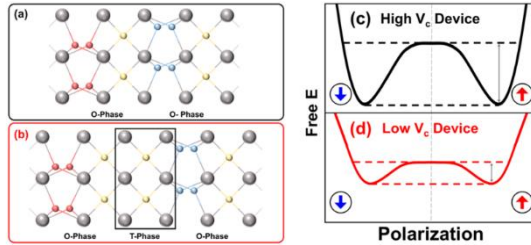

Fig. 1. Schematics of two HZO lattices with the (a) continuous o-phase and (b) o-phase with a thin t-phase. Gray spheres for Hf/Zr. Red, yellow, and blue for O. Schematic of the free energy for the polarization state of the (c) continuous o-phase and the (d) o-phase with a thin t-phase. [5]

The analysis of scanning transmission electron microscope (STEM) and high-resolution transmission electron microscope (HRTEM) images (cf. **Fig. 2**) confirmed the presence of t-phase interlayers, which can lower the switching barrier [6]. Additionally, a distorted crystal structure was observed in the inverse fast Fourier transformation (FFT) pattern, which can also facilitate polarization reversal [7].
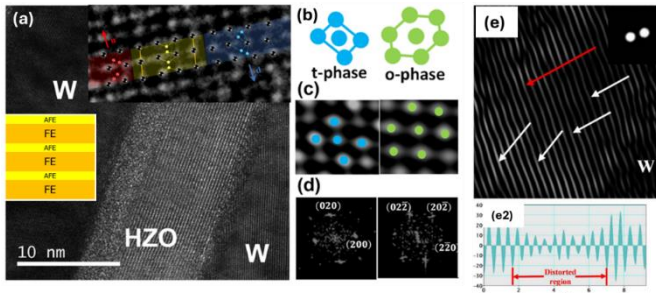

Fig. 2. (a) W/HZO/W cross sectional HRTEM image with a schematic image of HZO nanolaminate (middle left) and a STEM cross sectional image (top right). (b) atomic arrangements of t- and o-phase (c) STEM images that shows the t and o atomic arrangements (d) FFT pattern (e) inverse FFT pattern from HZO layer and (e2) the line profile [5, 7].

After further optimizing the fabrication process, thickness and chemical composition of the HZO layer, the performance of our nanolaminate HZO reached the target for FeRAM applications. The performance of planar devices from previous studies and this work is compared in **Fig. 3**.

Reference		Target	8	9	10	11	This work
RET	Q_{ss}	≥ 10 y / 85 °C	10 y / 105 °C	100 m / 85 °C	100 m / 85 °C	10 y / 85 °C	10 y / 85 °C
	Q_{os}	≥ 10 y / 85 °C	X	X	100 m / 85 °C	10 y / 85 °C	10 y / 85 °C
ENDU		≥ 1E12 / 85 °C	1E10 / 85 °C	1E18 / 85 °C	1E11 / RT	1E10 / RT	1E12 / 85 °C
Initial P_{sw}		≥ 40 μC/cm²	25 μC/cm²	19 μC/cm²	40 μC/cm²	25 μC/cm²	40 μC/cm²
V_{pp}		≤ 1 V	2.5 V	2.0 V	2.5 V	1.6 V	1.0 V
Thickness		≤ 6 nm	10.0 nm	8.0 nm	10.0 nm	4.0 nm	5.5 nm

Fig. 3. A performance comparison between this work and previous studies [5,8-11]. Retention (RET) includes the same state (Q_{ss}) and the opposite state (Q_{os}). Endurance (ENDU) is extrapolated at measuring frequency of 10 MHz. P_{sw} is the switchable polarization and V_{PP} stands for operation voltage.

Due to the constant growth of artificial intelligent, large storage capacity memory is desperately required to meet the demand of processing big data. The planar devices cannot satisfy the need when the technology node advances. Therefore, 3-dimensional (3D) FeRAM with a high aspect ratio trench is the solution to realize high-density memories. Since FeRAM was developed based on dynamic random-access memory (DRAM) technology, FeRAM could conveniently utilize the well-developed DRAM vehicle. However, the fabrication of 3D devices faces more challenges than planar devices, including conformality and harsh growth condition. After extensive iterations of process optimization, we successfully developed a conformal deposition of HfO_2-based ferroelectric capacitor stack. **Fig. 4** demonstrates the conformality of atomic layer deposition of electrodes and ferroelectric material in a 3D 30:1 aspect ratio trench studied via TEM and energy-dispersive X-ray spectroscopy (EDX).
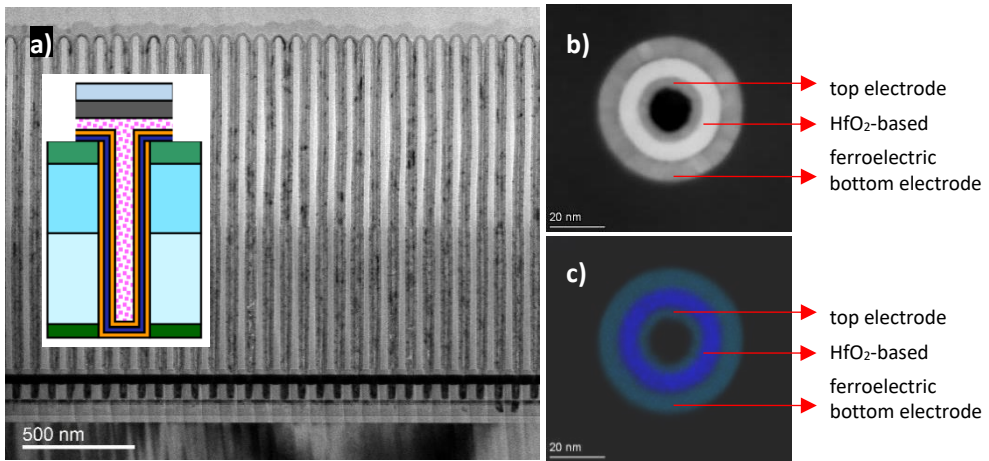
Fig. 4. a) cross-section TEM of a capacitor array with a schematic cross-section of a 3D capacitor trench. Plan-view cuts of individual capacitors via b) STEM as well as c) EDX.

Conclusions

This study introduced a newly designed nanolaminate structure of HZO films that significantly enhances the performance of FeRAM devices, enabling reliable operation at 1.0 V through reduced V_c. The incorporation of thin t-phase layers effectively lowers

the switching barrier, resulting in improved endurance (~ 10^{11} cycles) and retention (greater than 10 years at 85 °C). By precisely controlling the fabrication process, along with structural engineering, this study addressed the V_c-related reliability issues inherent in HZO-based ferroelectric devices. The results on planar devices pave a pathway to overcome challenges related to endurance, retention, and voltage scaling. Furthermore, a conformal deposition HfO_2-based ferroelectric capacitor was demonstrated on a 3D 30:1 aspect ratio trench. This work represents an important advancement toward the commercialization of low-voltage FeRAM technologies

Acknowledgements

References

[1] A. Kashir et al. ACS applied electronic materials, 3 (2), 629, 2021.
[2] P. Yuan et al. Nano Research, 15,3667, 2022.
[3] H A. Hsain et al. Nanotechnology,34,125703, 2023.
[4] H. J. Lee et al. Science, 369 (6509), 1343, 2021.
[5] H. Jang et al. ACS Applied Materials and Interfaces XX, 2024.
[6] D. H. Choe et al. Materials Today, 50, 8, 2021.
[7] A. Kashir and H. Hwang, Nanotechnology, 32, 445706, 2021.
[8] Y. Lin et al, Electron Devices Meeting, 15–23, 2021.
[9] J, Okuno et al, IEEE International Memory Workshop, 1–3, 2021.
[10] J. Okuno et al, IEEE J. Electron Devices Soc., 10, 29–34, 2022.
[11] K. Tahara et al, Symposium on VLSI Technology, 1–2, 2021.

Development of Super-Hard Ceramic Composites: Driving material innovation with Multiscale Material Characterization

L. Maier[1*], A.-K. Wolfrum[1], B. Matthey[1], M. Herrmann[1]

[1]*Fraunhofer IKTS, Fraunhofer Institute for Ceramic Technologies and Systems, 01277 Dresden, Germany*

louis.maier@ikts.fraunhofer.de

Keywords: Super-Hard Ceramic Composites, Spark Plasma Sintering (SPS), Multiscale Characterization, Interface Characterization

Cubic boron nitride (cBN), second only to diamond in hardness, is highly valued for industrial applications such as cutting tools and abrasives due to its low thermal expansion, chemical stability, high elastic modulus, thermal conductivity and hardness [1]. Aluminum oxide, widely known for its role f.e. as a wear resistant material and cutting tool in mechanical and plant engineering, can benefit from the incorporation of cBN. However, cBN undergos transformation into the stable hexagonal modification hexagonal boron nitride (hBN), respectively, at temperatures around 1300 - 1550 °C. Therefore, employing the Spark Plasma Sintering (SPS) technique for kinetic suppression of the thermally and/or chemically induced phase transformation in ceramic composites, weakening the interface between matrix material and cBN, is crucial for maintaining optimal mechanical and tribological properties. Although several studies have investigated aluminum oxide-based ceramics incorporating cBN, these investigations frequently reveal limited improvements in mechanical and tribological properties, alongside inaccuracies in determining the transformation of cBN [2,3,4]. These properties are significantly influenced by the formation of the particle interface during sintering, which is a key aspect that needs to be understood comprehensively. Another aspect that will be discussed is the crack formation that arises due to residual stresses [5]. In this context, advanced characterization techniques are essential for elucidating microstructural development. Investigations of Al_2O_3 composites with cBN are conducted at temperatures above 1300 °C, including the use of various coatings on the cBN. In order to analyze interface properties, sophisticated experimental characterization methods are employed. Phase transformations are examined using advanced techniques such as micro-Raman spectroscopy. This analysis will be accompanied by detailed and advanced experimental interface characterization. This includes high-resolution imaging techniques to precisely observe phase boundaries and grain structures of superhard ceramic composites, as well as spectroscopy methods to identify and quantify the chemical composition at interfaces, some of which are shown in figure 1.
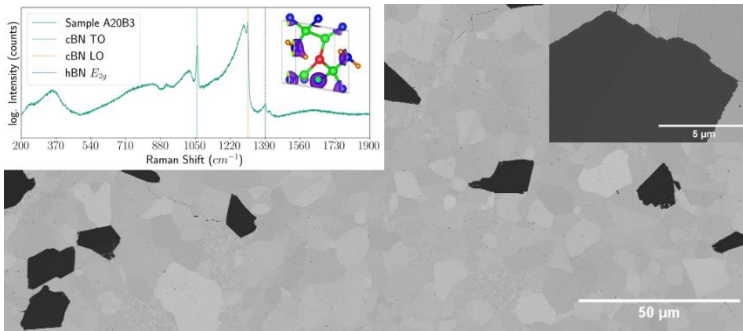
Fig. 1. *Representation of the microstructure of an aluminium oxide based ceramic composite with cBN and detailed characterization methods.*

References

[1] R. Riedel. Novel Ultrahard Materials. Advanced Materials 6,7-8, 549–560, 1994

[2] M. Hotta, T. Goto. Effects of cubic BN addition and phase transformation on hardness of Al2O3–cubic BN composites. Ceramics International, 37,5, 1453–1457, 2011

[3] P. Klimczyk et al. "Al2O3–cBN composites sintered by SPS and HPHT methods". Journal of the European Ceramic Society 36,7,1783–1789, 2016

[4] R. Sedlák et al. Micro/Nano Indentation Testing of Spark Plasma Sintered Al2O3 + ZrO2 + cBN Ceramics. Ceramics 4,1, 40–53, 2021

[5] F. C. Serbena, E. D. Zanotto. Internal residual stresses in glass-ceramics: A review. Journal of Non-Crystalline Solids 358, 6, 975–984, 2012

Phase evolution in Cr-Al-B system leading to MAB phase formation

J. Słomiński[*]

[1]*AGH University of Krakow, Faculty of Material Science and Ceramic, Department of Ceramics and Refractories, 30 Reymonta Street, 30-059, Kraków, Poland,*

[*]*slominsk@agh.edu.pl*

Abstract:

Cr_3AlB_4 is a promising candidate for high-temperature structural ceramics due to its unique combination of properties characteristic of both ceramics and metals. This study validates the formation mechanism of Cr_3AlB_4 as outlined in the literature through XRD, DSC, and SEM analyses. The results indicate that the synthesis of Cr_3AlB_4 is a multi-step process, initiating with the formation of CrB_2, followed by the generation of Cr_3B_4, which is subsequently intercalated with aluminum to yield Cr_3AlB_4. Notably, most existing scientific literature does not address the synthesis of MAB phases from powders that contain an amorphous component. The present work explores the feasibility of synthesizing Cr_3AlB_4 from such amorphous-containing powders and examines their impact on the synthesis process.

Keywords: MAB phases, borides, phase evolution, formation mechanism

Introduction:

The growing interest in high-temperature ceramics is driven by the need for high-performance materials in the aerospace sector. Key attributes such as elevated melting points, thermal stability, chemical resistance, and excellent mechanical properties are essential for addressing the challenges posed by such demanding engineering applications. While established ultra-high-temperature ceramics (UHTCs) like ZrB_2, HfB_2, and TiB_2 possess these advantageous properties, they also exhibit significant drawbacks, including extreme brittleness, high sintering temperatures, and low machinability, which complicate their processing.

MAB phases present a promising alternative to traditional ceramics, combining properties characteristic of both metals and boride ceramics. These phases are analogous to the well-known MAX phases and feature nanolaminate orthorhombic crystal structures composed of M-B layers (where M represents a transition metal and B represents boron) interspersed with aluminum or zinc layers, or double aluminum atom layers. The defined MAB phases include $MAlB$, M_2AlB_2, $M_3Al_2B_2$, M_3AlB_4, and M_4AlB_6. This paper specifically investigates the MAB phase within the Cr-Al-B system, focusing on Cr_3AlB_4 [9–12].
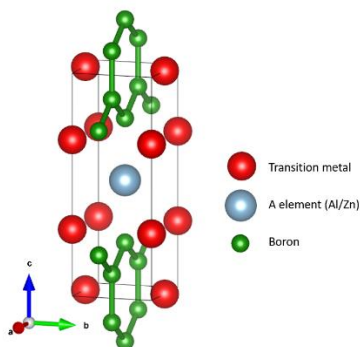
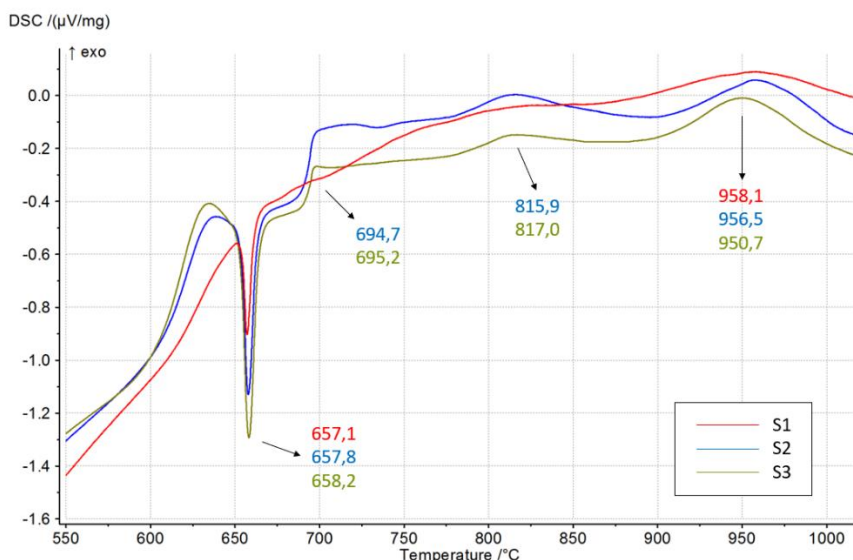**Fig 5**. *M₃AB₄ crystal structure*

Results and Discussion

Fig 2. *DSC curves for prepared mixtures*

All mixtures of powders containing CrB, Al, B were subjected to the thermal analysis by differential scanning calorimetry DSC. Figure 2 illustrates the obtained DSC curve. In the graph several thermal transitions within the system can be distinguished. Firstly, a high endothermic peak at about 658°C can be assigned to melting of aluminium. Slightly after that there is an exothermic peak at 695°C which indicate, the first transmission of a boride-synthesis of CrB_2. Other exothermic peaks can be seen at 816-817°C and 951-958°C. Both of them may be related to a further chemical reaction of CrB_2 in the system resulting in a formation of Cr_3B_4 and Cr_3AlB_4, respectively. Additionally according to XRD analysis (Fig. 3) a peak at 817°C can be assigned not only to the formation of Cr_3B_4 but also to the beginning of Cr_3AlB_4 synthesis. None of peaks during DSC measurement is assigned to any kind of

transition in the amorphous phase. For S1 sample with the lowest aluminium content, the effects on the DSC curve are the weakest and most blurred. In addition, for the first 3 peaks, it can be seen that a higher amount of aluminium affects the temperature of each transition making it slightly higher; on the contrary, for the last peak a higher amount of aluminium, the lower temperature of the transformation into Cr_3AlB_4.
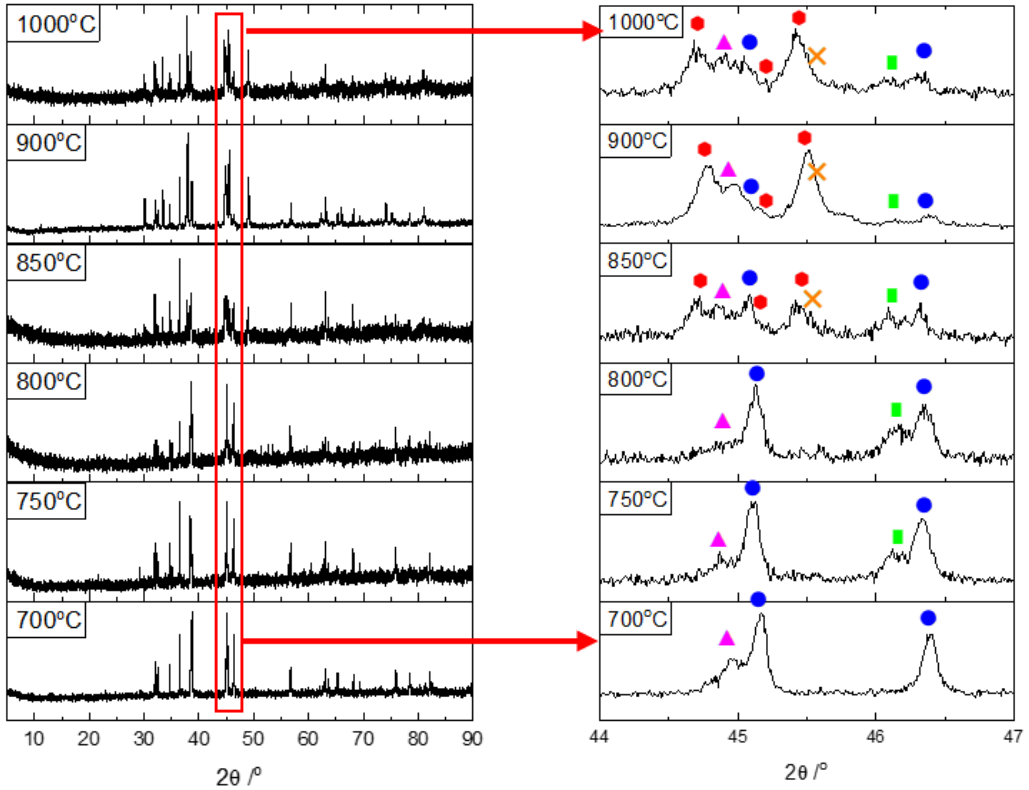
Fig 3. *XRD patterns and phase evolution in function of synthesis temperature*

Figure 4 illustrates the particle morphology of the powders, which varies with the phase composition of the synthesis products (Fig. 4). Samples with a significant MAB phase exhibit characteristic layered structures while those with less MAB show less defined morphologies, including visible slopes and terraces likely caused by elongated Cr_3AlB_4 grains in the residual amorphous phase. The S1 sample, annealed for 9 hours, displays numerous well-developed layered structures indicative of Cr_3AlB_4 (Fig. 4).

Fig. 4. *SEM images of morphology of synthesis product*

Conclusions:

With the reference to DSC thermal analysis all of the presented effects are consistent with the paper by Hanner et al. [1], but exact formation temperatures of each Cr-B phase (Eq.1-3), involved in the synthesis are slightly different. The difference may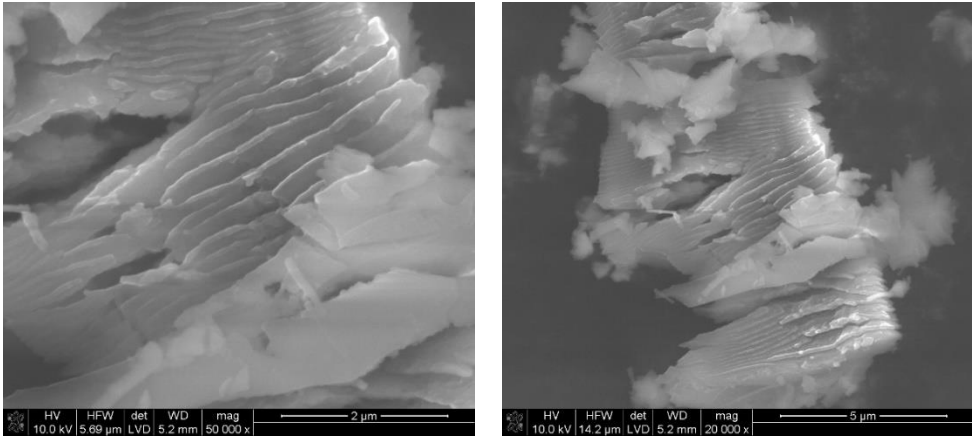 be related to the different amount of aluminium used in the present work and the one used in the Hanner's et al work [1] in the starting mixtures. Exothermic peaks at around 815-817°C may be related not only to the formation of Cr_3B_4 but also to the beginning of synthesis of Cr_3AlB_4 [2], despite the fact that the main peak related to the formation of Cr_3AlB_4 occurs close to 950°C. Initial forming of MAB phase at slightly lower temperature is caused by submicronic, freshly formed fine particles of metastable Cr_3B_4. These fine particles are in an aggressive, liquid aluminium environment that forces to react with aluminium, resulting in the formation of Cr_3AlB_4. Further rising of the temperature allows the system to produce larger grains and higher quantities of Cr_3B_4. At about 950°C aluminium intercalates large particles of Cr_3B_4 to form Cr_3AlB_4. The proposed mechanism is consistent with the literature data [1]. It has been shown to remain invariant even in the presence of an amorphous phase. Figure 8 is illustrates the crystal structure evolution during the synthesis process.
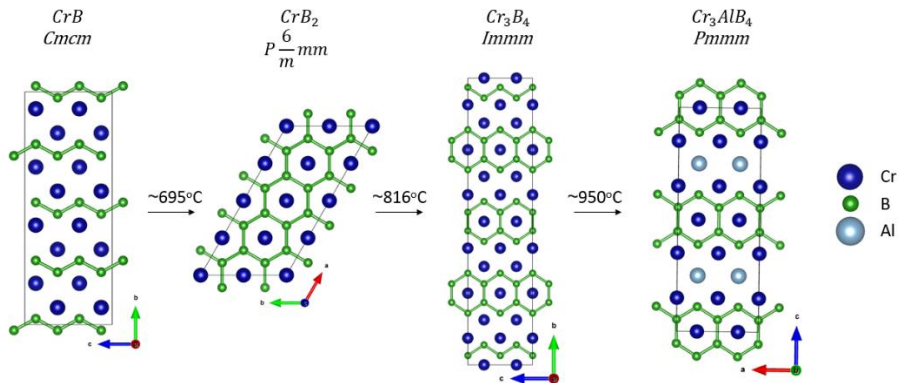
$$CrB + B \rightarrow CrB_2 \qquad\qquad \text{(Eq. 1)}$$

$$CrB_2 + 2CrB \rightarrow Cr_3B_4 \qquad\qquad \text{(Eq. 2)}$$

$$Cr_3B_4 + Al \rightarrow Cr_3AlB_4 \qquad\qquad \text{(Eq. 3)}$$

Fig. 5. *Evolution of crystal structure during Cr₃AlB₄ synthesis*

The formation mechanism of Cr_3AlB_4 is also confirmed by XRD analysis. Fig. 5 presents the evolution of the phase composition as a function of the starting composition of the samples and the synthesis temperature. The changes in phase composition and the number of identified phases coincide with the proposed mechanism for the synthesis of Cr_3AlB_4. The XRD data show that in the temperature range 750-850°C CrB_2 is formed, which transforms to Cr_3B_4 in the vicinity of 850°. This is also the temperature of the onset of Cr_3AlB_4 synthesis. XRD analyses also show that the amount of the amorphous phase decreases as the temperature increases (Fig. 5). It is mentioned in the literature that final product of synthesis in the CrB-Al-B system depends on the initial stoichiometry before heating [1]. This thesis is confirmed in this work; in XRD analysis there are no peaks assigned to Cr_2AlB_2. It worth mentioning that in the presented diffractograms there is no boron detected, due to the fact that it is amorphous. Additionally, Alamdari et al. [3] showed that boron can dissolve into liquid aluminium and form AlB_2. Although in this work that phase has not been detected. This might be explained by the fact that diffusion of boron within liquid aluminium and the further reaction with CrB prevents boron to cross the solvability limit, even locally, which results in the lack of conditions for AlB_2 to crystalize.

References:

[1] L.A. Hanner, S. Kota, M.W. Barsoum, Formation mechanisms of Cr_2AlB_2, Cr_3AlB_4, and Fe_2AlB_2 MAB phases, Mater Res Lett. 9 (2021) 323–328. https://doi.org/10.1080/21663831.2021.1912843.
[2] Y. Wang, L.X. Yang, R.J. Liu, H.P. Bu, Y.B. Mu, H.J. Liu, C.L. Zeng, S.L. Zhu, C. Fu, Molten salt synthesis of orthorhombic CrB and Cr_2AlB_2 ceramics, Ceram Int. 47 (2021) 31772–31779. https://doi.org/10.1016/j.ceramint.2021.08.059.
[3] H. Zhang, H. Xiang, F. zhi Dai, Z. Zhang, Y. Zhou, First demonstration of possible two-dimensional MBene CrB derived from MAB phase Cr_2AlB_2, J Mater Sci Technol. 34 (2018) 2022–2026. https://doi.org/10.1016/j.jmst.2018.02.024

Influence of wool fibre on polymer matrix characteristics in a controlled-release fertiliser

E. Szczepanik[1,*], E. Molik[2], K. Pielichowska[1]

[1]Department of Biomaterials and Composites, Faculty of Materials Science and Ceramics, AGH University of Krakow, Al. Mickiewicza 30, 30-059, Krakow, Poland
[2]Department of Animal Nutrition and Biotechnology, and Fisheries, Faculty of Animal Science, University of Agriculture in Krakow, Al. Mickiewicza 24/28, 30-059, Krakow, Poland

*eszczepanik@agh.edu.pl

Keywords: sheep wool; biopolymers; biocomposites; controlled-release fertilisers

Introduction

Sheep wool has been known for years as a fibre for textile applications. However, a significant amount of it (approximately 3 million tonnes per year), e.g., wool from dairy sheep, is not suitable for use in clothing. On the other hand, this fibre has many interesting properties that could prove useful in the design of innovative and environmentally friendly biocomposite materials. Wool has the ability to absorb large amounts of water, is resistant and can provide thermal and acoustic insulation [1]. The research presented here focused on the first property, as wool waste was used as the main ingredient in a biopolymer material for use as a CRF fertiliser. Controlled-release fertilisers (CRF) may be one solution to the growing effects of climate change (long droughts, overfertilisation of crops) [2]. Sheep wool added to the polymer accelerates its degradation in the soil and is also able to release gradually accumulated water and nitrogen and sulphur (from the proteins that make up the fibre) during decomposition, which are needed nutrients for plants [3].

In this study, polysaccharide compounds such as alginates were used as matrixes for CRF fertilisers, as they easily form a polymer network and are among the biodegradable compounds considered for agricultural applications. Their characteristics were compared with those of a polylactide (PLA)-based fibre polymer composite. Polysaccharide-based hydrogels were chosen because they can store large amounts of water and can further reduce the drying effect of the soil [4]. The aim of the study was to determine the properties of hydrogel-based composites, compare their characteristics with a PLA-based biodegradable composite, and to assess the effect of the wool fibre on the material composition. To do so, the absorption capacity of the materials and the study of soil water retention over time were conducted. In addition, characterisation of the composites was performed using thermal analysis (DSC) and SEM microscopy.

Results and Discussion

To create the hydrogel fertiliser, sodium alginate SA (4%, 6% and 8% concentration) was mixed with sheep wool fibres (2%) and cross-linked with calcium chloride solutions of two different concentrations (0.1M and 0.5M).

When testing the degree of swelling, samples cross-linked with 0.5M calcium chloride were observed to a significantly lower degree than those cross-linked with 0.1M. The addition of wool to the former improved the degree of swelling, while it reduced it in the case of hydrogels cross-linked with 0.1M. It can be inferred that the wool itself

absorbs large amounts of water but the addition of fibres blocks the structure of the hydrogel and that it is not able to swell on its own. The ability of wool to store water was confirmed by a soil water retention study, where both PLA-based and hydrogel samples with added wool retained moisture longer than soil alone. The hydrogel samples without the addition of wool did not show such properties. Hydrogels before and after the drying process were subjected to differential scanning calorimetry (DSC). In this way, differences that occur in the characteristics of the sample due to the presence of water. The samples were subjected to microscopic observation to analyse the influence of the wool fibre on the sample structure. It is a very high volume, low density fibre and its presence significantly affects the structure of the whole material.

Conclusions

The addition of wool has a very good ability to improve water retention in the soil. However, attention should be paid to the concentration and degree of cross-linking of the hydrogel matrix, as the introduction of fibre significantly disturbs the structure of the hydrogel network. The addition to thermoplastic polymers does not present such difficulties, but further research is needed to ensure complete polymer degradation and environmental protection.

Acknowledgements

References

[1] Szatkowski P., et al. Production of biodegradable packaging with sheep wool fibres for medical applications and assessment of the biodegradation process, Animal Sci Genet, 18/3, 57-57, 2022.
[2] Priya E., et al. A urea-loaded hydrogel comprising of cellulose nanofibers and carboxymethyl cellulose: An effective slow-release fertilizer, J Clean Prod, 434, 140215, 2024.
[3] Molik E., et al. Tradition and innovative in the protection of the natural environment of mountain regions, Acta Sci Pol Formatio Circumiectus, 22(3), 33, 2023.
[4] Lang Z., et al. Water retention and sustained release of magnesium-based biochar modified hydrogel composite materials, J Environ Chem Eng, 11, 111380, 2023.

Silicon Nanoparticle Sintering into a Porous Polycrystalline Material

J. A. Mendes[1,*], D. Gaspar[1], R. Martins[1], L. Pereira[1], H. Águas[1]

[1]*i3N/CENIMAT, Department of Materials Science, NOVA School of Science and Technology and CEMOP/UNINOVA, Campus de Caparica, 2829-516 Caparica, Portugal[2]*

[*]*jad.mendes@campus.fct.unl.pt*

Abstract

Silicon nanoparticles were synthesized through the gas-phase decomposition of silane and subjected to a sintering process to yield a porous polycrystalline material with 17× increase in grain size from the original nanoparticles. The morphologies of the initial and final material were assessed by employing several material characterization tools.

Introduction

Sintering and annealing of Si-based materials has been explored to change the structural, electronic, and mechanical properties of materials [1-5]. Sintered silicon nanoparticles (Si-NPs) present high surface area, tunable porosity, and good thermal, mechanical and electrical characteristics [1,6]. These can be applied in biomedical systems [7-8], electronics [9], and even lithium-ion batteries [10]. A number of bottom-up sintering processes for Si-NPs have been described in literature over the years [11-14]. In this work, we analyze Si-NPs before and after they undergo a sintering process.

Results and Discussion

As-synthesized Si-NPs were characterized using XRD, Raman spectroscopy and STEM. Si-NPs were found to be crystalline and spherical, with an average size of 3 nm, confirmed by XRD, Raman spectroscopy, and STEM. These were subjected to an undisclosed sintering process developed by our group, with the resulting sintered material characterized through XRD, Raman spectroscopy, STEM and SEM. The sintered material was found to have a porous network of interconnected crystalline grains with an average size of 53 nm, according to SEM (see Figure 1). XRD shows the minimum crystallite size to be 23.9 nm, suggesting the grains observed in SEM are polycrystalline in nature. This polycrystalline nature was confirmed by STEM imaging of the individual grains. Raman spectroscopy also indicates an increase in grain size and in crystallinity of the final material when compared with the original Si-NPs.

Conclusions

Sintering of 3 nm Si-NPs yielded a porous polycrystalline material, exhibiting a 17× increase in grain size from that of the initial Si-NPs according to SEM imaging (from 3 nm up to an average of 53 nm). The average crystallite size increased around 8×. The materials' crystallinity was also enhanced by sintering. The material appears to be promising for sensor and battery applications due to its porous polycrystalline nature.
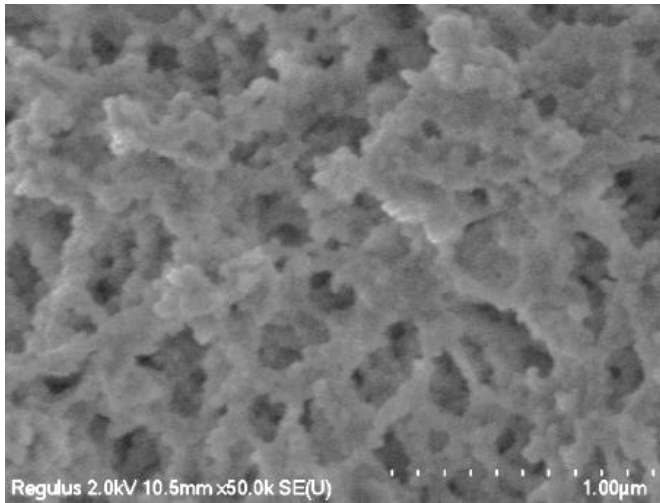
Fig.1. *SEM image of the sintered Si-NPs at a scale of 1 μm.*

References

[1] U. R. Kortshagen, R. M. Sankaran, R. N. Pereira, S. L. Girshick, J. J. Wu, and E. S. Aydil, "Nonthermal Plasma Synthesis of Nanocrystals: Fundamental Principles, Materials, and Applications," Chem Rev, vol. 116, no. 18, pp. 11061–11127, Sep. 2016, doi: 10.1021/acs.chemrev.6b00039.

[2] E. Gombia, R. Panizzieri, G. Salviati, and J. Vidal, "Growth and characterization of sintered polycrystalline silicon," J Cryst Growth, vol. 84, no. 4, pp. 621–628, Oct. 1987, doi: 10.1016/0022-0248(87)90053-4.

[3] R. Lechner et al., "Electronic properties of doped silicon nanocrystal films," J Appl Phys, vol. 104, no. 5, p. 053701, Sep. 2008, doi: 10.1063/1.2973399.

[4] G. Buscarino, V. Ardizzone, G. Vaccaro, and F. M. Gelardi, "Sintering process of amorphous SiO2 nanoparticles investigated by AFM, IR and Raman techniques," J Non Cryst Solids, vol. 357, no. 8–9, pp. 1866–1870, Apr. 2011, doi: 10.1016/j.jnoncrysol.2010.11.114.

[5] S. P. Bogdanov, A. P. Garshin, N. Yu. Korableva, and V. A. Ponomarenko, "Study of Sintering Polycrystalline and Composite Materials Based on Silicon Carbide in High-Pressure Equipment," Refractories and Industrial Ceramics, vol. 56, no. 1, pp. 66–71, May 2015, doi: 10.1007/s11148-015-9785-5.

[6] C. R. Kagan, "Flexible colloidal nanocrystal electronics," Chem Soc Rev, vol. 48, no. 6, pp. 1626–1641, 2019, doi: 10.1039/C8CS00629F.

[7] R. K. Kankala, Y. H. Han, H. Y. Xia, S. Bin Wang, and A. Z. Chen, "Nanoarchitectured prototypes of mesoporous silica nanoparticles for innovative biomedical applications," Dec. 01, 2022, BioMed Central Ltd. doi: 10.1186/s12951-022-01315-x.

[8] G. Maria Anna, "Biomedical Applications of Silica (SiO2) Nanoparticles," Biomed J Sci Tech Res, vol. 51, no. 1, Jun. 2023, doi: 10.26717/bjstr.2023.51.008057.

[9] E. Drahi, A. Gupta, S. Blayac, S. Saunier, and P. Benaben, "Characterization of sintered inkjet-printed silicon nanoparticle thin films for thermoelectric devices," in Physica Status Solidi (A) Applications and Materials Science, Wiley-VCH Verlag, 2014, pp. 1301–1307. doi: 10.1002/pssa.201300180.

[10] A. Fereydooni, C. Yue, and Y. Chao, "A Brief Overview of Silicon Nanoparticles as Anode Material: A Transition from Lithium-Ion to Sodium-Ion Batteries," 2023, John Wiley and Sons Inc. doi: 10.1002/smll.202307275.

[11] M. Biesuz and V. M. Sglavo, "Flash sintering of ceramics," Feb. 01, 2019, Elsevier Ltd. doi: 10.1016/j.jeurceramsoc.2018.08.048.

[12] B. J. Babalola, O. O. Ayodele, and P. A. Olubambi, "Sintering of nanocrystalline materials: Sintering parameters," Mar. 01, 2023, Elsevier Ltd. doi: 10.1016/j.heliyon.2023.e14070.

[13] D. Zymełka, S. Saunier, J. Molimard, and D. Goeuriot, "Contactless monitoring of shrinkage and temperature distribution during hybrid microwave sintering," Adv Eng Mater, vol. 13, no. 9, pp. 901–905, Sep. 2011, doi: 10.1002/adem.201000354.

[14] E. V. Astrova et al., "Formation of Porous Silicon by Nanopowder Sintering," Semiconductors, vol. 53, no. 4, pp. 530–539, Apr. 2019, doi: 10.1134/S1063782619040031.

Development of Computationally Efficient Numerical Models for Assessing the Reliability of Electronic Components under Vibration Loads

C. Lyu*, K. Meier, K. Bock

Institute of Electronic Packaging Technology, Technische Universität Dresden, Helmholtz Str. 10, Dresden, Germany

chengzhe.lyu@tu-dresden.de

Abstract

This work focuses on developing efficient models based on the Finite Element Method for data synthesis that is useful for solder joint reliability predictions under vibration tests. Starting from an existing detailed 3D Finite Element model of a vibration test vehicle assembled with Flip Chip components, efficiency optimized models were generated. Models were simplified to make use of periodically present structures. The equivalent inelastic strain occurring in the corner solder joints of the Flip Chip components was extracted from the simulation results and was further evaluated to assess the simulation accuracy. While cutting the calculation time down to 9 minutes, the modifications introduced strain result deviations that however did not exceed 15%. Replacing volume elements in thin structures with shell elements helped to significantly reduce the number of elements and nodes, thus shortening the calculation time. Additionally, implementing a submodeling approach did significantly reduce the calculation time, too.

Keywords: Finite Element Method (FEM); vibration test; inelastic behavior; computing time reduction; submodeling techniques.

Introduction

The reliability of electrical devices has always been the focus of attention. Common scenario for industrial and automotive device failures involves occurrence of cracks at solder joints due to mechanical vibration and temperature change. To address this issue, test specimens were developed to examine the fatigue behavior of lead-free solder joints [1], [2]. Furthermore, modifications were made to the specimen to enable analyses of Flip Chip (FC) package spherical solder joints, as shown in Fig. 1 [3]. Each specimen involves 1 FC at each narrow section of the cantilever, 8 FCs in total. These specimens are clamped onto a fixture on top of a shaker inside a temperature chamber, as shown in Fig. 2. Each of the FCs is mounted with 25 solder joints consisting of 96.5Sn-3.0Ag-0.5Cu (SAC305) alloys.

In addition to experimental testing, Finite Element Analysis (FEA) was used to obtain results regarding stress and strain. Corresponding Finite Element (FE) models were created and simulated in previous work, as illustrated in Fig. 3 [4]. Pin connections on the printed circuit board (PCB), accelerometer pads as well as circuit traces in PCB and FCs were omitted from the FE model because of requirements of simplification due to the focus on solder joint analyses. Furthermore, a quarter model was developed, which makes optimal use of the symmetry of the complete test vehicle and its model. The remaining boundary conditions include a 4 mm clamping region at

which a sinusoidal oscillation with a frequency of 125 Hz and a peak-to-peak amplitude of 250 µm is applied. Simulations are conducted considering room temperature (22 °C) condition. Additionally, finer mesh sizes of 0.1 mm were used in critical areas like solder joints and close-by copper pads and solder masks, while larger mesh sizes were applied to other regions. The quarter model represents the full and detailed model and serves as the starting point for this work.
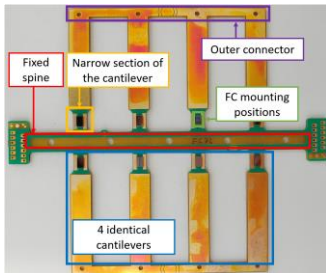

Fig.1. *Test vehicle for vibration tests: Printed Circuit Board assembled with 8 custom FC components.*
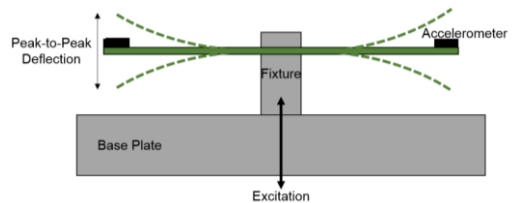

Fig.2. *Schematic setup of the experiment from* **Błąd! Nie można odnaleźć źródła odwołania.**.
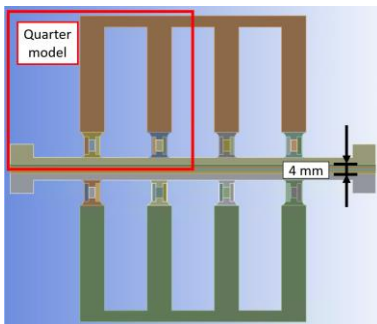

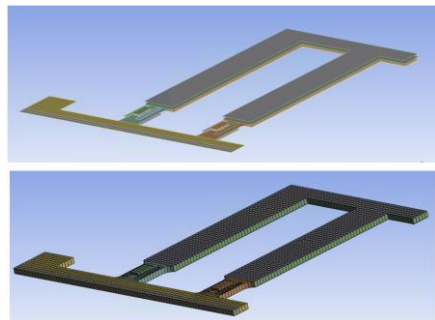**Fig.3**. *Complete and quarter FE model.*

Fig.4. *Model with shell elements. The tickness display in the vertical direction represents the thickness of the shell elements.*

Results and Discussion

The equivalent plastic strain (EPS) range of a corner solder joint's point in the last oscillation cycle was selected as the comparative data. Neglecting unused copper pads on the PCB has almost no impact on the results. Simplified models without solder masks have a significant reduction in element counts, resulting in a halving of computation time (from 77 min to 32 min) and a large deviation (38.8%). On this basis, a cantilever model and a half-cantilever model were devised taking advantage of the repeated topology. Their lower eigen frequencies lead to larger vibration amplitudes and EPS ranges. With a reduction of calculation time to 9 min, the half-cantilever model with a smaller relative deviation of 9% is considerable once the problem of unequal deflection is solved in the future, which further improves the accuracy. Based on the half-cantilever model, an examination about multicore computing was carried out subsequently, revealing that increasing the number of computational cores does

not necessarily result in a proportional decrease in calculation time, indicating the presence of computational constraints and communication costs.

A quarter model using shell and beam elements was used as global model with calculation time of 18 min, as shown in Fig.4. Implementing the submodeling technique, a series of submodels were generated and compared. With appropriate submodels, the calculation time can be reduced to 3 min, and the deviation is less than 8%. If it is determined that changes to the solder joint structures and material properties do not significantly impact the global model, this can lead to a substantial reduction in computing time by altering corresponding parameters only in the submodel. The neglected solder masks in those modifications should be reintroduced in the future to match the original model though longer calculation times have to be expected.

Conclusions

In this work, several modifications have been proposed to address the problem of insufficient data acquisition due to the extensive computing times of common full detail 3D solid FE models under isothermal vibration conditions. The evaluation of results took both calculation time and accuracy of the data into account. A dynamic element selection is to be considered in future work. Discarding irrelevant geometric details, such as unused copper pads, had almost no impact on the result. Neglecting solder masks in the model led to a significant reduction in the calculation time, but also resulted in larger result deviations. Rational use of repeating geometries and appropriate sub-modelling can also significantly reduce calculation time. Using more computing cores did not reduce computing time as the model size i.e., number of elements and nodes is yet rather small.

References

[1] K. Meier, R. Metasch, M. Röllig and K. Bock, "Fatigue measurement setup under combined thermal and vibration loading on electronic SMT assembly," Microelectronics Reliability, Dresden, 2018, doi: 10.1016/j.microrel.2018.06.003.

[2] K. Meier, M. Winkler, K. Bock, D. Lelsie and A. Dasgupta, "Fatigue Behaviour of Lead Free Solder Joints Under Combined Thermal and Vibration Loads," IEEE 69th Electronic Components and Technology Conference (ECTC), Las Vegas, May 2019, doi: 10.1109/ectc.2019.00082.

[3] K. Meier, D. Leslie, A. Dasgupta, M. Roellig and K. Bock, "Analysis of Flip-Chip Solder Joints under Isothermal Vibration Loading," 2019 IEEE 21st Electronics Packaging Technology Conference (EPTC), Singapore, pp. 138-142, December 2019, doi: 10.1109/EPTC47984.2019.9026642.

[4] M. Lehmann, "Entwicklung eines Finite-Element-Modells für die Analyse von FC-Lotkontakten unter isothermer Vibrationsbelastung," Studienarbeit, Technische Universität Dresden, Dresden, 2021.

[5] M. Ochmann, "Analysis of the Damage Behavior of Lead-Free Solder Joints at Low Temperature Vibration Conditions," Diplomarbeit, Technische Universität Dresden, Dresden, 2019.

A potential Fe^{3+} doped NIR phosphor under high-pressure

A. K. Somakumar[1,*], L.-I. Bulyk [1], V. Tsiumra[1], J. Barzowska[2], P. Xiong[3], A. Lysak[1], Y. Zhydacheyskyy[1], A. Suchocki [1]

[1] Institute of Physics, Polish Academy of Sciences, Al. Lotnikow 32/46, 02-668, Warsaw, Poland
[2] University of Gdańsk, Institute of Experimental Physics, Wita Stwosza 57, 80-308 Gdańsk, Poland
[3] The State Key Laboratory of Luminescent Materials and Devices, South China University of Technology, Wushan Road 381, Guangzhou 510641, China

[*] skumar@ifpan.edu.pl

Abstract

The present work investigates the NIR luminescence properties of iron (Fe^{3+})-doped lithium gallate ($LiGaO_2$) phosphor material under ambient, low-temperature and high-pressure conditions. The oxide phosphor is thoroughly characterised using techniques such as X-ray diffraction (XRD), luminescence, and decay measurements employing diamond anvil cells (DAC), and mechanoluminescence. etc

Keywords: Diamond Anvil Cell, Transition metals, Iron dopant, Near Infrared luminescence

Introduction

Iron (Fe^{3+}) doped β-LiGaO2 inorganic phosphor materials with near-infrared (NIR) luminescence hold significant promise for applications in the biological field due to their biocompatibility and less cytotoxicity. Besides, it is considered an auspicious phosphor material for NIR LED applications [1, 2]. In addition to its optical qualities, solid β-$LiGaO_2$ has interesting mechanical features like piezoelectricity and elasticity. β-$LiGaO_2$ has also been used as a ceramic tritium breeder material in experimental fusion reactors. It serves as a solid gallium precursor source material for bulk GaN crystal formation as well as a lattice-matched substrate material for the growth of GaN, InN and ZnO materials. The results of our study reveal the phase transition behaviour of β-$LiGaO_2$ material under very high hydrostatic pressures in the gigapascal (GPa) range. To understand further about these transitions, we examined the near-infrared luminous characteristics of the sample under various physical conditions like high pressure and low temperature.

Results and Discussion

The preliminary XRD analysis reveals that the phosphor exhibits an orthorhombic crystal structure with a space group of Pna21 at room temperature, indicating the presence of a stable β-LiGaO2 phase with a particle crystalline size of around 32 nm. Photoluminescence measurements conducted under ambient conditions demonstrate a broad and highly intense NIR luminescent band centred at 746 nm when excited from various peaks in the excitation spectra. The intensity of this primary band decreases with increasing temperature and exhibits a red shift towards longer wavelengths. Notably, at low temperatures below 100 K, a sharp phonon band emerges around 710 nm, suggesting a relatively weak interaction between the dopant Fe^{3+} ions and the host lattice. The sample also shows potential mechanoluminescence

in the NIR range under certain pressure. High-pressure luminescence and decay measurements are performed using a diamond anvil cell setup at helium temperature, with a 275 nm laser excitation source. The decay profiles of the main and phonon bands at high pressure and low temperature are characterized and fitted using a three-exponential equation.

Conclusions

During the high-pressure luminescence measurements (up to 14 GPa), a phase change is observed around 3 GPa, marked by the disappearance of the main phonon line at 710 nm. This phenomenon indicates a pressure-induced phase transition from the initial orthorhombic phase to a trigonal phase at 3 GPa [3]. Additionally, the luminescence is nearly quenched at approximately 14 GPa to the amorphization of the material with an irreversible phase transition. Moreover, we also observed a decrease in milliseconds decay time with an increase in pressure.

Acknowledgements

References

[1] Zhou, Z., Yi, X., Xiong, P., Xu, X., Ma, Z. and Peng, M. (2020). *Journal of Materials Chemistry C*, 14100-14108
[2] Chen, C., Li, C.A., Yu, S.H. and Chou, M.M. (2014) *Journal of crystal growth, 402, 325-329*
[3] Marezio, M. and Remeika, J.P. (1965) *Journal of Physics and Chemistry of Solids*, *26*, 1277-1280.

MXene-based aerogels for application in solar thermal energy conversion and storage materials

K. Suchorowiec[, *], K. Pielichowska

Department of Biomaterials and Composites, Faculty of Materials Science and Ceramics,

AGH University of Krakow, al. Adama Mickiewicza 30, 30-059 Kraków, Poland

[*]*suchorowiec@agh.edu.pl*

Abstract

Green energy conversion and storage materials have become a focal point of current research efforts. MXenes have emerged as a new two-dimensional transition-metal carbides/carbonitrides with a great potential in large variety of applications especially those related to energy conversion and storage. Combining MXenes with other materials could provide a solar energy conversion effect and enhance the overall thermal performance of this kind of composite. This study aims to provide evaluation of properties of two different types of ultralight MXene-based aerogels based on poly(ethylene glycol) (PEG) and potato starch, which shows enormous potential for applications as solar energy harvesting and storage materials.

Keywords: MXene, aerogel, solar-thermal energy conversion

Introduction

In recent decades, the energy demand has been continuously growing. Renewable energy sources like wind, water, and the sun have gained the researchers attention, but the key aspect nowadays is not only to present a new renewable energy source but also to improve the efficiency of the existing renewable energy harvesting systems. Therefore, there is still a need for designing a sustainable material that could significantly improve thermal energy storage (TES) technologies.

MXenes are a relatively new category of two-dimensional materials that are obtained from transition-metal carbides/carbonitrides. As they possess unique properties related to high electron conductivity, fast ion transport capability, and abundant active sites, they have become significant material in conductive fillers, electrochemical energy storage, electromagnetic interference shielding, and catalyst support research and applications. What is more MXene nanosheets, with their exceptional light absorption capabilities, can easily convert solar energy into thermal energy [1].

Aerogels (AGs) are a class of three-dimensional materials characterized by extremely high porosity and low density. Due to their unique structure, they have been effectively utilized in various applications, such as thermal insulation, space technology, energy storage, and sensors [2]. Combining MXene with water-soluble polymers is an effective

method to obtain ultralight MXene aerogels with high porosity that could act as a functional or multifunctional material [3].

This study aims to provide two different ways to obtain sustainable and environmentally friendly MXene-based aerogels. First, based on potato starch clay (ST) prepared while heating. The second way use PEG 10000 solution. All initial processes were followed by lyophilization. Properties of obtained MXene-based aerogels were evaluated in terms of their thermal stability and thermal performance using thermogravimetry (TG) and differential scanning calorimetry (DSC). The microstructure of obtained MXenes and MXene based aerogels were examined by light microscope and scanning electron microscope (SEM). The performance of aerogels was also examined under artificial sunlight source.

Results and Discussion

The MXene solution of 2.3 mg/ml determined the maximum MXene wt% in the prepared aerogels. Due to the potential heat related degradation of MXenes, the maximum of 0.5 wt.% was incorporated into the starch clay. On the other hand, preparation of PEG 10000 solution in room temperature enables direct mixing of PEG 10000 in MXene solution and leads to obtain 10 wt% MXene-PEG 10000 aerogel. The SEM images of dried MXene suspension indicates a good delamination of the MAX phase precursor.

The preparation method of the obtained aerogels played a crucial role in the maximum MXene concentration in the final aerogel and also to the material microstructure. Fig.1. presents the comparison of SEM micro images of obtained aerogels. The PEG based aerogel have more uniform microstructure with similar pore sizes while starch-based aerogel presents lees uniform microstructure with non-regular pore sizes.
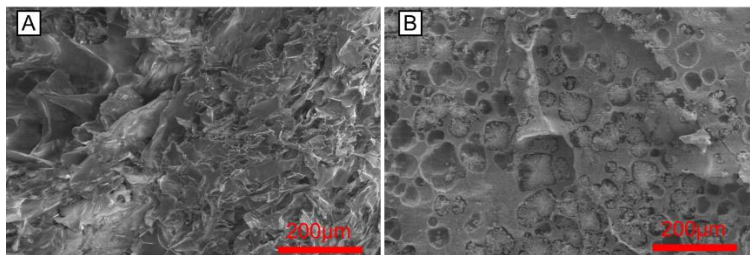

Fig.1. *SEM microimages of A-0.5%MXene-ST and B- 10%MXene-PEG10000 aerogels*

In the case of 10%MXene-PEG10000, a higher concentration of MXene nanosheets may also play a crucial role leading to radially speeded (treelike) PEG crystallites. In 0.5% MXene-ST aerogels, MXene concentration may be too low for making some impact on ST microstructure that have also probably established mostly in the heating process prior to MXene addition.

DSC curves of 10%MXene-PEG10000 (Fig.2. A) exhibited one endothermic peak that occurs in 63°C related to PEG 10000 melting process. The melting enthalpy of composite reached 115,7 J/g which is ~77% of theoretical enthalpy value for PEG 10 000 with 10 wt.% additive. The lower enthalpy value may be an indication of MXene-PEG crosslinking. The second exothermic peak may be related to the oxidation process that may be caused by the presence of MXene nanosheets that are rich in functional groups. In the cooling process the oxidation process may continue till 100°C and then an exothermic PEG crystallization peak occurs in 23°C. The enthalpy of crystallization reached 65,5 J/g which is ~45% of theoretical crystallization enthalpy value. This indicates that some interactions of PEG and MXene occurred leading to partial decomposition.
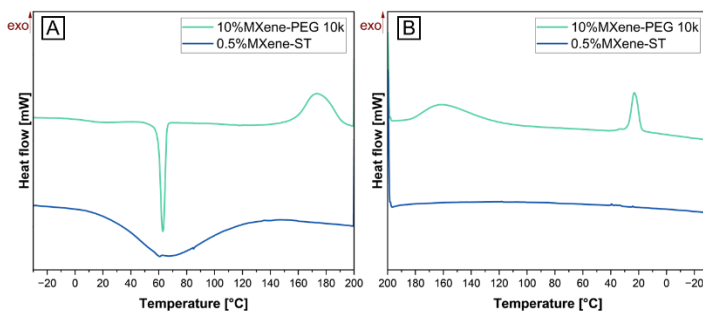

Fig.2. *Heating (A) and cooling (B) DSC curves of MXene-based aerogels.*

DSC curves of 0.5%MXene-ST (Fig.2. B) indicates a wide endothermic peak in the range form 7-150°C related probably to the following water loss or moisture desorption together with gelatinization of starch. Both samples do not exhibit any kind of radical decomposition up to 200°C in the DSC measurements. According to the TGA 10%MXene-PEG10000 main thermal degradation occurs in 388°C while 0.5%MXene-ST main thermal degradation occurs 307°C. This may be caused by the significant difference in the MXene concentration in the material, which has an impact on the thermal properties and decomposition.

Conclusions

The study highlights the importance of the preparation method and main component, as well as MXene concentration, on the structural and thermal properties of the resulting aerogels, with implications for their potential applications. The MXene-PEG combination leads to lover phase change related properties. All samples exhibited good thermal stability and highly porous microstructure that could be a promising sign for further material usage and examination in terms of shape stabilizers for low temperature phase change materials infiltration and thermal energy storage technologies.

Acknowledgements

References

[1]   P. Lin *et al.*, 'MXene aerogel-based phase change materials toward solar energy conversion', *Sol. Energy Mater. Sol. Cells*, vol. 206, p. 110229, Mar. 2020, doi: 10.1016/j.solmat.2019.110229.

[2]   K. Suchorowiec, N. Paprota, and K. Pielichowska, 'Aerogels for Phase-Change Materials in Functional and Multifunctional Composites: A Review', *Materials*, vol. 17, no. 17, Art. no. 17, Jan. 2024, doi: 10.3390/ma17174405.

[3]   C. Cai, Z. Wei, Y. Huang, and Y. Fu, 'Wood-inspired superelastic MXene aerogels with superior photothermal conversion and durable superhydrophobicity for clean-up of super-viscous crude oil', *Chem. Eng. J.*, vol. 421, p. 127772, Oct. 2021, doi: 10.1016/j.cej.2020.127772.